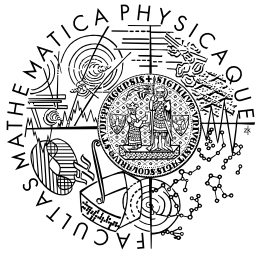

FACULTY
OF MATHEMATICS
AND PHYSICS
Charles University

MASTER THESIS

Matěj Konvalinka

Multichannel models of Siegert states in electron collisions with molecules

Institute of Theoretical Physics

Supervisor of the master thesis: Mgr. Zdeněk Mašín, PhD.
Study programme: Theoretical Physics
Study branch: FTFP

Prague 2024

I declare that I carried out this master thesis independently, and only with the cited sources, literature and other professional sources. It has not been used to obtain another or the same degree.

I understand that my work relates to the rights and obligations under the Act No. 121/2000 Sb., the Copyright Act, as amended, in particular the fact that the Charles University has the right to conclude a license agreement on the use of this work as a school work pursuant to Section 60 subsection 1 of the Copyright Act.

In ..... date ....

Author's signature

First of all, I would like to thank my supervisor Dr. Z. Mašín for all the time and support. I could not wish a better guidance and I have learnt so much about quantum physics from him.

The people from the Institute of Theoretical Physics have always been very helpful in any problem I have had. I would like to thank all of them and all of my teachers from the Faculty of Mathematics and Physics who showed me the beauty of physics.

I want to thank my parents who have always supported me in my education and have always been here for me.

Title: Multichannel models of Siegert states in electron collisions with molecules

Author: Matěj Konvalinka

Institute: Institute of Theoretical Physics

Supervisor: Mgr. Zdeněk Mašín, PhD., Institute of Theoretical Physics

Abstract: This thesis uses the phenomenon of the Siegert states and the R-matrix approach to analyze quantum scattering. The main task of the work is to implement the multichannel R-matrix method and test it on model potentials before applying it to ab initio scattering calculations. I follow up on my bachelor thesis where we described the Siegert states and their influence on the cross section and did the analysis for a short-range potential in one channel. In this work, we implement the multichannel approach within the one-particle R-matrix method. The method is tested for multichannel potentials and the long-range dipole and Coulombic potentials. Then we implement our approach into the multi-electron R-matrix UKRmol+ codes and apply our method to real molecular systems. We analyze the results of electronically elastic and inelastic calculations.

Keywords: scattering theory, S-matrix, Riemann surface, R-matrix theory, resonance

Contents

List of presented conference contributions

- **Analysis of collision processes in quantum mechanics**
  Matěj Konvalinka, Zdeněk Mašín
  Poster: AttoChem Prague, 2022

- **Analysis of collision processes in quantum mechanics**:
  Matěj Konvalinka, Zdeněk Mašín
  Poster: ATOM 23 Dresden, 2023

Units and conventions

Unless specified otherwise, we use the atomic units in all calculations, tables and diagrams; i.e. the following constants have a unit magnitude in the calculations:

- Planck constant: $\hbar$,
- Electron mass: m_e,
- Bohr radius: a_0,
- Atomic unit of energy: E_h.

In all the calculations, we denote matrices by letters in bold font $\mathbf{A}$ and vectors by letters with an arrow $\vec{a}$. The unit matrix is denoted by $\mathbb{I}$.

Introduction

This thesis follows up the bachelor thesis Konvalinka [2021] where we studied the one-channel scattering problem using the phenomenon of the Siegert states. The main task of the present thesis is to study the Siegert states in a multichannel quantum scattering problem and extend our study to real quantum systems.

We solve the non-relativistic Schrödinger equation in a non-spherical potential and search for the scattering solution. Such solutions are completely described by the energy and asymptotic conditions and can be expressed in terms of the S-matrix. The poles of the S-matrix, called Siegert states, are of a great importance for the analysis of the scattering problem. We divide them into the bound, virtual, and resonant states. The latter are characterized by the energy E_R and width Γ that define the location of the resonant states in the complex plane

$$E = E_R - \mathrm{i}\frac{\Gamma}{2}. \tag{1}$$

The resonant states are interpreted as temporary bound states of the system with the lifetime inversely proportional to the width of the resonance. For a small Γ, the resonant states strongly influence the cross section and other observable quantities which manifests itself by the resonant peaks.

For the physical interpretation of the structures in the cross section, it is important to know the locations of Siegert states and be able to separate the resonant contributions from the so-called background. We implement a mathematical approach similar to the one used in Rakityansky and Elander [2005] to remove the poles using the Mittag-Leffler expansion of the S-matrix.

The Siegert states were introduced by Siegert [1939] and the original application was for nuclear physics, similarly as for the R-matrix in Wigner and Eisenbud [1947]. In the original form, the Siegert states are defined by the outgoing wave boundary condition

$$\left(\frac{\mathrm{d}}{\mathrm{d}r} - \mathrm{i}k\right) u(r)\bigg|_{r\to\infty} = 0. \tag{2}$$

Early applications of the method were to model systems that can be solved analytically. The movement of the poles of the S-matrix in the rectangular potential well was studied in Nussenzveig [1959]. I reproduced his results in my bachelor thesis. The problem of one-channel long-range dipole potential and movement of poles is analytically solved in Estrada and Domcke [1984]. The articles Herzenberg and Saha [1983] and Herzenberg [1984] follow up the article by searching for the poles on various sheets of the complex plane. In this thesis, we reproduce their results to test our numerical approach and extend the model to more channels.

Later, in the 80s and early 90s, the R-matrix method was used to study the relation between the S-matrix poles and cross section peaks in low-energy electron scattering from molecules in Schneider [1981]. Further results for particular molecules were obtained by Morgan and Burke [1988], McCartney et al. [1990], Morgan et al. [1990] and Fandreyer et al. [1993] for halogen acids and in Morgan [1998] and Mazevet et al. [2001] for CO_2. Regrettably, the R-matrix codes used in these computations have not been preserved. Recently, a similar R-matrix implementation has been reimplemented by Ragesh Kumar et al. [2022a] for studying

the N-H bond dependence of resonances in pyrrole – the whole complex plane is searched in the recent applications. A different approach employing exterior complex scaling (ECS) was used in Chen et al. [2015] to study the giant dipole resonance in Xenon giant resonance.

Another important step in the mathematical approach was made by Tolstikhin et al. [1998] and Sitnikov and Tolstikhin [2003] who used a slightly different condition

$$\left(\frac{\mathrm{d}}{\mathrm{d}r} - \mathrm{i}k\right) u(r)\bigg|_{r=a} = 0, \tag{3}$$

closed in a region bounded by $r = a$ to define so-called pseudo-Siegert states. This method can solve the quantum scattering problem completely in one and two channels. However, the equations describing the pseudo-Siegert states have to be linearized which does not have a universal solution for N channels. Other mathematical properties of the resonances and S-matrix poles are studied for example in de la Madrid and Gadella [2002] and de la Madrid et al. [2005].

In my bachelor thesis, I implemented a numerical R-matrix approach to solve the time-independent Schrödinger equation in one channel. Here, I extend the codes to the multichannel approach and study multichannel inelastic and long-range model potentials. We study the paths of the poles in the complex plane and test the pole removal in the multichannel problem.

In the final step, we implement our approach to UKRmol+ molecular codes, described in Mašín et al. [2020], to study real molecular systems in electron scattering and photoionization. Our goal is to search for Siegert states in systems where the photoionization cross section (or other observable quantities) indicates the existence of resonances, implement the method of pole removal into the codes, and use it for the analysis. We present a working implementation for electron scattering applications.

This work is structured into four chapters. Chapter 1 summarizes the one-channel approach used in Konvalinka [2021] and the basis theory. In Chapter 2, we describe the multichannel problem and implement the multichannel R-matrix approach and removal of poles of the S-matrix. In Chapter 3, we introduce multichannel inelastic and long-range model potentials and test our numerical approach. Chapter 4 describes implementation of our method into the UKRmol+ codes and applications to molecules.

1. One channel scattering and previous results

This chapter briefly summarizes the results of my bachelor thesis Konvalinka [2021] and serves us as a basic introduction to the theory of Siegert states and the R-matrix method.

1.1 Scattering solution and Siegert states

We follow the basic theory of quantum scattering, see e.g. Friedrich [2016] and Taylor [1972], and solve the time-independent Schrödinger equation

$$\hat{H}\psi(\vec{r}) = \left[-\frac{1}{2}\Delta + V(\vec{r})\right] = E\psi(\mathbf{r}). \tag{1.1}$$

After expanding $\psi(\vec{r})$ into the partial waves $u_l(r)$ and assuming a spherically symmetric potential, the problem reduces to a radial problem

$$\left[\frac{d^2}{dr^2} - \frac{l(l+1)}{r^2} - U(r) + p^2\right] u_l(r) = 0, \tag{1.2}$$

where l denotes an angular momentum, $U(r) = 2V(r)$ is the reduced potential and p momentum of an incoming particle connected to energy by $E = p^2/2$. We considered short-range potentials with the asymptotics

$$V(r) \overset{r\to\infty}{=} O\left(\frac{1}{r^{3+\epsilon}}\right) \quad \epsilon > 0. \tag{1.3}$$

We searched for a scattering solution, i.e. the solution of (1.1) with positive energy $E > 0$, with the boundary condition

$$\psi(\vec{r}) \overset{r\to\infty}{\sim} e^{\mathrm{i}pz} + f(\theta,\phi)\frac{e^{\mathrm{i}pr}}{r}, \tag{1.4}$$

where the coefficient $f(\theta,\phi)$ is the scattering amplitude.

Substituting the asymptotic behaviour of the radial wave

$$u_l(r) \overset{r\to\infty}{=} A\hat{j}_l(pr) + B\hat{n}_l(pr), \tag{1.5}$$

where $\hat{j}_l(\tilde{k}r)$ and $\hat{n}_l(\tilde{k}r)$ are Riccati-Bessel functions and A and B the independent constants, we obtained the phase shift

$$\delta_l = \arctan\left(\frac{B}{A}\right). \tag{1.6}$$

Similarly, the asymptotics

$$u_l(r) \overset{r\to\infty}{\sim} \hat{h}_l^{(-)}(pr) + S(p)\hat{h}_l^{(+)}(pr), \tag{1.7}$$

defines the S-matrix $S(p)$ which is related to the phase shift by $S(p) = e^{2\mathrm{i}\delta_l(p)}$.

The cross section σ of the interaction can be expanded into partial cross sections

$$\sigma = \sum_{l=0}^{\infty} \sigma_l \ , \quad \sigma_l = \frac{4\pi}{2l+1}|f_l|^2, \tag{1.8}$$

which are related to the phase shift and the S-matrix

$$\sigma_l(p) = \frac{4\pi}{p^2}(2l+1)\sin^2\delta_l = \frac{\pi}{p^2}(2l+1)|S(p)-1|^2. \tag{1.9}$$

Finally, Siegert states are solutions of (1.2) with a complex momentum p which coincides with a pole of the S-matrix. This is equivalent to the boundary condition

$$u_l(r) \overset{r\to\infty}{\sim} \hat{h}_l^{(+)}(pr). \tag{1.10}$$

Siegert states are classified into three types:

$$\text{Bound state:} \quad p = \mathrm{i} \mid p \mid,$$

$$\text{Virtual state:} \quad p = -\mathrm{i} \mid p \mid,$$

$$\text{Resonant state:} \quad p = \pm\Re(p) - \mathrm{i} \mid \Im(p) \mid \ , \quad \Im(p) > 0.$$

They have a great importance for analyzing the behaviour of the cross section. For a resonant state with the complex energy $E = E_R - \mathrm{i}\frac{\Gamma}{2}$ close to the real axis, we see a sharp increase (of π approximately) of the phase shift expressed by

$$\delta_{res}(E) = \arcsin\left[\frac{\Gamma/2}{[(E-E_R)^2 + (\Gamma/2)^2]^{\frac{1}{2}}}\right], \tag{1.11}$$

and a characteristic shape of the cross section called the Breit-Wigner resonance.

1.2 R-matrix approach

As a numerical method, we used so-called R-matrix approach explained in Burke [2011] and Descouvemont and Baye [2010]. For numerical integration, we used the Gauss-Legendre quadrature described in Chihara [1978] and Koonin [1986] (source code taken from Burkardt [2020]).

The R-matrix approach consists of separating the space into internal and external regions. In the external region, the solution $u_l^{ext}(r)$ is typically known explicitly. The R-matrix is the Green function computed on the boundary of the internal region, in our case, a sphere of radius $r = a$. We obtain the formula

$$u_l^{ext}(a) = R_l(E)\left.\frac{\mathrm{d}u_l^{ext}(r)}{\mathrm{d}r}\right|_{r=a}, \tag{1.12}$$

which gives us the expression for the S-matrix

$$S(p) = \frac{R_l(E)p\left.\frac{\mathrm{d}\hat{h}_l^{(-)}(z)}{\mathrm{d}z}\right|_{z=pa} - \hat{h}_l^{(-)}(pa)}{R_l(E)p\left.\frac{\mathrm{d}\hat{h}_l^{(+)}(z)}{\mathrm{d}z}\right|_{z=pa} - \hat{h}_l^{(+)}(pa)}. \tag{1.13}$$

In the internal region, we approximate the solution as a sum of B-splines: piecewise polynomial functions described in detail in Bachau et al. [2001]. In this basis of B-splines, we diagonalize the operator $\hat{H}_l + \hat{L}$ where $\hat{H}_l$ is the radial Hamiltonian for a given l and $\hat{L}$ is the Bloch operator that ensures the Hermiticity. The R-matrix is computed as

$$R_l(E) = \frac{1}{2} \sum_{k=1}^{M} \frac{\psi_k(a)\psi_k(a)}{E_k - E}, \tag{1.14}$$

where E_k denote the eigenvalues of $\hat{H}_l + \hat{L}$ and $\psi_k(a)$ are its eigenstates evaluated at point $r = a$.

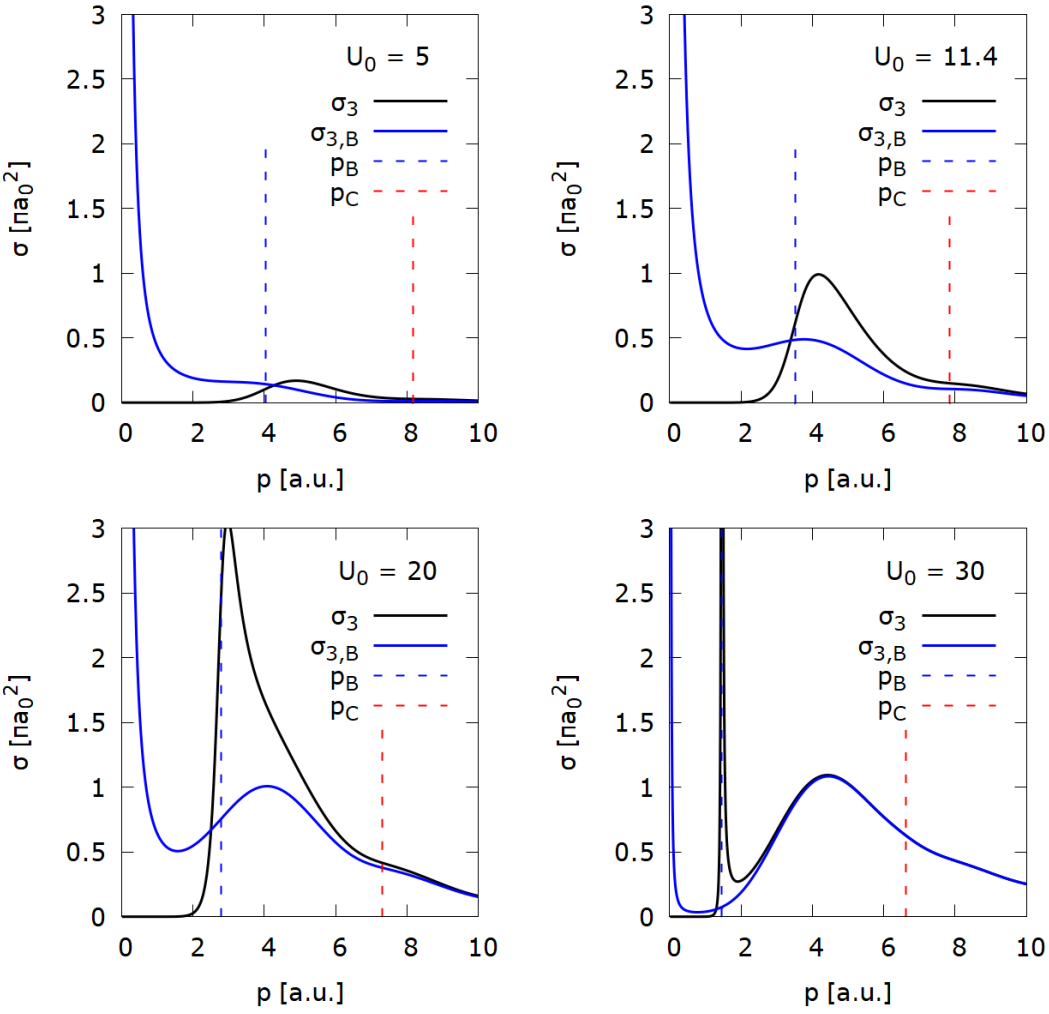

Figure 1.1: Selected results from Konvalinka [2021]. The form of the cross sections $\sigma_3(p)$ and $\sigma_{3,B}(p)$ after removal of the pole B for the chosen values of the potential $U_0 \in \{5,\ 11.4,\ 20,\ 30\}$ *a.u.*, the real parts of resonant poles B and C are denoted by the vertical lines.

1.3 Removal of S-matrix poles

To analyze the results, we removed selected poles of the S-matrix and computed the cross section. The formula for removal was based on the theory of complex

functions explained for example in Kopáček [2010]. A similar approach based on the removal of poles is used in Rakityansky and Elander [2005]. We expect the poles to be simple and we define an S-matrix $S^B(p)$ with a single pole p_B removed

$$S^B(p) = S(p) - \frac{\mathrm{Res}_{p_B} S(p)}{p - p_B}. \tag{1.15}$$

This corresponds to the removal of a single term from the Mittag-Leffler expansion of the function in the same way as in Rakityansky and Elander [2005].

1.4 Model case of a potential well

The simplest case of a spherical rectangular potential well served us well as an illustration of the numerical method and the method of pole removal. We showed how the poles of the S-matrix are found in the complex plane and plotted their trajectories for the depth of the potential well varying. The most relevant result was a comparison of the cross section σ_l and σ_l^B with and without the pole included, respectively. An illustrative example of this is shown in Figure 1.1 with the two cross sections compared for different values of the well-depth U_0 and the angular momentum $l = 3$. As expected, the pole removal has the strongest effect in case of a sharp resonance. My thesis Konvalinka [2021] includes more examples including attempts to isolate the background.

2. Multichannel and R-matrix scattering theory

In this chapter, we introduce the basics of the multichannel collision theory described in Friedrich [2016], Taylor [1972] and Burke [2011]). Then we develop the multichannel R-matrix theory and explain the method of the removal of S-matrix poles.

2.1 Multichannel Schrödinger equation

Let's consider a collision reaction described by

$$e^- + A_i \to e^- + A_j, \tag{2.1}$$

where e^- is an electron and A_i and A_j are the initial and final bound states of the target, respectively.

We describe the whole system by the wave function $\Psi(\xi, \vec{r})$ depending on the coordinates $\vec{r}$ of the free electron and on the internal degrees of freedom ξ of the target system. This wave function satisfies the time-independent Schrödinger equation

$$\hat{H}\Psi(\xi, \vec{r}) = E\Psi(\xi, \vec{r}), \tag{2.2}$$

where the Hamiltonian $\hat{H}$ is expressed as

$$\hat{H} = \hat{H}_\xi - \frac{1}{2}\Delta_{\vec{r}} + V(\xi, \vec{r}), \tag{2.3}$$

i.e. as a sum of an internal Hamiltonian $\hat{H}_\xi$ of the target, the kinetic energy of the electron, and the electron-target interaction $V(\xi, \vec{r})$. We expect that there exist bound states $\Upsilon_i(\xi)$ of the internal Hamiltonian satisfying the equation

$$\hat{H}_\xi \Upsilon_i(\xi) = e_i \Upsilon_i(\xi). \tag{2.4}$$

The eigenenergies e_i are called threshold energies and functions Υ_i target channels. Let's assume that we can expand the wave function in the separable form

$$\Psi(\xi, \mathbf{r}) = \sum_j \Upsilon_j(\xi)\psi_j(\mathbf{r}), \tag{2.5}$$

and insert this expansion into (2.2). We obtain the equation for the single-electron wave functions

$$\sum_j \Upsilon_j(\xi) \left[e_j - E - \frac{1}{2}\Delta_{\mathbf{r}} + V(\xi, \mathbf{r}) \right] \psi_j(\mathbf{r}) = 0. \tag{2.6}$$

We expect the channels to be orthonormal, i.e. $\langle \Upsilon_i | \Upsilon_j \rangle_\xi = \delta_{ij}$. Therefore, we can simplify the equation (2.6) by multiplication by $\Upsilon_i(\xi)$ followed by integration over ξ and thus obtain the set of coupled Schrödinger equations for the channel wave functions $\psi_i(\vec{r})$

$$(e_j - E - \frac{1}{2}\Delta_{\vec{r}})\psi_i(\vec{r}) + \sum_j V_{ij}(\vec{r})\psi_j(\vec{r}) = 0, \tag{2.7}$$

where we define the potential matrix V_{ij} with the components

$$\langle \Upsilon_i | V(\xi, \vec{r}) | \Upsilon_j \rangle_\xi = V_{ij}(\vec{r}) = V_{ji}(\vec{r}). \tag{2.8}$$

For a finite number N_{targ} of channels $\Upsilon_i(\xi)$ of the internal Hamiltonian $\hat{H}_\xi$, the formula (2.8) defines a set of N_{targ} equations for a vector of N_{targ} functions $\psi_i(\vec{r})$

We expand the function ψ_i into the partial waves summing over the angular momentum quantum numbers l_i and m_i

$$\psi_i(r, \theta, \phi) = \sum_{l_i, m_i} \frac{u_{i,l_i m_i}(r)}{r} Y_{l_i m_i}(\theta, \phi), \tag{2.9}$$

where $Y_{l_i m_i}(\theta, \phi)$ are spherical harmonics and $u_{i,l_i m_i}(r)$ radial partial waves for the i-th channel. The spherical harmonics are orthonormal to each other, i.e. $\langle Y_{l_i m_i} | Y_{l_j m_j} \rangle_{\theta,\phi} = \delta_{l_i l_j} \delta_{m_i m_j}$. We multiply (2.7) by $Y^*_{l_i m_i}(\theta, \phi)$ and integrate over θ and ϕ. Thus we obtain the equation

$$\left[\frac{\mathrm{d}^2}{\mathrm{d}r^2} - \frac{l_i(l_i+1)}{r^2} + p_i^2 \right] u_{i,l_i m_i}(r) - \sum_{j, l_j, m_j} \langle Y_{l_i m_i} | U_{ij}(\mathbf{r}) | Y_{l_j m_j} \rangle_{\theta,\phi} u_{j,l_j m_j}(r) = 0, \tag{2.10}$$

where we identify the reduced potential $U_{ij} = 2V_{ij}$ and the channel momentum p_i defined by

$$\frac{p_i^2}{2} = E - e_i. \tag{2.11}$$

We separate the Coulomb long-range term from the potential, i.e. rewrite the components $U_{ij}(\vec{r})$ as

$$U_{ij}(\vec{r}) = \delta_{ij} \frac{-2Z}{r} + \tilde{U}_{ij}(\vec{r}), \tag{2.12}$$

where the rest of the potential is denoted by $\tilde{U}_{ij}$. The Coulomb term is written here for the electron-atom or molecule case where Z denotes the charge of the target. We rewrite the reduced potential term from (2.10) to

$$\langle Y_{l_i m_i} | U_{ij}(\vec{r}) | Y_{l_j m_j} \rangle_{\theta,\phi} = U^{i,l_i m_i}_{j,l_j m_j}(r) = \tilde{U}^{i,l_i m_i}_{j,l_j m_j}(r) + \frac{-2Z}{r} \delta_{ij} \delta_{l_i l_j} \delta_{m_i m_j}. \tag{2.13}$$

Inserting this into the equation (2.10), we obtain the final form

$$\left[\frac{\mathrm{d}^2}{\mathrm{d}r^2} - \frac{-2Z}{r} - \frac{l_i(l_i+1)}{r^2} + p_i^2 \right] u_{i,l_i m_i}(r) - \sum_{j, l_j, m_j} \tilde{U}^{i,l_i m_i}_{j,l_j m_j}(r) u_{j,l_j m_j}(r) = 0. \tag{2.14}$$

In the case of a spherically symmetric potential (independent on θ and ϕ), the radial wave function does not depend on m and the equation (2.14) reduces to

$$\left[\frac{\mathrm{d}^2}{\mathrm{d}r^2} - \frac{-2Z}{r} - \frac{l_i(l_i+1)}{r^2} + p_i^2 \right] u_{i,l}(r) - \sum_j \tilde{U}_{ij}(r) u_{j,l}(r) = 0, \tag{2.15}$$

similar, in form, to the one-channel radial Schrödinger equation.

We define yet another number N_{chan} denoting the total number of channels including the degeneracy of the target channels. The formula (2.14) describes N_{chan} equations for

$$N_{chan} = \sum_{i=1}^{N_{targ}} \sum_{l_i, m_i} 1. \tag{2.16}$$

Here we assume a finite number of angular momenta included in the calculations.

2.2 Scattering solution and the S-matrix

Let's now look at the scattering solution of a multichannel quantum problem. It holds that p_i is a real number (i.e. $p_i^2 \geq 0$) only if $E \geq e_i$. For a given energy E, we split the target channels into two types with respect to their threshold energy e_i:

- Closed channels: $E < e_i$,
- Open channels: $E \geq e_i$.

If there are N_o open target channels and N_c closed target channels it holds $N_o + N_c = N_{targ}$ for the total number of target channels N_{targ}. Including the degeneracy of the target channels, we define number N_o^{chan} for all open channels and number N_c^{chan} for all closed channels: $N_o^{chan} + N_c^{chan} = N_{chan}$.

In the case of a neutral target, the boundary condition in infinity for the wave function corresponding to the reaction (2.1) is

$$\Psi(\xi, \vec{r}) \overset{r\to\infty}{\sim} \Upsilon_i(\xi) e^{\mathrm{i}p_i z} + \sum_{j \text{ open}} \Upsilon_j(\xi) f_{ij}(\theta, \phi) \frac{e^{ip_j r}}{r}, \tag{2.17}$$

where the outgoing term contains only contributions from open channels because only those transitions are energetically allowed. We choose such a coordinate system that the momentum p_i of the incoming particle is in the z-axis direction. The equation (2.17) implies the formula for asymptotics of the function ψ_j in an open channel as

$$\psi_j(\vec{r}) \overset{r\to\infty}{\sim} \delta_{ij} e^{\mathrm{i}p_i z} + f_{ij}(\theta, \phi) \frac{e^{ip_j r}}{r}. \tag{2.18}$$

The problem is more complicated for a charged target, for details, see Friedrich [1990]. The resulting asymptotics of the wave function is

$$\psi_j(\vec{r}) \overset{r\to\infty}{\sim} \delta_{ij} e^{\mathrm{i}[p_i z + \eta_i \ln(k_i[r-z])]} + \left[\delta_{ij} f_{C,i}(\theta) + \tilde{f}_{ij}(\theta, \phi)\right] \frac{e^{\mathrm{i}[p_j r + \eta_j \ln(2k_j r)]}}{r}, \tag{2.19}$$

where the scattering amplitude $f_{C,i}$ for the pure Coulombic potential is separated from the amplitude $\tilde{f}_{ij}$ for the short-range plus Coulombic potential.

We describe the asymptotics of a solution of the equation (2.10) similarly as done in Friedrich [2016]. We assume that the short-range potential $\tilde{U}(\vec{r})$ from (2.12) satisfies the relation

$$\tilde{U}_{ij}(\vec{r}) \overset{r\to\infty}{=} O\left(\frac{1}{r^{2+\epsilon}}\right), \quad \epsilon > 0. \tag{2.20}$$

For this behaviour of the potential, we asymptotically obtain two linearly independent solutions

$$\phi_{i,l_i}^{(\pm)}(pr) \overset{r\to\infty}{\sim} \sqrt{\frac{2}{\pi p}} e^{\pm \mathrm{i}\Theta_{i,l_i}(r)}, \tag{2.21}$$

where $\Theta_{i,l_i}(r)$ is an argument of the imaginary exponential expressed by

$$\Theta_{i,l_i}(r) = p_i r - \frac{l_i \pi}{2} - \eta_i \ln 2 p_i r + \sigma_{l_i}, \tag{2.22}$$

where

$$\eta_i = -\frac{Z}{p_i}, \tag{2.23}$$

and

$$\sigma_{l_i} = \mathrm{arg}\Gamma(l_i + 1 + \mathrm{i}\eta_i). \tag{2.24}$$

For $Z = 0$, the formula (2.22) simplifies to

$$\Theta_{i,l_i}(r) = p_i r - \frac{l_i \pi}{2}. \tag{2.25}$$

In the case of a neutral target, the functions $\phi_l^{(\pm)}(pr)$ are identified with the Riccati-Hankel functions $\hat{h}_{l_i}^{(\pm)}(p_i r)$. In the general case of a charged target, the functions are identified with the Coulomb-Hankel functions $H_{l_i}^{(\pm)}(\eta_i; p_i r)$, described in Thompson and Barnett [1985].

For a given energy E, we obtain as many independent vectors ϕ_i of solutions as there are open channels. We denote each component $u_{j,l_j m_j}^{i,l_i m_i}$ where the bottom set of indices denotes the independent solutions and the upper set denotes the components in all channels. Equivalently, we deal with $N_{chan} \times N_o^{chan}$ matrices $\mathbf{u}$ with the components $u_{j,l_j m_j}^{i,l_i m_i}$ instead of N_o^{chan} vectors with components $u_{j,l_j m_j}$.

The expansion (2.9) and the asymptotic condition (2.18) and (2.19), respectively, imply the asymptotic conditions for the partial waves, see Friedrich [2016],

$$u_{j,l_j m_j}^{i,l_i m_i}(r) \overset{r\to\infty}{\sim} e^{-\mathrm{i}\Theta_{i,l_i}(r)}\delta_{ij}\delta_{l_i l_j}\delta_{m_i m_j} - e^{+\mathrm{i}\Theta_{j,l_j}(r)} S_{j,l_j m_j}^{i,l_i m_i},\ j,i = 1,..,N_o, \tag{2.26}$$

$$u_{j,l_j m_j}^{i,l_i m_i}(r) \overset{r\to\infty}{\sim} 0,\ j = N_o + 1,..,N_{targ}, \quad i = 1,..,N_o, \tag{2.27}$$

where $S_{j,l_j m_j}^{i,l_i m_i}$ are components of the open-channel S-matrix and Θ_{i,l_i} is the function from (2.22) for a given p_i. We distinguish between the asymptotics for closed and open channels. For the $N_o^{chan} \times N_o^{chan}$ submatrix $\bar{\mathbf{u}}$ being the open-channel part of the matrix $\mathbf{u}$, we rewrite the equation (2.26) in a matrix form

$$\bar{\mathbf{u}} \overset{r\to\infty}{\sim} e^{-\mathrm{i}\boldsymbol{\Theta}(r)} - e^{+\mathrm{i}\boldsymbol{\Theta}(r)}\mathbf{S}, \tag{2.28}$$

where $\bar{\mathbf{u}}$, $\mathbf{S}$, and $\boldsymbol{\Theta}$ are $N_o^{chan} \times N_o^{chan}$ matrices ($\boldsymbol{\Theta}$ is diagonal). Using the linearly independent functions (2.21), we get

$$\bar{\mathbf{u}} \overset{r\to\infty}{\sim} \boldsymbol{\Phi}^{(-)} - \boldsymbol{\Phi}^{(+)}\mathbf{S}, \tag{2.29}$$

where $\boldsymbol{\Phi}^{(\pm)}$ are diagonal matrices with components $\phi_{l_i}^{(\pm)}(p_i r)$.

2.2.1 Eigenphases

Phase shift is in one channel defined by the expression $S = e^{2\mathrm{i}\delta}$. In multichannel scattering, we do not compute $(N_o^{chan})^2$ phase shifts from each S-matrix component as one could expect. Instead, we use so-called eigenphases δ_i indexed by $i = 1, ..., N_o^{chan}$. These are calculated by diagonalization of the S-matrix, which is unitary, so it can be diagonalized by a real symmetric matrix. That gives us the set of eigenvalues expressed by $\{\exp(2\mathrm{i}\delta_i)\}_{i=1}^{N_o^{chan}}$. These define the eigenphases δ_i up to the 2π shift. The eigenphases can be used to compute the eigenphase sum

$$\delta = \sum_{i=1}^{N_o^{chan}} \delta_i. \tag{2.30}$$

2.2.2 Cross section

Let's begin with the equations (2.18) and (2.19) determining the shape of the wave function asymptotics. We compute the differential $\frac{\mathrm{d}\sigma_{i\to j}}{\mathrm{d}\Omega}$ or integral $\sigma_{i\to j}$ integral cross section of a transition between an initial state Υ_i to a final state Υ_j as shown in Friedrich [2016]

$$\frac{\mathrm{d}\sigma_{i\to j}}{\mathrm{d}\Omega} = \frac{p_j}{p_i}|f_{ij}(\theta,\phi)|^2 \quad , \; \sigma_{i\to j} = \frac{p_j}{p_i}\int |f_{ij}(\theta,\phi)|^2 \mathrm{d}\Omega, \tag{2.31}$$

and the total cross section

$$\sigma = \sum_{j \text{ open}} \sigma_{i\to j}. \tag{2.32}$$

Neutral target

For a neutral target, we proceed similarly as in the one-channel case and obtain the formula for the scattering amplitudes

$$f_{ij}(\theta,\phi) = \sum_{l_j,m_j} Y_{l_j m_j}(\theta,\phi) \sum_{l_i} \mathrm{i}^{l_i-l_j-1}\sqrt{\frac{\pi(2l_i+1)}{p_i p_j}}(S^{i,l_i 0}_{j,l_j m_j} - \delta_{ij}\delta_{l_i l_j}\delta_{0m_j}), \tag{2.33}$$

and thus also the relation between the cross section $\sigma_{i\to j}$ from (2.31) and the components of the S-matrix

$$\begin{aligned}\sigma_{i\to j} =& \frac{\pi}{p_i^2}\sum_{l_1,l_2} \mathrm{i}^{l_2-l_1}\sqrt{(2l_1+1)(2l_2+1)} \\ &\times \sum_{l_j,m_j}\left[(S^{i,l_1 0}_{j,l_j m_j})^* - \delta_{ij}\delta_{l_1 l_j}\delta_{0m_j}\right]\left[S^{i,l_2 0}_{j,l_j m_j} - \delta_{ij}\delta_{l_2 l_j}\delta_{0m_j}\right].\end{aligned} \tag{2.34}$$

Computation of the formula (2.34) simplifies when we consider only a few partial waves and channels which is the usual case in practice.

Charged target

If the target is charged, we expand the scattering amplitudes f_{ij} into two terms

$$f_{ij}(\theta,\phi) = \delta_{ij} f_{C,i}(\theta) + \tilde{f}_{ij}(\theta,\phi), \tag{2.35}$$

where $f_{C,i}$ is the Coulomb scattering amplitude connected with the long-range Coulomb potential and $\tilde{f}_{ij}$ denotes the additional scattering amplitude connected with the short-range plus Coulombic potential from (2.13).

The amplitude $f_{C,i}$ is the solution of the scattering on a pure Coulomb potential. From Friedrich [1990], we get the formula

$$f_{C,i} = \frac{-\eta_i}{2p_i \sin^2\frac{\theta}{2}} e^{\mathrm{i}\left[\eta_i \ln(\sin^2\frac{\theta}{2}) - 2\sigma_{i,l=0}\right)}. \tag{2.36}$$

The formula for the additional amplitudes $\tilde{f}_{ij}$ is similar to the case of a neutral target except for the additional Coulomb phases:

$$\tilde{f}_{ij}(\theta,\phi) = \sum_{l_j,m_j} Y_{l_j m_j}(\theta,\phi) \sum_{l_i} \mathrm{i}^{l_i-l_j-1} e^{\mathrm{i}(\sigma_{l_i,i}-\sigma_{l_j,j})}\sqrt{\frac{\pi(2l_i+1)}{p_i p_j}}(S^{i,l_i 0}_{j,l_j m_j} - \delta_{ij}\delta_{l_i l_j}\delta_{0m_j}), \tag{2.37}$$

where the S-matrix is asymptotically determined relative to the pure Coulomb scattering problem and $\sigma_{l_i,i}$, $\sigma_{l_j,j}$ are given by (2.24).

Similarly as Friedrich [2016], we rewrite the differential cross section (2.31)

$$\frac{\mathrm{d}\sigma_{i\to i}}{\mathrm{d}\Omega} = |f_{C,i}(\theta) + \tilde{f}_{ii}(\theta,\phi)|^2, \tag{2.38}$$

for elastic scattering and

$$\frac{\mathrm{d}\sigma_{i\to j}}{\mathrm{d}\Omega} = \frac{p_j}{p_i}|\tilde{f}_{ii}(\theta,\phi)|^2 \ , \quad j \neq i, \tag{2.39}$$

for the inelastic case.

2.2.3 Riemann sheets of the first type

In this subsection, we look in detail at the target channel momenta p_i given by the formula (2.11) and describe Riemann sheets of the complex plane of energies for the multichannel problem. There is an ambiguity of signs in the explicit expression for the channel momenta

$$p_i = \pm\sqrt{2(E-e_i)}. \tag{2.40}$$

For N channels, $2^{N_{targ}}$ combinations of these signs are possible and thus the S-matrix has $2^{N_{targ}}$ different values for each combination. In the complex plane of energy E, we introduce $2^{N_{targ}}$ so-called Riemann sheets, each for one combination of signs. Our working title will be Riemann sheets of the first type (we are going to deal with a different type of sheets in what follows).

Following Burke [2011], we denote the sheets in the same way. The physical sheet P is defined by

$$\mathrm{Im}(p_i) > 0 \ , \quad i = 1,..,N_{targ}. \tag{2.41}$$

The bound states are located only on the sheet P, no resonant or virtual states are on P. We define the sheets U_m by the condition

$$\begin{aligned} &\mathrm{Im}(p_i) < 0 \ , \quad i = 1,..,m \ \ , \\ &\mathrm{Im}(p_i) > 0 \ , \quad i = m+1,..,N_{targ}, \end{aligned} \tag{2.42}$$

i.e. the physical sheet is equivalent to U_0.

Each sheet has a branch cut on the real axis of E between e_1 and $+\infty$. Crossing the positive real axis on the interval (e_m, e_{m+1}) means crossing to another sheet. Considering this, it is reasonable to specifically define the sheets U_m because these sheets are the "closest" to the physical sheet.

Let's explain this behaviour in Figure 2.1 for the simple example of $N_{targ} = 2$, i.e. $2^{N_{targ}} = 4$ describes four possible trajectories from E on the physical sheet P to its complex conjugation E^*. The trajectory denoted (0) goes around the branch cut and reaches E^* still on P, the path (1) crosses the branch cut between e_1 and e_2 and reaches E^* on U_1 and the path (2) similarly ends on U_2. Finally, the path $(1,2)$ goes to U_1 at first and then ends at E^* on the last non-physical sheet which we denote as $U_{1,2}$.

In the case of one channel, we had to consider two different sheets – P and U_1 – but these can be united into one by mapping values of the S-matrix on the momentum complex plane. This is not possible to do in more channels.

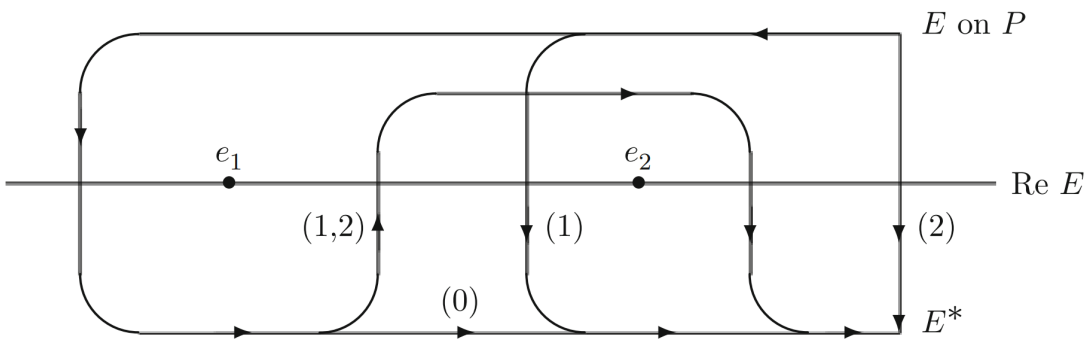

Figure 2.1: The scheme of four possible continuous paths in the complex plane from E on the physical sheet P to E^* for $N_{targ} = 2$ where e_i denotes threshold energies. Each path is equivalent to reaching the energy E^* on a different Riemann sheet (the scheme is taken from Burke [2011]).

2.2.4 Multichannel Siegert states

The Siegert states are defined as poles of the S-matrix by the energy E_0 where the function $\mathbf{S}$ has a pole. It is equivalent to finding functions satisfying the asymptotics

$$\mathbf{u} \overset{r\to\infty}{\sim} \mathbf{\Phi}^{(+)}. \tag{2.43}$$

In Konvalinka [2021], we distinguished three types of Siegert states with respect to the momentum of the state (see 1.1). In the multichannel case, the definition of the virtual and bound states is a bit tricky because of the various Riemann sheets:

$$\begin{aligned} \text{Bound state:} \quad & E \in \mathbb{R}, \text{ on the sheet } P, \\ \text{Virtual state:} \quad & E \in \mathbb{R}, \text{ on any other sheet}, \\ \text{Resonant state:} \quad & E = \Re(E) \pm \mathrm{i} \mid \Im(E) \mid , \quad \Im(E) \neq 0. \end{aligned}$$

The resonances occur every time in pairs and, on the plane of momentum, we are interested only in the poles with $\Re(p) > 0$ that are close to the positive real axis of momentum and so are connected with peaks of the cross section. These poles are projected on the poles with $\Im(E) < 0$ so we search for the poles only on the lower half plane of the complex plane of energies.

Resonances and Riemann sheets

The consequence of the behaviour described in 2.2.3 is that we have to look for the poles of the S-matrix more carefully because they occur on all the $2^{N_{targ}}$ sheets we are dealing with. Nevertheless, the most important sheets are the sheets U_m because the strong resonant peaks are visible only for resonances "close" to the real axis of the physical sheet.

Let's explain a simple example showing that a resonance occurring on U_m for some $m \in \{1, .., N_{targ}\}$ is "close" to the real axis of the physical sheet $P = U_0$. We compare U_m with a sheet V_m defined by the condition

$$\begin{aligned} &\mathrm{Im}(p_i) < 0 \ , \quad i = m \ , \\ &\mathrm{Im}(p_i) > 0 \ , \quad i = 1, ..m-1, m+1, .., N_{targ}. \end{aligned} \tag{2.44}$$

Looking for resonances in the target channel A_m, one could intuitively choose the sheet V_m. However, in Figure 2.2 we show that the poles on V_m are much further from the real axis of the physical sheet.

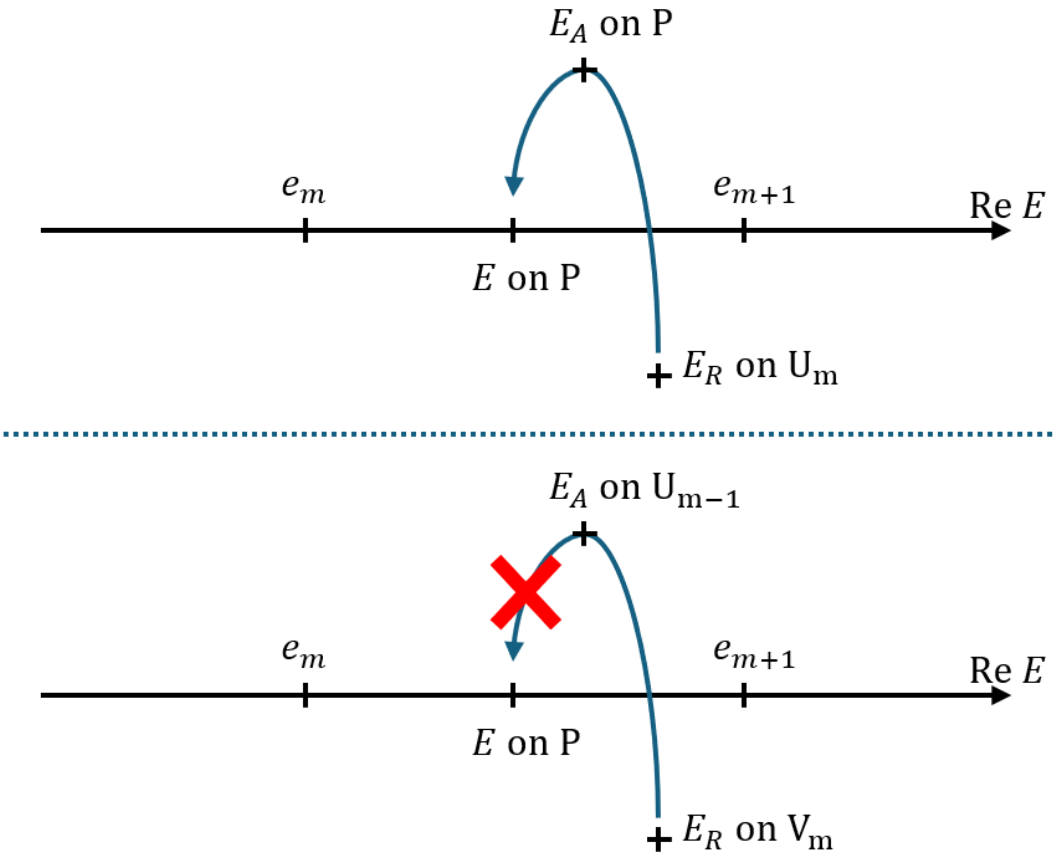

Figure 2.2: Different paths from resonance on U_m and V_m to the energy E on the real axis on the physical sheet P.

Let's assume that there is a resonance on U_m and on V_m and our goal is to find the path to the real axis of the physical sheet. In addition, we need to get to the real axis from the upper side which is equivalent to reaching the positive real axis of momentum (reaching the real axis on P is equivalent to reaching the negative axis of momentum). Figure 2.2 shows that this can be simply done for the path from the resonance on U_m with just one crossing of the real axis of E. On the other hand, we can not do the same for V_m. Moreover, it is evident that the sheets U_m are the only sheets neighboring the physical sheet P (crossing the real axis from P gets us every time to some U_m), i.e. all the poles that are close to the real axis and influence the cross section have to lie on U_m. The problem of looking for resonances is thus simplified because we do not have to go through all the $2^{N_{targ}}$ possibilities – it is sufficient to look only at U_m.

2.3 Multichannel R-matrix approach

In this section, we describe the derivation of the R-matrix approach for the multichannel case as an extension of the one-channel case from Konvalinka [2021]. A detailed discussion can be found in Burke [2011].

We define an R-matrix sphere of radius a which splits the space into an internal and an external region. The R-matrix radius is typically chosen so that the solution $(u_j^i)^{ext}$ in the external region is known analytically. In the internal region given by the condition $r \leq a$, we expand the wave function in an orthonormal basis

$$(u_j^i)^{int} = \sum_{m=1}^{M} (c_j^i)_m f_m(r) \ , \quad r < a, \tag{2.45}$$

as a linear combination of M orthonormal basis functions $f_m(r)$. For convenience, we omit the indices l and m and merge them into the index i and write the radial wave function as $u_j^i(r)$ instead of the notation in (2.26). Similarly, we will write $U_{ij}(r)$ for the potential components in (2.13). We also write the numbers of channels N_{chan} as N and N_o^{chan} as N_o.

In the equation (2.45), the index i labels the independent solutions. The $N \times N_o$ matrix $\mathbf{u}$ thus consists of N_o columns $\vec{u}_j$ of dimension N

$$\mathbf{u} = \left(\vec{u}_j \ , \quad \vec{u}_j \ , \quad \cdots \ , \quad \vec{u}_{N_o}\right) \quad , \quad \vec{u}_j = \begin{pmatrix} u_j^1 \\ u_j^2 \\ \vdots \\ u_j^N \end{pmatrix}. \tag{2.46}$$

The equation (2.10) is expressed as

$$\sum_{k=1}^{M} \hat{h}_{ik} u_j^k + E u_j^i = 0, \tag{2.47}$$

where

$$\hat{h}_{ij} = \delta_{ij} \left[\frac{1}{2} \frac{\mathrm{d}^2}{\mathrm{d}r^2} - \frac{l_i(l_i+1)}{2r^2} - e_i \right] - 2U_{ij}(r). \tag{2.48}$$

We see that $\hat{h}_{ij} = -2U_{ij}(r)$ for $i \neq j$. The equation (2.47) is expressed in a matrix form by

$$(\mathbf{h} - E)\mathbf{u} = 0, \tag{2.49}$$

where $\mathbf{h}$ is an $N \times N$ matrix and E is a scalar.

Let's now define the Bloch operator

$$\hat{l}_{ij} = \delta_{ij} \frac{1}{2} \delta(r-a) \frac{\mathrm{d}}{\mathrm{d}r}. \tag{2.50}$$

This expression can be rewritten in terms of $N \times N$ matrix $\mathbf{l}$ which acts on the matrix $\mathbf{u}$. The factor δ_{ij} originates in the requirement of Hermiticity of the kinetic energy operator. Adding the operator to the Hamiltonian ensures the Hermiticity of the whole sum $\mathbf{h} + \mathbf{l}$ as shown in Konvalinka [2021].

The requirement of continuity of the wave function derivative can be written as

$$\mathbf{l}\mathbf{u}^{int} = \mathbf{l}\mathbf{u}^{ext}. \tag{2.51}$$

Inclusion of this condition into the equation (2.47) gives us the formula

$$(\mathbf{h}+\mathbf{l}-E)\mathbf{u}^{int}=\mathbf{l}\mathbf{u}^{ext}, \tag{2.52}$$

and subsequently

$$\mathbf{u}^{int}=(\mathbf{h}+\mathbf{l}-E)^{-1}\mathbf{l}\mathbf{u}^{ext}=-\frac{1}{2}\mathbf{G}(E;r,a)\frac{\mathrm{d}\mathbf{u}^{ext}}{\mathrm{d}r}\bigg|_{r=a}. \tag{2.53}$$

In the last equation, we used (2.50) to evaluate $\mathbf{l}\mathbf{u}^{ext}$. The Green function $\mathbf{G}(E;r)$ is defined as an $N\times N$ matrix

$$\mathbf{G}(E;r,a)=-(\mathbf{h}+\mathbf{l}-E)^{-1}. \tag{2.54}$$

We evaluate the equation (2.53) at the point $r=a$ where the internal and external solution must be equal to each other and we obtain the relation

$$\mathbf{u}^{ext}=\mathbf{R}\frac{\mathrm{d}\mathbf{u}^{ext}}{\mathrm{d}r}\bigg|_{r=a}, \tag{2.55}$$

where we define the $N\times N$ dimensional R-matrix $\mathbf{R}$ as

$$2\mathbf{R}=-\mathbf{G}(E;r=a). \tag{2.56}$$

In correspondence with the equation (2.29), we assume that we know the open-channel solution $\bar{\mathbf{u}}^{ext}$ in the external region (for $r>a$) and we write it in the form of $N_o\times N_o$ matrices

$$\bar{\mathbf{u}}^{ext}\overset{r\to\infty}{\sim}\mathbf{\Phi}^{(+)}-\mathbf{\Phi}^{(-)}\mathbf{S}. \tag{2.57}$$

Including this condition into (2.55) and taking the $N_o\times N_o$ submatrix $\bar{\mathbf{R}}$ of the R-matrix $\mathbf{R}$, we compute the $N_o\times N_o$ S-matrix

$$\mathbf{S}(E)=\left(\bar{\mathbf{R}}\frac{\mathrm{d}\mathbf{\Phi}^{(+)}}{\mathrm{d}r}\bigg|_{r=a}-\mathbf{\Phi}^{(+)}\right)^{-1}\left(\bar{\mathbf{R}}\frac{\mathrm{d}\mathbf{\Phi}^{(-)}}{\mathrm{d}r}\bigg|_{r=a}-\mathbf{\Phi}^{(-)}\right). \tag{2.58}$$

Siegert states are located as zeros of the function

$$F(E)=\det\left[\bar{\mathbf{R}}\frac{\mathrm{d}\mathbf{\Phi}^{(+)}}{\mathrm{d}r}\bigg|_{r=a}-\mathbf{\Phi}^{(+)}\right]. \tag{2.59}$$

2.3.1 Computation of the R-matrix in the basis of B-splines

In the following, we describe the computation of the R-matrix (2.56) using the specific basis of B-splines $\{B_m(r)\}_{m=1}^{M}$. The procedure is analogous to the one-channel case, more details about B-splines are to be found in Bachau et al. [2001].

At first, we want to orthonormalize our basis (B-splines are not orthonormal functions). We calculate the overlap integrals as

$$O_{mn}=\langle B_m|B_n\rangle=\int_0^a B_m(r)B_n(r)\mathrm{d}r. \tag{2.60}$$

These are components of a real symmetric $M \times M$ matrix $\mathbf{O}$ which can be diagonalized as

$$\mathbf{O} = \mathbf{A}^{+}\mathbf{diag}(d_1, ..., d_M)\mathbf{A}, \tag{2.61}$$

where $\mathbf{diag}(d_1, ..., d_M)$ is a diagonal matrix consisting of the eigenvalues d_i of $\mathbf{O}$ and $\mathbf{A}$ is a unitary matrix consisting of the eigenvectors of $\mathbf{O}$. Let's define a new basis of functions $\tilde{B}_m(r)$ by a linear transformation

$$\tilde{B}_m(r) = \sum_{n=1}^{M} \frac{A_{nm} B_n(r)}{\sqrt{d_m}}. \tag{2.62}$$

This new basis is orthonormal and the new overlap matrix $\tilde{\mathbf{O}}$ in this basis is the unit matrix

$$\tilde{O}_{mn} = \langle \tilde{B}_m | \tilde{B}_n \rangle = \delta_{mn}, \tag{2.63}$$

which was a basic assumption in the implementation of the R-matrix approach in the previous section.

Including this into (2.45), we express the radial wave function in the internal region in the new basis by

$$(u_j^i)^{int} = \sum_{m=1}^{M} (c_j^i)_m \tilde{B}_m(r) \ , \quad r < a, \tag{2.64}$$

where each component u_j^i is represented by a vector $\vec{c}_j^{\,i}$ with M components $(c_j^i)_m$.

We express the operator (2.48) in the basis of B-splines. Each component $\hat{h}_{ij}$ of the multichannel Hamiltonian is in the basis expressed by the $M \times M$ matrix $\mathbf{h}_{ij}$ of the components

$$(h_{ij})_{mn} = \langle \tilde{B}_m | \hat{h}_{ij} | \tilde{B}_n \rangle_r = \int_0^a \tilde{B}_m \hat{h}_{ij} \tilde{B}_n \mathrm{d}r. \tag{2.65}$$

Merging the expressions (2.64) and (2.65) into the equation (2.47), we obtain a matrix formula

$$\sum_{k=1}^{N} \mathbf{h}_{ik} \vec{c}_j^{\,k} + E \vec{c}_j^{\,i} = 0. \tag{2.66}$$

Now, we will express the equation (2.49) in terms of B-splines. The $N \times N$ matrix $\mathbf{h}$ is in the basis represented by the $MN \times MN$ matrix

$$\mathbf{H} = \begin{pmatrix} \mathbf{h}_{11} & \mathbf{h}_{12} & \cdots & \mathbf{h}_{1N} \\ \mathbf{h}_{21} & \mathbf{h}_{22} & \cdots & \mathbf{h}_{2N} \\ \vdots & \vdots & \ddots & \vdots \\ \mathbf{h}_{N1} & \mathbf{h}_{N2} & \cdots & \mathbf{h}_{NN} \end{pmatrix}. \tag{2.67}$$

The N-dimensional independent solutions $\vec{u}_j$ are in the B-spline basis represented by MN-dimensional vectors as

$$\vec{u}_j \longrightarrow \begin{pmatrix} \vec{c}_j^{\,1} \\ \vec{c}_j^{\,2} \\ \vdots \\ \vec{c}_j^{\,N} \end{pmatrix}, \tag{2.68}$$

and the $N \times N_o$ wave function matrix $\mathbf{u}$ is represented by the $MN \times N_o$ matrix

$$\mathbf{c} = \begin{pmatrix} \vec{c}_1^{\,1} & \vec{c}_2^{\,1} & \cdots & \vec{c}_{N_o}^{\,1} \\ \vec{c}_1^{\,2} & \vec{c}_2^{\,2} & \cdots & \vec{c}_{N_o}^{\,2} \\ \vdots & \vdots & \ddots & \vdots \\ \vec{c}_1^{\,N} & \vec{c}_2^{\,N} & \cdots & \vec{c}_{N_o}^{\,2} \end{pmatrix}. \tag{2.69}$$

The equation (2.49) is then expressed by

$$(\mathbf{H} - E)\mathbf{c} = 0. \tag{2.70}$$

Thus we introduced MN equations for N_o independent vectors of MN components. In the same way, we represent $\mathbf{l}$ by the $MN \times MN$ matrix $\mathbf{L}$ in our basis.

Thanks to the Hermiticity of $(\mathbf{H} + \mathbf{L})$, we can diagonalize this matrix as

$$\mathbf{H} + \mathbf{L} = \mathbf{U}^{+}\mathbf{diag}(E_1, ..., E_{MN})\mathbf{U}, \tag{2.71}$$

and obtain the set of eigenvalues (called R-matrix energies) and eigenfunctions $\{E_k, \psi_k(r)\}_{k=1}^{MN}$. In (2.71), $\mathbf{U}$ is a unitary matrix consisting of the eigenvectors of $(\mathbf{H} + \mathbf{L})$ and $\mathbf{diag}(E_1, ..., E_{MN})$ is a diagonal matrix consisting of the eigenvalues. The eigenfunctions $\psi(r)$ are in the B-spline basis represented by the MN-dimensional vectors, columns of $\mathbf{U}$

$$\psi_k(r) \longrightarrow \begin{pmatrix} U_{1,k} \\ U_{2,k} \\ \vdots \\ U_{MN,k} \end{pmatrix}, \tag{2.72}$$

and we express them by the formula

$$\psi_k(r) = \sum_{j=1}^{N} \sum_{m=1}^{M} U_{(j-1)M+m,k} \tilde{B}_m(r). \tag{2.73}$$

We can interpret this equation as consisting of N M-dimensional vectors

$$\begin{pmatrix} U_{(j-1)M+1,k} \\ U_{(j-1)M+2,k} \\ \vdots \\ U_{(j-1)M+M,k} \end{pmatrix}, \tag{2.74}$$

each representing a projection of the function $\psi_k(r)$ to the j-th channel. We define the surface amplitudes $w_k^{j'}$ as projections of $\psi_k(r)$ on the individual channels on the surface of the R-matrix sphere expressed by

$$w_k^{j'} = \psi_k^{j'}(a) = \sum_{m=1}^{M} U_{(j'-1)M+m,k} \tilde{B}_m(a). \tag{2.75}$$

Using the eigensystem and the surface amplitudes, we express the equation (2.53) as

$$(u_j^i)^{int}(r) = \frac{1}{2} \sum_{m'=1}^{M} \sum_{j'=1}^{N} \sum_{k=1}^{MN} U_{(j-1)M+m',k} \tilde{B}_{m'}(r) \frac{1}{E_k - E} w_k^{j'} \left. \frac{\mathrm{d}(u_{j'}^i)^{ext}}{\mathrm{d}r} \right|_{r=a}. \tag{2.76}$$

To express the components of the matrix $\mathbf{c}$, we rewrite (2.76) as

$$(c_j^i)_m = \frac{1}{2}\sum_{j'=1}^{N}\sum_{k=1}^{MN} U_{(j-1)M+m,k}\frac{1}{E_k - E}w_{j'}^k \frac{\mathrm{d}(u_{j'}^i)^{ext}}{\mathrm{d}r}\bigg|_{r=a}. \tag{2.77}$$

The coefficients can be used in the formula (2.64) to explicitly evaluate the internal solution once the external one is known.

Setting $r = a$ in (2.76), we obtain the relation

$$(u_j^i)^{ext} = \sum_{j'=1}^{N}\sum_{k=1}^{MN}\frac{1}{2}\frac{w_k^j w_k^{j'}}{E_k - E}\frac{\mathrm{d}(u_{j'}^i)^{ext}}{\mathrm{d}r} = \mathbf{R}\frac{\mathrm{d}\mathbf{u}^{ext}}{\mathrm{d}r}\bigg|_{r=a}, \quad (u_j^i)^{ext} = \sum_{j'=1}^{N} R_{jj'}\frac{\mathrm{d}(u_{j'}^i)^{ext}}{\mathrm{d}r}, \tag{2.78}$$

where we define the R-matrix components as

$$R_{jj'} = \sum_{k=1}^{MN}\frac{1}{2}\frac{w_k^j w_k^{j'}}{E_k - E}. \tag{2.79}$$

Thus we obtained the equation (2.78) as an expression of the equation (2.55) and the formula (2.79) for evaluating the R-matrix components.

Wave function in the internal region

If we want to express the wave function $(u_i^j)^{int}(r)$ in the internal region we have to use explicitly the equation (2.77) to calculate the coefficients $(c_j^i)_m$. Then we calculate the wave function $(u_i^j)^{int}(r)$ using the formula (2.64).

However, it is necessary to calculate the S-matrix to obtain the external solution $\mathbf{u}^{ext}$ at first and then continue with the calculation of $(c_j^i)_m$.

The problem simplifies if one needs to calculate the wave function of the Siegert state. The external solution is then proportional to the function $\hat{h}_l^{(+)}(pr)$ or $H_l^{(+)}(\eta, pr)$, respectively, and the S-matrix is not needed in this case but we need to know the complex energy (momentum) of the Siegert state.

Searching for the bound states

In the case of a sufficiently large a and a correspondingly dense basis of B-splines, the diagonalization generates R-matrix energies E_k that are very close to the energies of bound states which can cause a numerical problem.

Let's have a bound state E_B and an R-matrix energy $E_r \sim E_B$. If we search for this bound state in the complex plane using the implicit function (2.59) then the term $\frac{w_r^j w_r^{j'}}{E_r - E}$ diverges for E close to E_B.

It is important to keep this in mind when we search for the bound states. This numerical problem is solved for example in Burke and Seaton [1984]. In our application, we did not encounter it.

2.4 Removal of poles in multichannel problem

By a straightforward extension of Konvalinka [2021], we remove individual poles of the S-matrix using their complex residues using the formula similar to (1.15).

The only difference is that the S-matrix has N_o^2 components and so we have to compute all of N_o^2 residues for each component. We also use the S-matrix as a function of the energy so the removal is based on the Mittag-Leffler expansion with respect to the energy. In the end, to obtain the transformed S-matrix S_{ij}^B with a pole of an energy E_B removed, we use the formula

$$S_{ij}^B(E) = S_{ij}(E) - \frac{\mathrm{Res}_{E_B} S_{ij}(E)}{E - E_B}. \tag{2.80}$$

The complex residue $\mathrm{Res}_{E_B} S(E)$ is obtained from

$$\mathrm{Res}_{E_B} S_{ij}(B) = \frac{1}{2\pi \mathrm{i}} \oint_C S_{ij}(E)\mathrm{d}E = \frac{1}{2\pi} \int_0^{2\pi} S_{ij}(E_B + \varepsilon e^{\mathrm{i}\phi}) \varepsilon e^{\mathrm{i}\phi} \mathrm{d}\phi, \tag{2.81}$$

where we integrate over a curve C enclosing the pole at E_B (but no other S-matrix pole at the same time).

As we mentioned above in 2.2.4, resonances occur in pairs and we are interested in the poles with $E = \Re(E) - \mathrm{i} \mid \Im(E) \mid$. Using the same logic, we remove only these poles.

2.4.1 Partial widths

The search of poles gives us only the total width Γ of the resonance but not the decay widths into the individual channels. To obtain these widths we use the approach introduced in Taylor [1972] (a similar method is used in Shimamura [2011]).

Let's assume a resonance at $E_B = E_R - \mathrm{i}\frac{\Gamma}{2}$ lying close to the real axis. In accordance to Taylor [1972], the S-matrix in the vicinity of E_B is given by

$$S_{ij}(E) = S_{ij}^B + \frac{\mathrm{Res}_{E_B} S_{ij}(E)}{E - E_R + \mathrm{i}\frac{\Gamma}{2}}, \tag{2.82}$$

where we separate it into the resonant contribution and the background S-matrix S^B. We rewrite this expression as

$$\mathbf{S}(E) = \mathbf{S^B} \left(1 - \frac{\mathrm{i}\mathbf{A}}{E - E_R + \mathrm{i}\frac{\Gamma}{2}}\right), \tag{2.83}$$

where the components of the matrix $\mathbf{A}$ have the form

$$A_{ij} = \delta_i \delta_j^*. \tag{2.84}$$

We calculate $\mathbf{A}$ from the matrix equation

$$\mathbf{A} = \mathrm{i}\left(\mathbf{S^B}\right)^{-1} \mathbf{Res}_{E_B} \mathbf{S}. \tag{2.85}$$

The quantity $\Gamma_i := A_{ii} = |\delta_i|^2$ is called the partial width of the resonance for channel i. In the multichannel problem, it is interpreted as a rate of influence of the resonance on the individual channels. The partial widths and the width Γ of the resonance are related by

$$\Gamma = \sum_{i=1}^{N} \Gamma_i. \tag{2.86}$$

3. Model multichannel problems with short- and long-range potentials

In this part, we develop our numerical approach and test it on analytically solvable models of multichannel problems employing short-range and long-range potentials.

3.1 Spherical potential well and the Feshbach resonance

The first problem that we solved was the case of a rectangular potential well; the two-channel case is in Grozdanov and McCarroll [2007]. We located resonances arising in the two-channel case of the spherical potential well given by

$$\begin{aligned} \tilde{U}(r) &= \begin{pmatrix} -4 & -1 \\ -1 & -4 \end{pmatrix} , \quad r \leq a, \\ \tilde{U}(r) &= \begin{pmatrix} 0 & 0 \\ 0 & 0 \end{pmatrix} , \quad r > a, \end{aligned} \tag{3.1}$$

with a representing both the radius of the well and the R-matrix boundary. The threshold energies were set to $e_1 = 0$ and $e_2 = 2$. The model parameters have been selected to allow formation of one Feshbach resonance below the second threshold. The Feshbach resonance is a pole that emerges from a bound state with respect to channel 2 when a small coupling between channels 1 and 2 is present, i.e. it exists only in the multichannel case. We check our results with the analytically solvable case of the partial wave with $l = 0$ (see Grozdanov and McCarroll [2007]) and compare the analytical and numerical results of the cross section σ in Figure 3.2 (in the top left panel).

We located S-matrix poles for the partial wave with $l = 0$. In Figure 3.1 we see the amplitude of the implicit function $F(E)$ from (2.59) whose zero points are the S-matrix poles. In the top panel, we observe the implicit function for the uncoupled potential ($V_{12} = V_{21} = 0$) on the physical Riemann sheet where one bound state with the energy $E_B = 1.796$ occurs. The resonance poles for the coupled potential (3.1) are on the Riemann sheet U_1 in the bottom panel where the original state with E_B gave birth to the two poles $E_F = 1.832 \pm 0.029$ i in the vicinity of the real axis – we see the Feshbach resonance in the vicinity of the former bound state.

We calculated the cross section σ_{ij} using (2.34) and removed the Feshbach resonance from it using the appropriate residue matrix (2.80). The results for all σ_{ij} are in Appendix A, here we show only the results for σ_{11}.

The removal led to the complete removal of the Feshbach resonance peak as shown in the left column of Figure 3.2, where the upper figure shows the cross section with the pole included and the bottom figure shows the case with the removed pole, respectively.

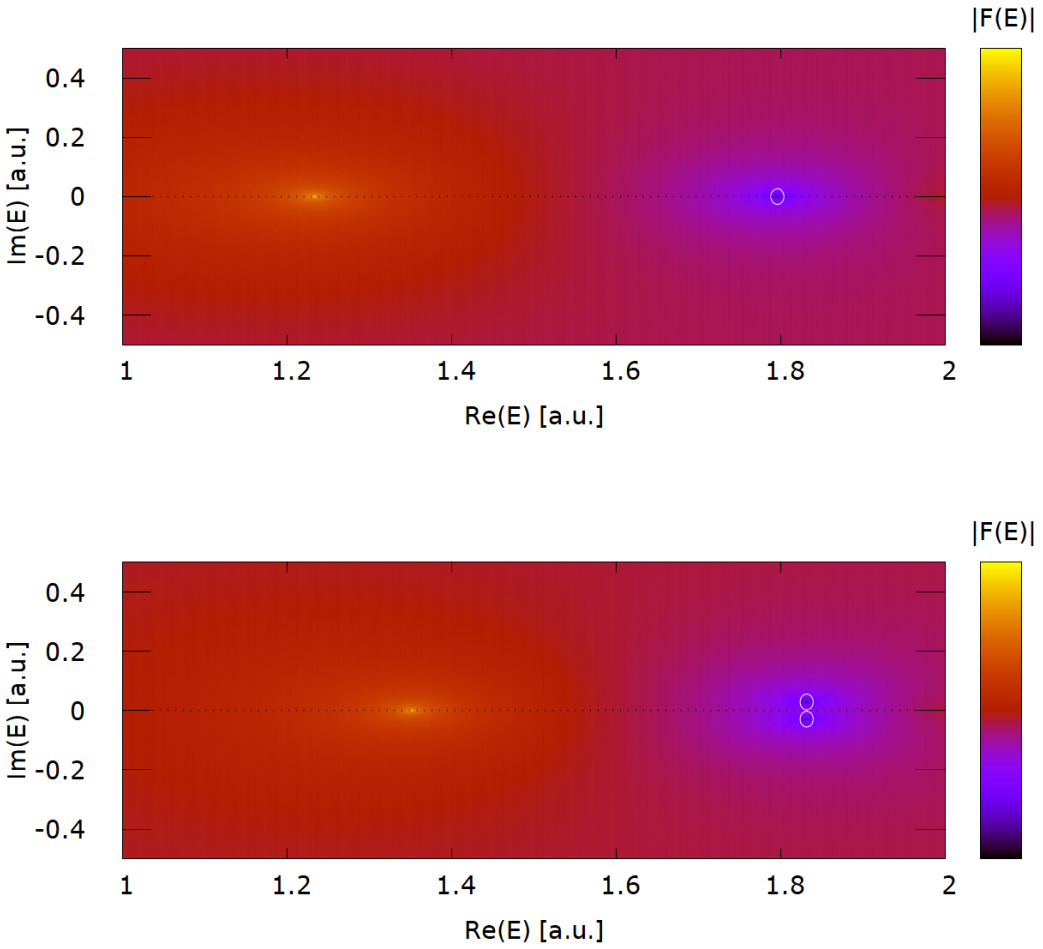

Figure 3.1: Amplitude of the implicit function $|F(E)|$ in the complex plane, minima of the function are circled. Top panel: physical Riemman sheet for the uncoupled case with one bound state. Bottom panel: sheet U_1 for coupled case with Feshbach resonances.

Then we did the same for the nonzero angular momentum $l = 3$, which is no longer analytically solvable. The Feshbach resonance pole occurred at the energy $E_F = 1.775 \pm 0.004\mathrm{i}$ for the potential

$$\begin{aligned} \tilde{U}(r) &= \begin{pmatrix} -34 & -1 \\ -1 & -34 \end{pmatrix}, \quad r \leq a, \\ \tilde{U}(r) &= \begin{pmatrix} 0 & 0 \\ 0 & 0 \end{pmatrix}, \quad r > a. \end{aligned} \tag{3.2}$$

The cross section is plotted in the right column of Figure 3.2 and the bottom right panel shows the case with the Feshbach pole removed.

We see that the resonant peaks vanish after the removal of the pole. However, for $l = 3$, there is still a small visible peak left even after the removal. The source of this peak does not lie in physics but in the numerical error – we simply can not determine the exact position of the pole and so the removal is not perfectly accurate either. It is important to keep in mind that this can happen when we

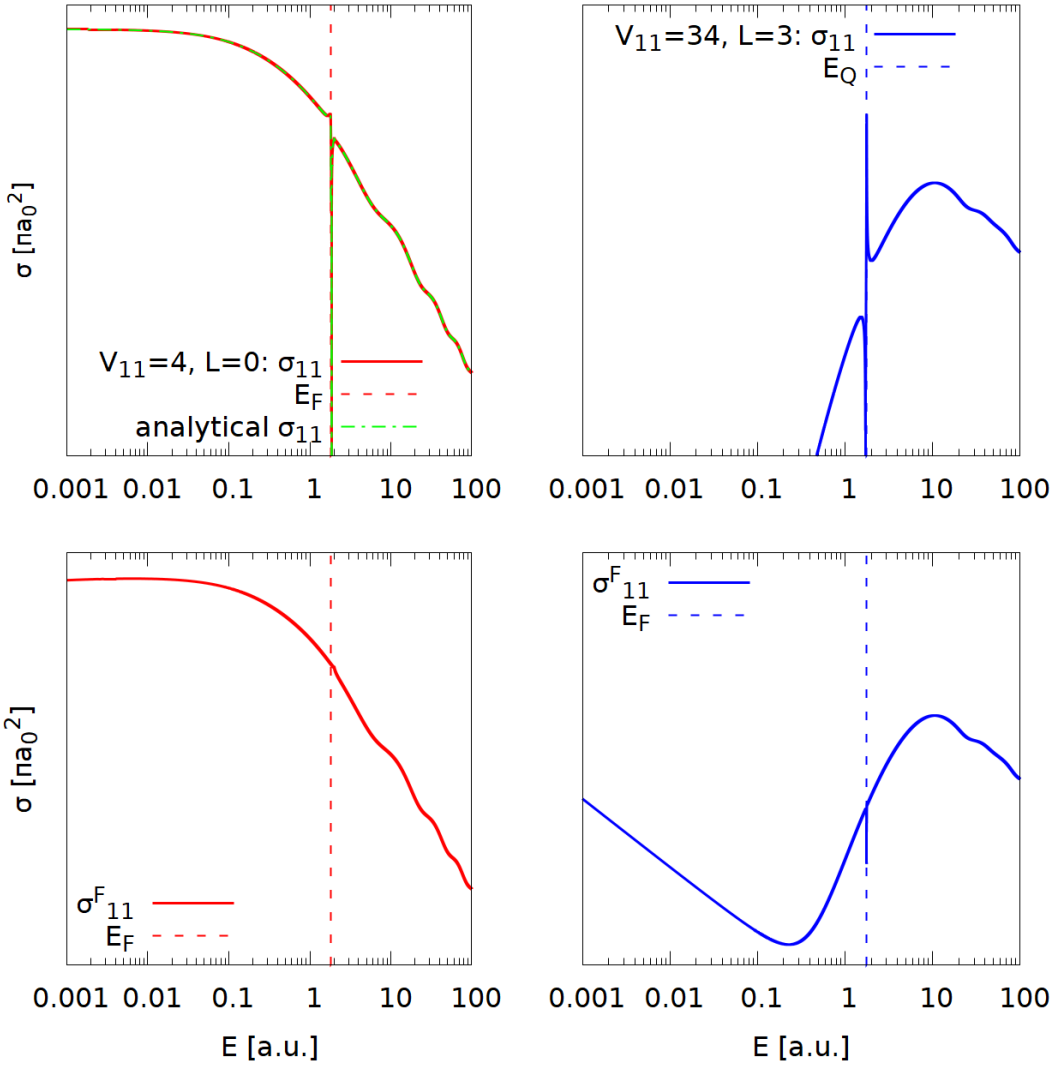

Figure 3.2: The cross section $\sigma_{1\to1}$ as a function of energy on logarithmic scale. For $l = 0$ and the potential (3.1) in the left column; for $l = 3$ and (3.2) in the right column. The upper row shows the original cross section; the bottom row shows the cross section after the removal of the Feshbach resonance.

remove the poles.

In this part, we successfully tested that our numerical results (pole positions and the cross section with the pole included) correspond to the results in Grozdanov and McCarroll [2007] and that we can remove strong resonant peaks completely.

3.2 Spherical well and dipole potential: one-channel case

In this section, we describe a model potential that was analytically solved in Estrada and Domcke [1984] in one channel for the s-wave ($l = 0$) expressed by the relation

$$\tilde{U} = \begin{cases} -U_0 \ , & r \leq a \\ -\gamma r^{-2} \ , & r > a, \end{cases} \tag{3.3}$$

which combines a spherical well of the depth U_0 and a long-range dipole potential parameterized by γ. The radius of the well a equals the R-matrix boundary. At first, we solve the problem in one channel and then we present a method solving the multichannel form of (3.3).

3.2.1 Pure dipole potential in one channel

If we solve a one-channel quantum scattering problem for a pure dipole potential

$$\tilde{U} = -\gamma r^{-2}, r \geq a, \tag{3.4}$$

we express the radial Schrödinger equation for the angular momentum l and dipole parameter γ by

$$\left[\frac{\mathrm{d}^2}{\mathrm{d}r^2} + p^2\right] u_l(r) - \left[\frac{l(l+1) - \gamma}{r^2}\right] u(r) = 0. \tag{3.5}$$

We want to rewrite this equation in the form of

$$\left[\frac{\mathrm{d}^2}{\mathrm{d}r^2} + p^2\right] u_l(r) - \left[\frac{\lambda(\lambda+1)}{r^2}\right] u(r) = 0. \tag{3.6}$$

The coefficient λ is a solution of the quadratic equation

$$\lambda(\lambda+1) = l(l+1) - \gamma, \tag{3.7}$$

and we choose the solution

$$\lambda = \frac{1}{2}\left[-1 + \sqrt{\frac{1}{4} + l(l+1) - \gamma}\right]. \tag{3.8}$$

These coefficients are generally complex numbers.

The analytical asymptotic solutions of (3.6) are the Riccati-Hankel function $\hat{h}_\lambda^{(\pm)}$ with the complex order λ. In the code, we evaluate these functions by subroutine `riccati_hankel_plus_rieman`. The method for the evaluation of $\hat{h}_\lambda^{(\pm)}$ by series expansion is described in Appendix B and it was used in Ragesh Kumar et al. [2022a].

Critical dipole

In the case of a pure dipole potential, bound states can emerge only for $\gamma > \frac{1}{4}$ as shown in Connolly and Griffiths [2007]. This value $\gamma_{crit} = 0.25$ is called the critical dipole. The article Estrada and Domcke [1984] explains that the properties of the model with (3.3) are different for γ below and above the critical dipole.

Also, the results of the calculation of the S-matrix and Siegert states become slightly different. For the simplest case of s-wave ($l = 0$) in one channel, the coefficient λ from (3.8) is real for $\gamma \leq \gamma_{crit}$ and becomes generally complex for $\gamma > \gamma_{crit}$.

S-matrix and propagation of R-matrix

Normally, for calculating the S-matrix in a long-range potential, we would have to use a very large R-matrix boundary to ensure that the potential is small enough in the external region. However, in this case, we can use a simple solution to the problem used in Ragesh Kumar et al. [2022b] where a can be used as the grid boundary.

We call this method the propagation of the R-matrix to a given point $r_0 \gg a$. At first, we calculate the S-matrix $\tilde{S}(E)$ from the solution $\tilde{u}$ represented by

$$\tilde{u}(r) = h_\lambda^{(-)}(pr) - h_\lambda^{(+)}(pr)\tilde{S}, \tag{3.9}$$

using the R-matrix approach for the R-matrix boundary at a. Then we calculate the solution at r_0 and obtain the R-matrix R_{r_0} from the equation

$$\tilde{u}(r_0) = R_{r_0} \left.\frac{\mathrm{d}\tilde{u}(r)}{\mathrm{d}r}\right|_{r=r_0}, \tag{3.10}$$

which is the result of the R-matrix approach propagated to the boundary r_0. Then we use R_{r_0} in the R-matrix condition

$$u(r_0) = R_{r_0} \left.\frac{\mathrm{d}u(r)}{\mathrm{d}r}\right|_{r=r_0}, \tag{3.11}$$

with the wave function expressed in terms of $\hat{h}_l^{(\pm)}$ with the integer order l

$$u(r) = h_l^{(-)}(pr) - h_l^{(+)}(pr)S, \tag{3.12}$$

and evaluate the S-matrix S from it.

Localization of Siegert states

The problem is simpler when we are interested only in the positions of the Siegert states. It is sufficient to compute the minima of the following implicit function

$$F(E) = \left|h_\lambda^{(+)}(pr) - R(E)h_\lambda^{(+)}(pr)\right|, \tag{3.13}$$

as shown in Ragesh Kumar et al. [2022b].

3.2.2 Numerical results in one channel

This problem was analytically solved in Estrada and Domcke [1984] using the Jost functions approach. It is shown there that there are no virtual states in the complex plane for non-zero γ and no resonances in the lower part of the complex plane that become bound states as a function of increasing U_0 for a fixed γ. We use our approach to confirm this behaviour and show the trajectories of the poles in the complex plane in Figure 3.3. In this case, the bound state emerges at $U_0 = 21.927$ for $\gamma = 0.12$ (we used this value to check the correctness of our results) and, in the case of a pure potential well, it happens for $U_0 = 9 \cdot (0.5\pi)^2 = 22.2066$. In Figure 3.4, the scattering cross section is calculated for a few values of U_0 before and after the bound state emerges. We observe behaviour typical for a resonant or virtual state becoming bound. Nevertheless, there is no pole in the complex plane that would correlate with this behaviour. Instead, the cross section rises to the point of emergence of the bound state and then drops as the bound state moves away from the origin.

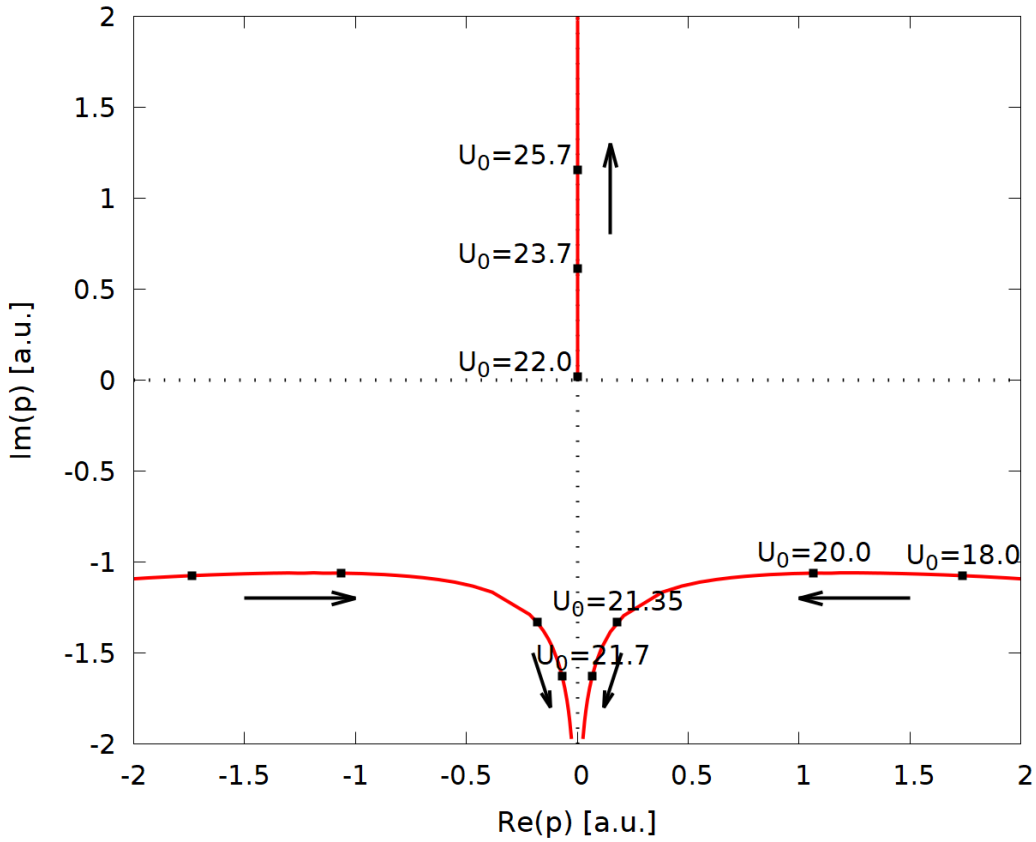

Figure 3.3: Complex plane of the momentum of the particle: trajectories of the S-matrix poles with respect to the depth U_0 of the potential well in the potential (3.3). Parameters of the model: angular momentum $l = 0$, dipole parameter $\gamma = 0.12$

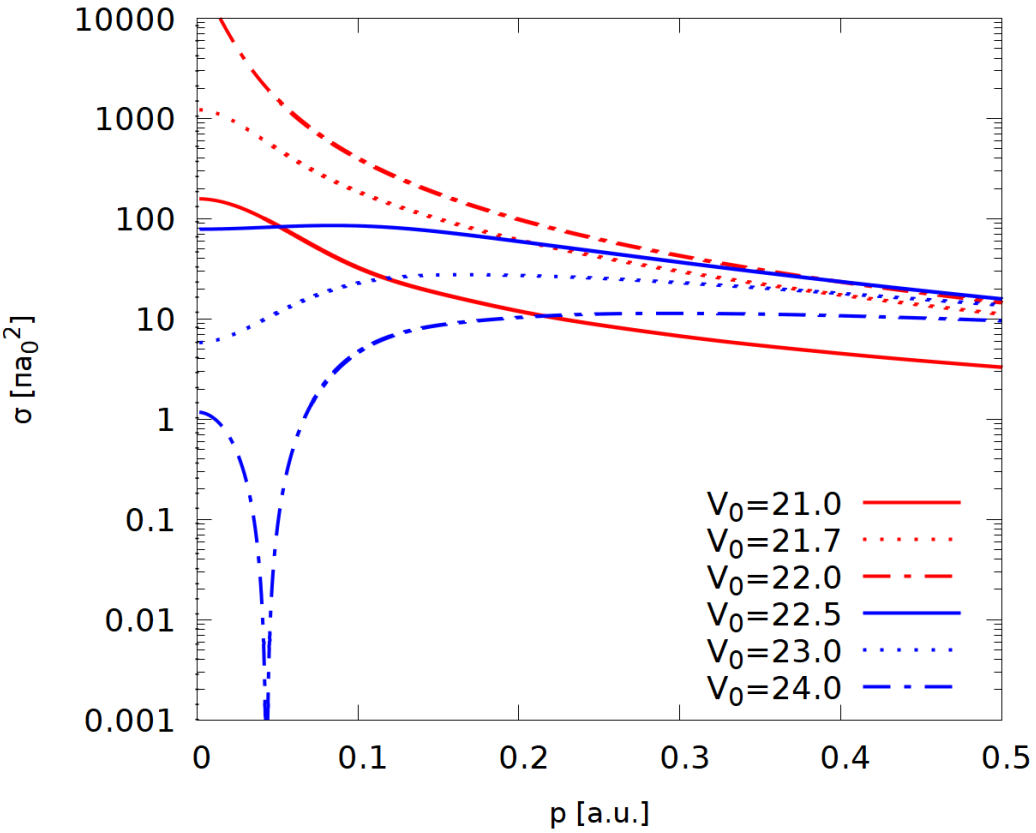

Figure 3.4: Scattering cross section on logarithmic scale as a function of the momentum for selected values of U_0 (bound state emerges at the value $U_0 = 21.9268$). Parameters of the model: angular momentum $l = 0$, dipole parameter $\gamma = 0.12$

3.2.3 Riemann sheets of the second type

In the calculations in Appendix B, we write the complex argument in the polar form $z = |z|e^{i\theta}$. The functions $\hat{h}_\lambda^{(\pm)}(pr)$ are expressed by the formula

$$\hat{h}_\lambda^{(\pm)}(z) = \sqrt{\frac{\pi z}{2}} \frac{J_{-(\lambda+\frac{1}{2})}(z) - e^{\mp \mathrm{i}(\lambda+\frac{1}{2})\pi} J_{(\lambda+\frac{1}{2})}(z)}{\sin[(\lambda+\frac{1}{2})\pi]}, \tag{3.14}$$

where $J_{\pm(\lambda+\frac{1}{2})}(z)$ are the Bessel functions expressed by

$$J_{\pm(\lambda+\frac{1}{2})}(z) = \left(\frac{1}{2}\right)^{\pm(\lambda+\frac{1}{2})} |z|^{\pm(\lambda+\frac{1}{2})} \exp(\pm \mathrm{i}(\lambda+\frac{1}{2})\theta) \sum_{k=0}^{\infty} f_k(z^{2k}). \tag{3.15}$$

In this expansion, the terms $f_k(z^{2k})$ in the sum are functions of the integer powers of z and they are single-valued. However, for a non-integer order λ, the factor $\exp(\pm \mathrm{i}(\lambda+\frac{1}{2})\theta)$ is multi-valued and depends on the choice of the complex phase.

For momenta expressed by $p = |p|e^{\mathrm{i}\phi}$, we define the Riemann sheets of the second type S_n for $n \in \mathbb{Z}$ by

$$S_n \ : \quad \phi \in \left(-\frac{\pi}{2} + 2n\pi; \frac{3\pi}{2} + 2n\pi\right). \tag{3.16}$$

The functions that depend only on integer powers of z are invariant to the choice of the Riemann sheet but, for the potential (3.3) that implies a non-integer order λ of the Riccati-Hankel functions, we obtain different results for different Riemann sheets.

The physical sheet of the complex plane is S_0; the sheets S_{+1} and S_{-1} are the "closest" sheets to the physical one. We already saw that the resonance poles do not reach the origin of the complex plane on the physical sheet for the potential (3.3). Nevertheless, the articles Herzenberg and Saha [1983] and Herzenberg [1984] explain that we can find such poles (reaching the origin) of the S-matrix on the other Riemann sheets of the second type and we reproduce these results in our model.

The results of the pole search on the "closest" sheets $S_{\pm 1}$ in Figure 3.5 confirm the conclusions of Herzenberg and Saha [1983] and Herzenberg [1984]: there are resonances that reach the origin when the bound state emerges on the physical sheet. In other words, the bound-state pole "drops down" from the unphysical Riemann sheet. Thus, we demonstrate that our approach can find the S-matrix poles on the non-physical sheets of the complex plane. Particularly, in Figure 3.5, we see two poles on the sheets $S_{\pm 1}$ reaching the origin – the right half plane of the sheet S_{+1} is equivalent to the left half plane of the sheet S_{-1} (this symmetry holds for all $n \neq 0$).

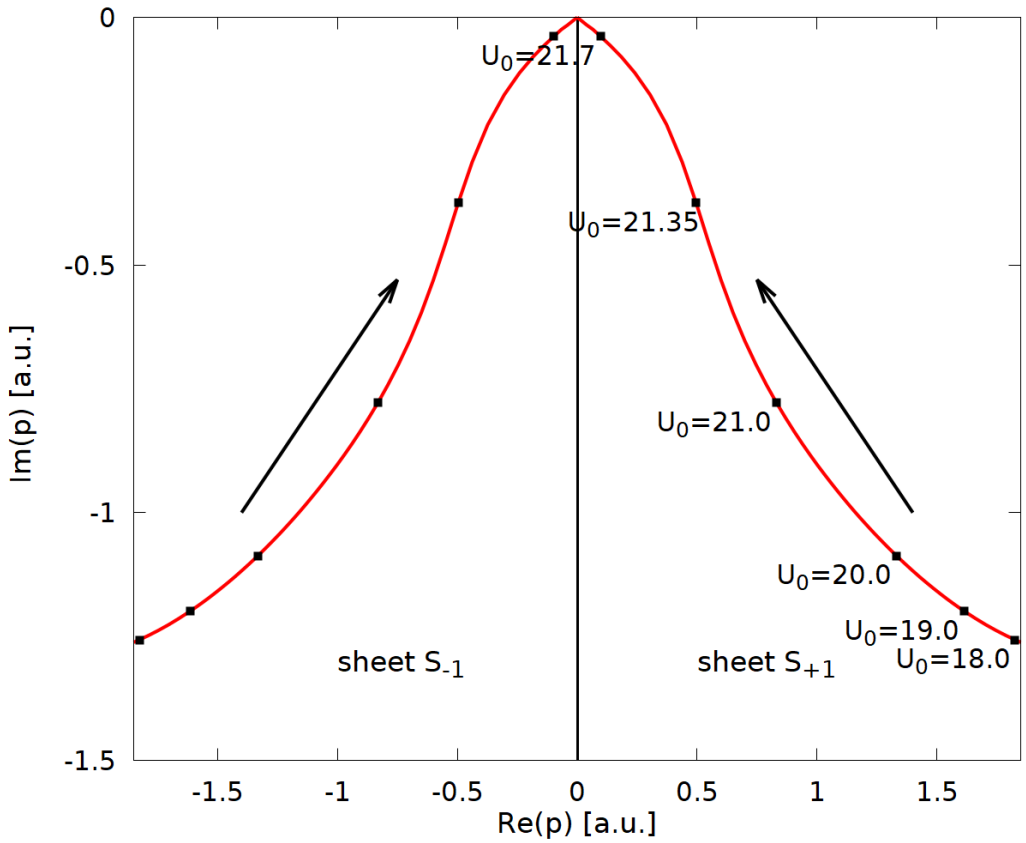

Figure 3.5: Complex plane of momentum: trajectories of the S-matrix poles reaching the origin as a function of the depth U_0 of the well. The left half corresponds to the sheet S_{-1} and the right half to S_{+1}. Parameters of the model: angular momentum $l = 0$, dipole parameter $\gamma = 0.12$.

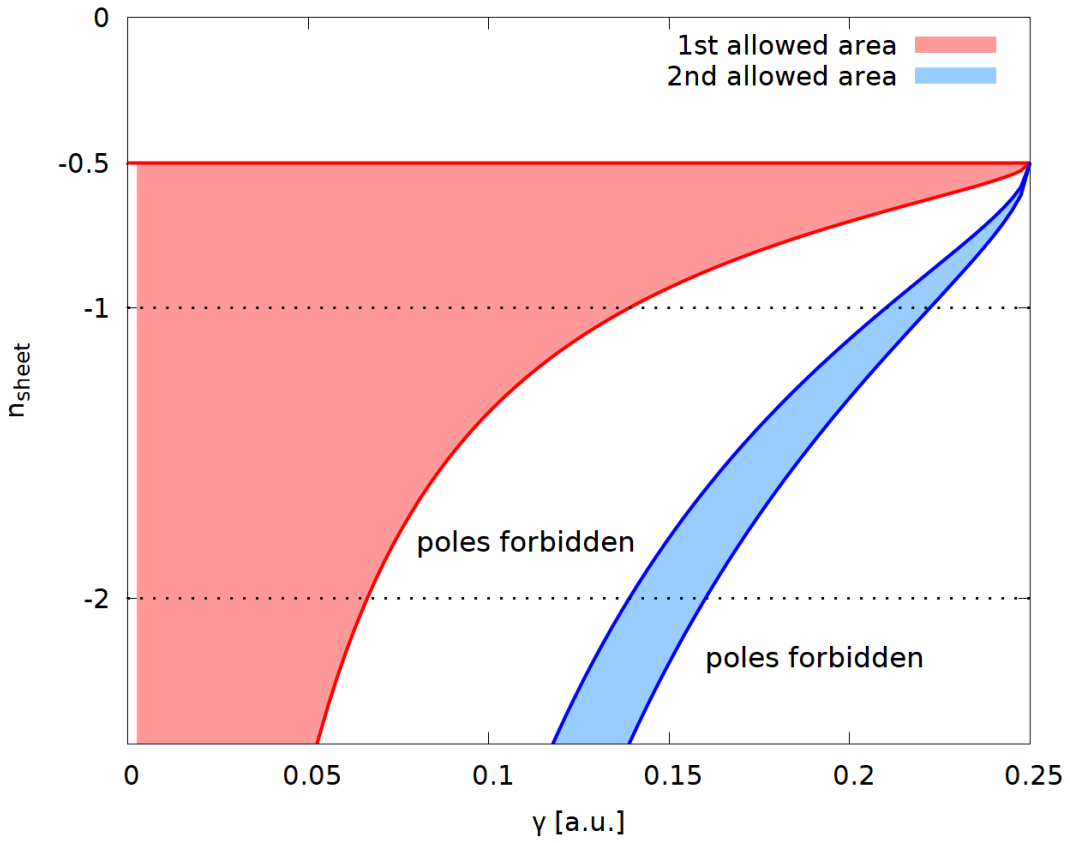

Figure 3.6: The relation between the dipole parameter γ and the index of the Riemann sheet for $l = 0$ showing the areas where the poles can occur in the vicinity of the origin.

A question remains if we can always find a pole on some S_n which is connected with the bound state on S_0. The answer is no. For example, for a larger $\gamma = 0.139$, the poles on $S_{\pm 1}$ will not reach the origin. Although there are two similar poles on the sheets $S_{\pm 2}$ reaching the origin, for even higher γ there are no such poles on any other sheet.

For the case $l = 0$ solved analytically in Herzenberg and Saha [1983] on various Riemann sheets, there is a relation between the occurrence of poles that can reach the origin, the index n of the sheet, and the dipole parameter γ up to γ_{crit}. It was obtained in Herzenberg and Saha [1983] from the boundary condition of the logarithmic derivatives of the wave function $u(r)$ at $r = a$. Expanding the functions into the series in the vicinity of the origin using (3.15) for $\lambda = \sqrt{\frac{1}{4} - \gamma}$ and taking only the lowest powers of the momentum p^λ, they obtained the condition

$$2\sqrt{\frac{1}{4} - \gamma}\left(\arg(p) - \frac{1}{2}\pi\right) = (2n_{sheet} + 1)\pi. \tag{3.17}$$

We show this dependence in Figure 3.6 (only for a negative index n of the sheets but the same relation holds for $n \geq 0$). On the diagram, we see two areas where poles can occur in the vicinity of the origin; anywhere else, this can not happen. Additionally, the diagram shows us that the occurrence of such poles is forbidden for $\gamma > 0.21$ on every possible sheet.

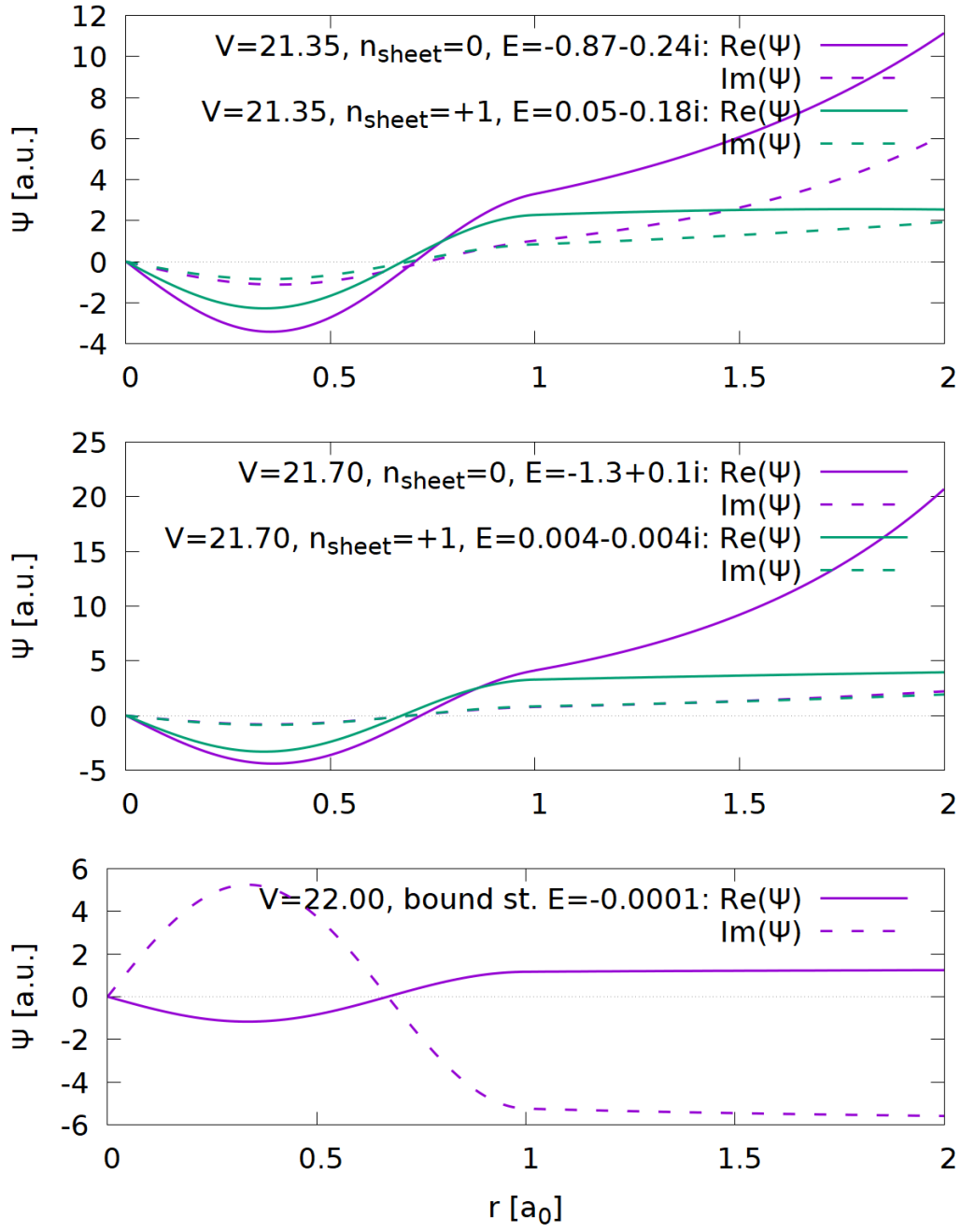

Figure 3.7: Real and imaginary part of the wave function for the energies of the Siegert states shown in Figure 3.3 and 3.5 and for a few key values of the potential parameter U_0. Parameters of the model: angular momentum $l = 0$, dipole parameter $\gamma = 0.12$.

3.2.4 Wave functions

Finally, one could be interested in the properties of the Siegert states on the sheets $S_{\pm 1}$ and look at the relevant wave functions. We applied the R-matrix approach to calculate the wave functions of the Siegert states at selected values of the potential parameter U_0 focusing on the transition between the resonance and the bound state. We compared the wave function of resonances on the physical sheet

S_0 with the one on the non-physical sheet S_{+1} that reaches the origin. The results are depicted in Figure 3.7 for three values of U_0 (for the last one, the bound state emerges).

We see that the wave function of the pole on S_{+1}, that approaches the origin, does not grow fast – it behaves as we would expect. It is also interesting that the shapes of the functions of different Siegert states (the first situated on S_0 and the second on S_{+1}) are similar and they have almost identically positioned zero points.

Notice that the wave function of the bound state is not a real function as we would normally expect. This is a simple consequence of the phase convention for the Riccati-Hankel functions

$$u_{l_i,m_i}(r) \overset{r\to\infty}{\sim} \hat{h}_\lambda^{(+)}(pr) \sim e^{\mathrm{i}(pr-\lambda\frac{\pi}{2})}. \tag{3.18}$$

For a bound state, $p = i|p|$ so the complex phase originates in the term $e^{-\mathrm{i}\lambda\pi/2}$.

3.3 Gaussian and dipole potential: one-channel case

3.3.1 Gaussian well with varying depth

To test our approach on some potentials that can not be solved analytically, we choose a Gaussian potential in the inner region

$$\tilde{U} = \begin{cases} -U_0 e^{-\frac{r^2}{a^2}} , & r \le a \\ -\gamma r^{-2} , & r > a. \end{cases} \tag{3.19}$$

The potential is shown in Figure 3.8.

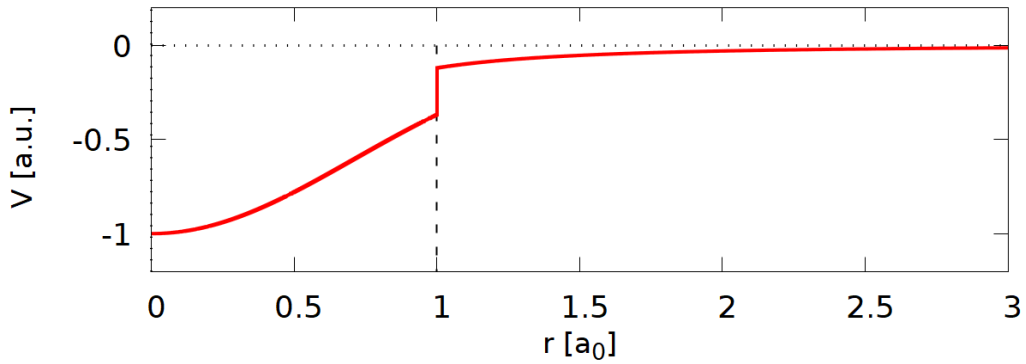

Figure 3.8: The reduced potential $\tilde{U}$ described by (3.19) comprises of a short-range Gaussian term and a long-range dipole term. Potential parameters: $U_0 = 1$, $a = 1$, $\gamma = 0.12$.

We solve this model in the same way as the model with the potential (3.3), i.e. using the calculation of the Hankel functions with the real coefficients λ and the implicit function calculated by (3.13). We identify the potential boundary a with the R-matrix grid boundary.

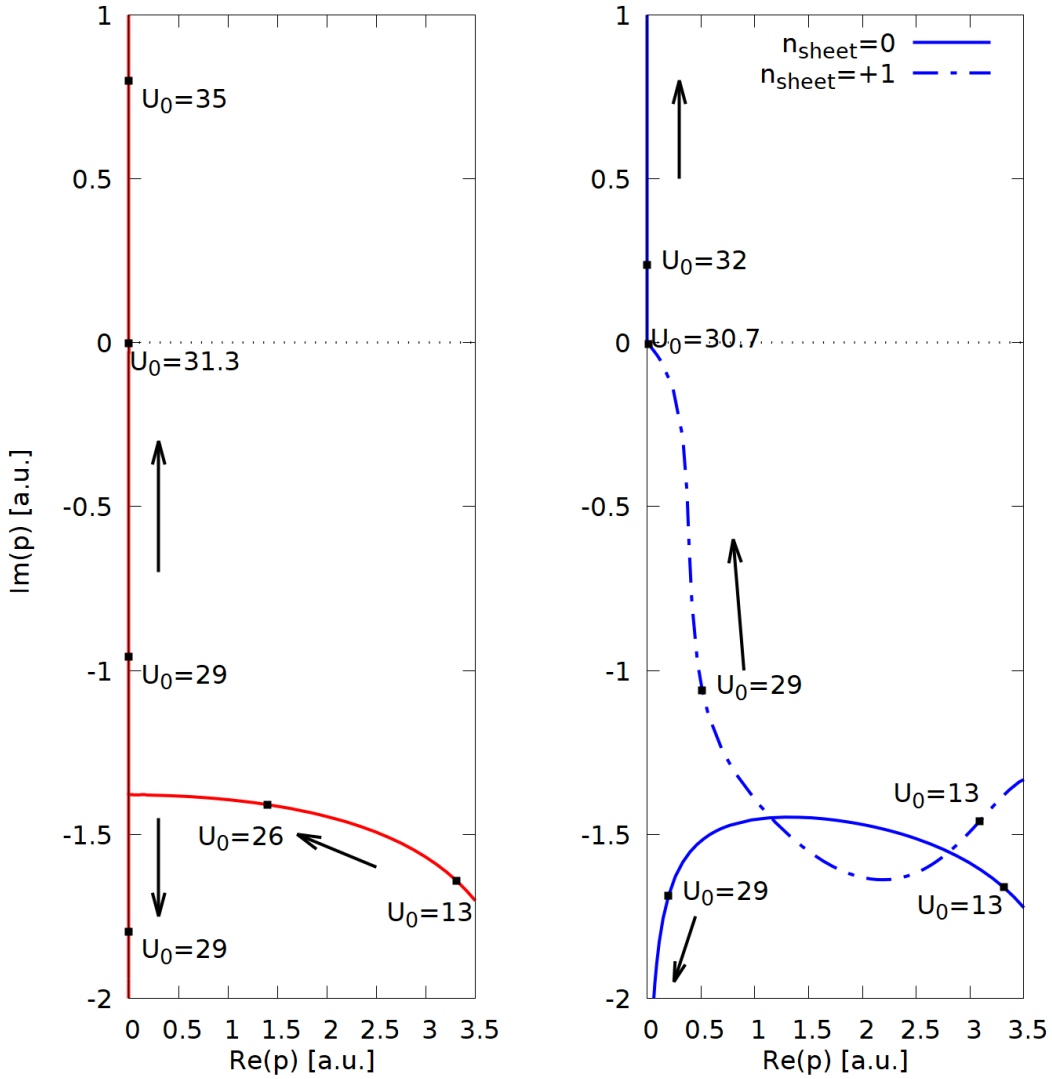

Figure 3.9: Trajectories of the poles of the S-matrix in the complex plane of momentum for the potential (3.19) as functions of the parameter U_0. Left panel: $l = 0$, $\gamma = 0$. Right panel: $l = 0$, $\gamma = 0.12$.

We located the poles of the S-matrix and followed their trajectories on the complex plane as functions of the parameter U_0 for two cases of $\gamma = 0$ and $\gamma = 0.12$. The resulting trajectories of the poles are shown in Figure 3.9. The results are very similar to the case of the rectangular potential well. For $\gamma = 0$, the resonances reach the imaginary axis and give rise to the virtual states (one virtual and one bound state in the end). For $\gamma = 0.12$, we observe the same process as in the preceding section – poles do not reach the origin or lead to a virtual state on the physical sheet S_0; however, it happens on the sheet S_{+1}.

3.3.2 Gaussian well and barrier with varying dipole parameter

The second model works with the potential

$$\tilde{U} = -3e^{-(\frac{r}{4})^2} + e^{-(r-3)^2} - \gamma r^{-2}, \tag{3.20}$$

in one channel and $l = 0$. The function (3.20) is plotted in Figure 3.10. In this case, we set the R-matrix boundary to $a = 5$. Due to the natural barrier in the potential, a strong resonance is formed in this system.

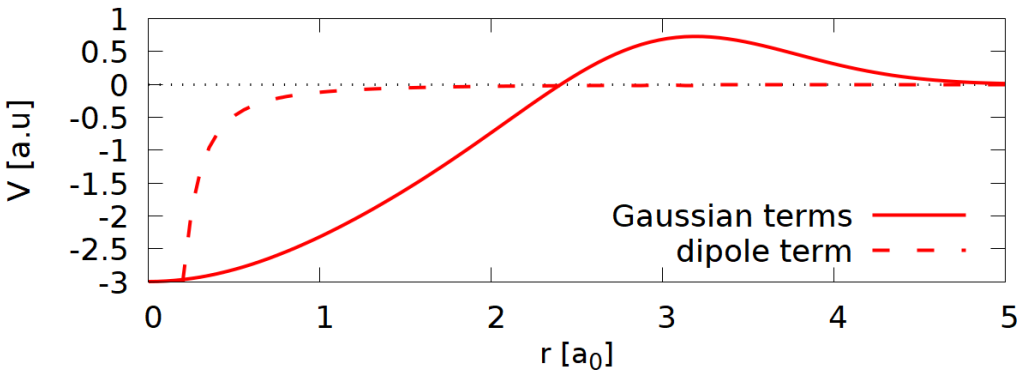

Figure 3.10: The reduced potential $\tilde{U}$ described by the equation (3.20) comprises of a short-range Gaussian term and a long-range dipole term. Potential parameters: $\gamma = 0.12$, $l = 0$.

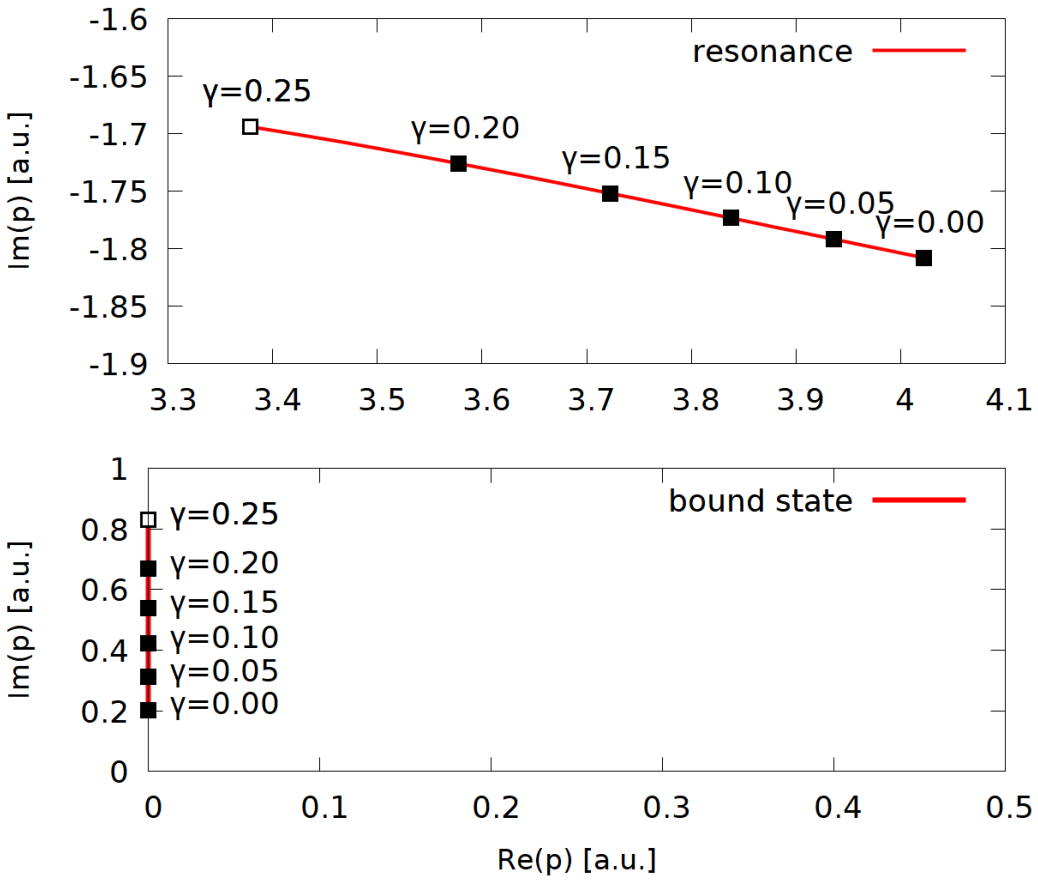

Figure 3.11: Poles of the S-matrix for the potential (3.20). The trajectory of the resonance (top panel) and the bound state (bottom panel) in the complex plane as a function of the parameter $\gamma \in [0, 0.25]$.

In this case, we varied the γ parameter from 0 to the critical dipole 0.25 and observed the change of position of the poles of the S-matrix. For $\gamma = 0$, two Siegert states were found in the vicinity of the origin, one resonance and one bound state. In Figure 3.11, we show their trajectories in the complex plane as functions of γ increasing to the critical dipole value $\gamma_{crit} = 0.25$.

3.4 Spherical well and dipole potential: multi-channel degenerate problem

Dipolar interaction $\frac{\mu \cos\theta}{r^2}$ is non-spherical and couples partial waves with neighboring angular momenta, i.e. l and $l+1$. The one-channel case neglects this coupling but it can be represented in a multichannel problem. In this subsection, we introduce the propagation of the R-matrix and search for the Siegert states in a multichannel case. Then we present results for a two-channel model.

We solve the problem for the potential

$$\tilde{\mathbf{U}} = \begin{cases} -\mathbf{U_0} \ , & r \leq a \\ -\gamma r^{-2} \ , & r > a, \end{cases} \tag{3.21}$$

which is represented by $N \times N$ matrices $\mathbf{U_0}$ and γ.

3.4.1 S-matrix and multichannel propagation of R-matrix

In a multichannel problem, the propagation of the R-matrix used in Section 3.2.1 is more complicated. We can use the approach from Ragesh Kumar et al. [2022b] only in the case of degenerate channels.

The system consists of N degenerate channels, $N_{targ} = 1$ and $N_{chan} = N$. We set $e_1 = 0$ and $p_i = p$ and the set of coupled equations (2.10) becomes

$$\left[\frac{\mathrm{d}^2}{\mathrm{d}r^2} + p^2\right] u_i(r) - \sum_j \left[\frac{l_i(l_i+1)\delta_{ij} - \gamma_{ij}}{r^2}\right] u_j(r) = 0. \tag{3.22}$$

We identify a new matrix with components

$$B_{ij} = l_i(l_i+1)\delta_{ij} - \gamma_{ij}, \tag{3.23}$$

and we rewrite the equation (3.22) by $N \times N$ matrices

$$\left[\left(\frac{\mathrm{d}^2}{\mathrm{d}r^2} + p^2\right)\mathbb{I} - \frac{1}{r^2}\mathbf{B}\right]\mathbf{u} = 0. \tag{3.24}$$

The first term of the equation (3.24) is just the unit matrix multiplied by a scalar. Therefore, a linear transformation $\mathbf{A}$ that will diagonalize the matrix $\mathbf{B}$ will not affect the first term. It can be done only for a degenerate problem (or when the non-degenerate channels are not coupled). This approach can not be used in a general case (nevertheless, there is a possibility to solve the problem using the exterior complex scaling approach).

We diagonalize the matrix $\mathbf{B}$ as

$$\mathbf{B} = \mathbf{A}^{+}\mathbf{diag}(b_1, ..., b_N)\mathbf{A}, \tag{3.25}$$

and obtain the set of N eigenvalues b_i. Analogically to the approach in Section 3.2.1, we calculate the coefficients

$$\lambda_i = \frac{1}{2}\left[-1 + \sqrt{\frac{1}{4} + b_i}\right]. \tag{3.26}$$

Thus, applying the linear transformation $\mathbf{A}$ on $\mathbf{u}$, we obtain the equation

$$\left[\frac{\mathrm{d}^2}{\mathrm{d}r^2} + p^2 - \frac{\lambda_i(\lambda_i+1)}{r^2}\right]\mathbb{I}\tilde{\mathbf{u}}(r) = 0, \tag{3.27}$$

where $\tilde{\mathbf{u}}$ is the wave function in the new channel basis. This formula is a decoupled Schrödinger equation that can be solved using the R-matrix approach and the R-matrix $\tilde{\mathbf{R}} = \mathbf{A}^{+}\mathbf{R}\mathbf{A}$ transformed in the new channel basis giving us the solution

$$\tilde{\mathbf{u}}(r) = \mathbf{h}_{\lambda}^{(-)}(pr) - \mathbf{h}_{\lambda}^{(+)}(pr)\tilde{\mathbf{S}}. \tag{3.28}$$

As a next step, we calculate $\tilde{\mathbf{u}}$ at some point $r_0 \gg a$ and obtain the R-matrix $\tilde{\mathbf{R}}_{r_0}$ from the equation

$$\tilde{\mathbf{u}}(r_0) = \tilde{\mathbf{R}}_{r_0}\left.\frac{\mathrm{d}\tilde{\mathbf{u}}(r)}{\mathrm{d}r}\right|_{r=r_0}, \tag{3.29}$$

which is the result of the multichannel R-matrix approach propagated to the boundary r_0. We calculate the non-transformed R-matrix at r_0 as $\mathbf{R}_{r_0} = \mathbf{A}\tilde{\mathbf{R}}_{r_0}\mathbf{A}^{+}$ which leads to the equation for wave functions in the original basis

$$\mathbf{u}(r_0) = \mathbf{R}_{r_0}\left.\frac{\mathrm{d}\mathbf{u}(r_0)}{\mathrm{d}r}\right|_{r=r_0}, \tag{3.30}$$

and allows us to solve for the S-matrix as usual.

3.4.2 Localization of Siegert states

According to Ragesh Kumar et al. [2022b], for finding the Siegert states, it is sufficient to locate the minima of the following implicit function

$$F(E) = |\det\left[\mathbf{M}(E)\right]| = \left|\det\left[\mathbf{h}_{\lambda}^{(+)}(pr) - \mathbf{A}^{+}\mathbf{R}(E)\mathbf{A}\mathbf{h}_{\lambda}^{(+)}(pr)\right]\right|. \tag{3.31}$$

3.4.3 Two-channel approximation for dipolar interaction

To illustrate that similar behaviour occurs in more channels, we add one more example for two channels. We use the following parameters of the potential:

$$\gamma = \begin{pmatrix} 0.12 & 0.03 \\ 0.03 & 0.12 \end{pmatrix}, \quad l = \begin{pmatrix} 0 \\ 1 \end{pmatrix}, \quad U_0 = \begin{pmatrix} U_{11} & 1 \\ 1 & U_{11}+2 \end{pmatrix}. \tag{3.32}$$

The choice of different angular momenta models properties of the actual dipolar interaction which couples angular momenta of opposite parity. We look for trajectories of Siegert states in the complex plane for U_{11} varying in the interval $(15, 25)$. Let's remind the reader that the channels are degenerate, i.e. $e_1 = e_2 = 0$.

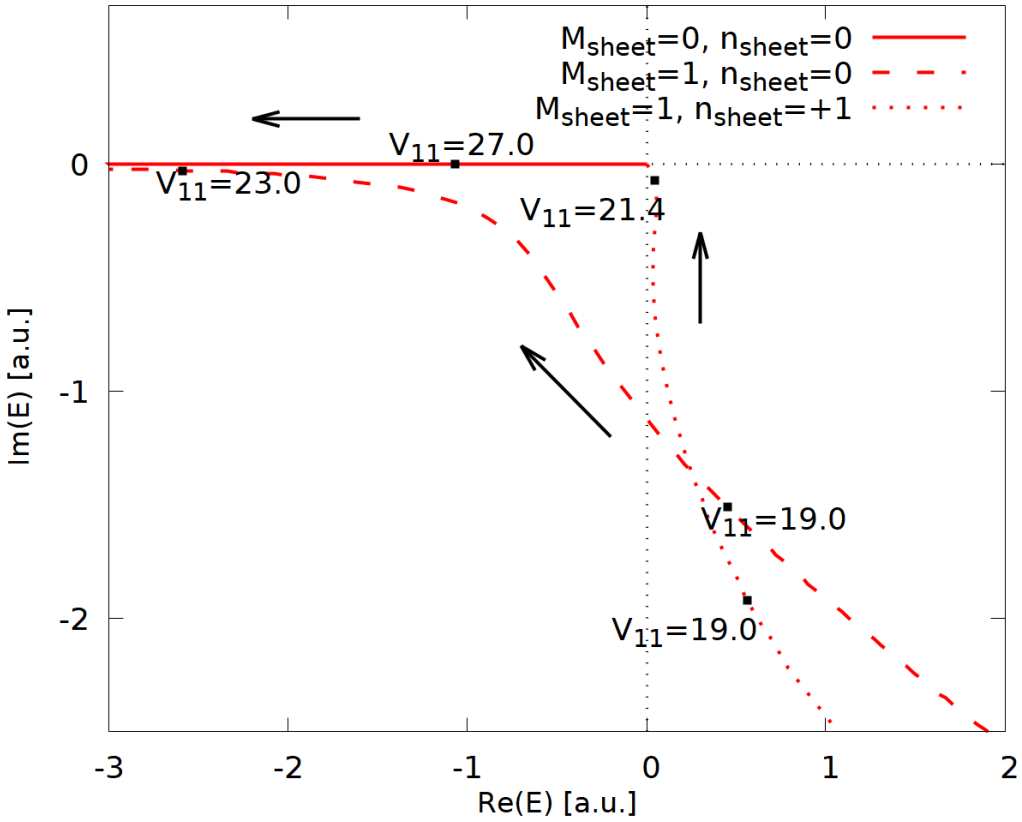

Figure 3.12: Complex plane of energy: trajectories of the S-matrix poles for the potential (3.32) on different sheets of the plane. The selected Riemann sheets are indicated in the legend: number M_{sheet} denotes the first type and n_{sheet} denotes the second type.

This time, we finally have to use the approach leading to the formula (3.31) in the matrix form. We choose weak coupling components of the dipolar potential and reach similar results as above and observe consistency between the models.

The movement of the poles is shown in Figure 3.12. In the multichannel case, we have to stay in the complex plane of energies, the sheets of the plane are denoted in the legend. We see that the trajectories of the poles are qualitatively the same as in the one-channel case. For $n_{sheet} = 0$, there is a resonance that does not reach the origin. However, there is a resonance for $n_{sheet} = +1$, which reaches the origin when the corresponding bound state emerges.

3.5 Coulomb potential

As the last test of our method, we used the pure Coulomb potential in one channel

$$\tilde{U}(r) = 0\ , \quad Z = 1\ , \quad \eta = \frac{-1}{p}. \tag{3.33}$$

We solve the problem with a charged target which means that the external solution (2.21) is now expressed in terms of so-called Coulomb-Hankel functions $H_l^{(\pm)}(\eta, pr)$. These functions and the Fortran subroutine COULCC that generates them are described in Thompson and Barnett [1985]. We use this simple case mainly to test the usage of the Coulomb-Hankel functions before the application to complex problems.

At first, we test if our approach gives us the correct locations of bound states of the pure Coulomb potential. In Figure 3.13, we plot the physical sheet of the complex plane of the energies for $l = 1$ and $l = 3$ where the bound states lie on the negative real axis. We see that our approach gives the predicted results: the bound states with energies $E = -\frac{1}{2n^2}$. We also show that, for higher l, the bound states with $n \leq l$ disappear.

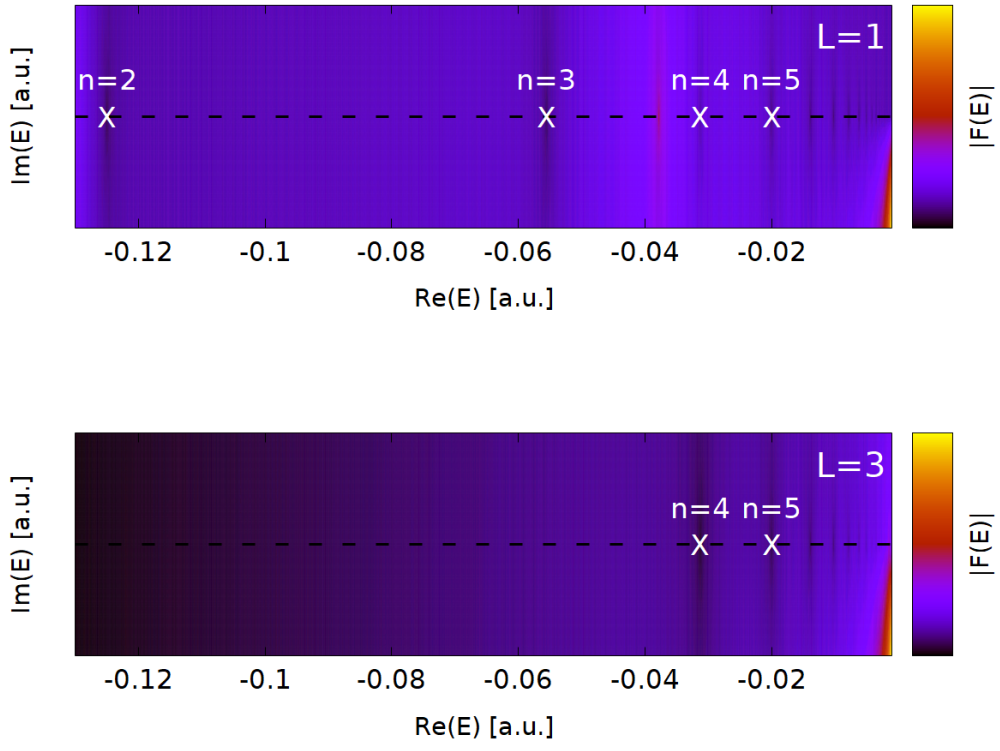

Figure 3.13: Bound states of the pure Coulomb potential for $l = 1$ (top panel) and $l = 3$ (bottom panel) on the physical sheet of the complex plane of energies. Bound states for the lowest n are highlighted.

The next step is testing the accuracy of the bound state energy. We chose the state with $n = 3$, $l = 1$, i.e., we look for the pole at $E = -\frac{1}{18} = -0.0\bar{5}$. The results are in Table 3.1.

Table 3.1: The energy of bound state of the pure Coulomb potential with $n = 3$ and $l = 1$. The comparison of the reference value of the bound state energy and our numerical result, including the absolute error Δ_E and the relative error η_E. R-matrix grid parameters: number of B-splines $M = 103$, order of B-splines $k = 5$, grid boundary $a = 5$.

E_{ref} $[a.u.]$	$-0.0\bar{5}$
E_{num} $[a.u.]$	-0.055555567
Δ_E $[a.u.]$	10^{-8}
η_E	$2 \cdot 10^{-7}$

In the same way as for the bound states, we test the locations of resonances for the Coulombic potential and the spherical potential well of the depth U_0

$$U(r) = \frac{-2Z}{r} + \tilde{U}(r) \ , \quad \tilde{U}(r) = \begin{cases} -U_0 \ , & r \leq a \\ 0 \ , & r > a. \end{cases} \tag{3.34}$$

We show how resonances of the potential well of the depth $U_0 = 20$ move over the complex plane when we vary the parameter Z from -1 to 1. The case $Z = 0$ is a solved problem of the pure potential well. The trajectory of the resonance is shown in Figure 3.14. We see that the pole moves continuously over the plane which is the first test of correctness.

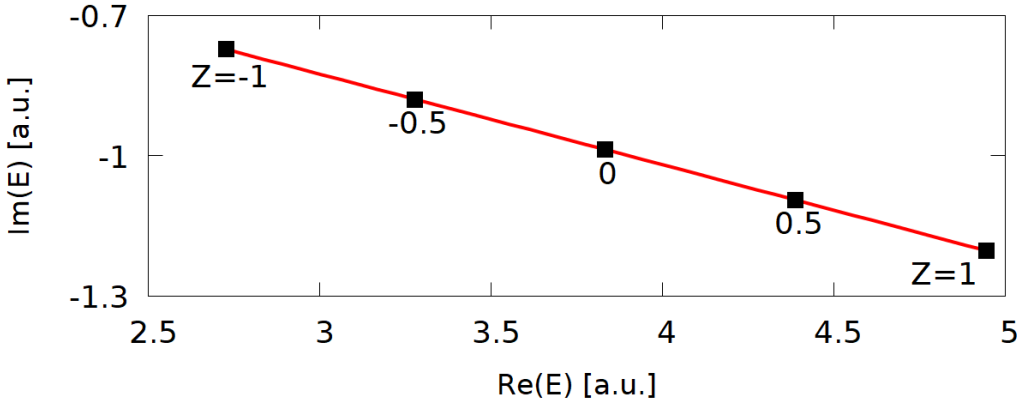

Figure 3.14: Trajectory of resonance in the potential well with respect to the parameter Z of the additional Coulomb interaction in the range from -1 to 1. Parameters: potential depth $U_0 = 20$, angular momentum $l = 3$.

Similarly as Konvalinka [2021], we test our results analytically in Mathematica where the Coulomb-Hankel functions $H_l^{(\pm)}$ (and Coulomb wave functions $F_l^{(\pm)}$ and $G_l^{(\pm)}$) are implemented. Thus, we find the poles of the S-matrix by applying the function FindRoot to the function

$$F(p) = \frac{\mathrm{d}F_l(\eta, \tilde{p}r)}{\mathrm{d}r}\bigg|_{r=r_0} H_l^{(+)}(\eta, pr) - \frac{\mathrm{d}H_l^{(+)}(\eta, pr)}{\mathrm{d}r}\bigg|_{r=r_0} F_l(\eta, \tilde{p}r) \ , \tag{3.35}$$

where U_0 is the depth of the well, $\eta = Z/p$, $\tilde{p} = \sqrt{U_0 + p^2}$, and r_0 the boundary of the R-matrix grid. The comparison of the analytically and numerically obtained energies is in Table 3.2.

Table 3.2: Energies E_a of resonances for various strengths of the Coulomb interaction obtained by our code in Mathematica and their differences compared to the numerical values. Parameters: potential depth $U_0 = 20$, angular momentum $l = 3$.

Z	E_a $[a.u.]$	Δ_E $[a.u.]$
0	$3.83222 - 0.98632\ \imath$	$7 \cdot 10^{-5}$
-1	$2.72645 - 0.77241\ \imath$	$8 \cdot 10^{-5}$
1	$4.94456 - 1.20234\ \imath$	$1 \cdot 10^{-4}$

The last test was a plot of the implicit function close to the real axis because, in the preceding applications of the COULCC subroutine, some non-physical poles occurred there. We tested our numerical model for this behaviour and did not find any such poles. In Figure 3.15, there is an example of a resonance close to the real axis with no other poles around.

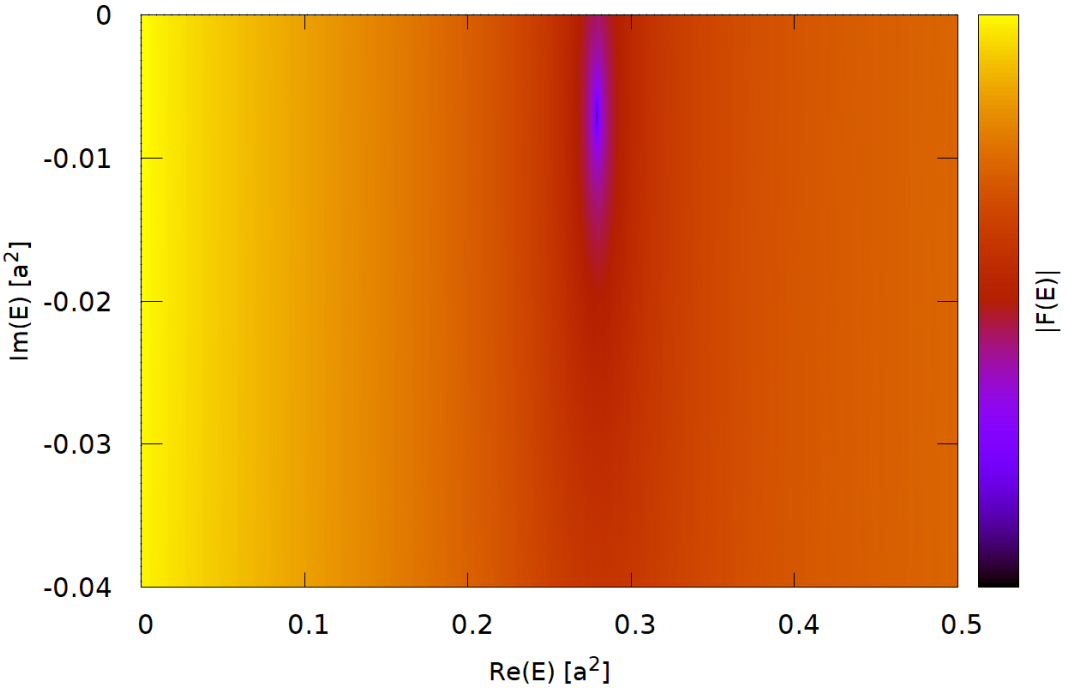

Figure 3.15: An implicit function for the case of a potential well and Coulomb potential close to the real axis of energy. Position of the resonance: $E = 0.279 - 0.007$i. Parameters: Coulomb potential parameter $Z = -1$ potential depth $U_0 = 29$, angular momentum $l = 3$.

4. Siegert states in molecules

After solving the model potentials in the previous chapter we move to real quantum systems. My numerical R-matrix approach is replaced by a complex R-matrix approach solving the electron scattering from molecules. This numerical method is implemented in UKRmol+ Fortran codes described in Mašín et al. [2020]. The code has been used for example by Ragesh Kumar et al. [2022a] to study Siegert states in electronically elastic collisions. The Siegert module was not applicable to inelastic models and the collisions with ions, relevant also for photoionization. The goal of my work was to lift these limitations.

4.1 Implementation into the UKRmol+ codes

The numerical approach in UKRmol+ is much more complicated than the R-matrix method I implemented; the whole problem is multi-electron. Nevertheless, the calculation of the Siegert states does not have to deal with this complexity. This is because the Siegert state calculation is a one-electron problem constrained to the R-matrix outer region which only requires the boundary amplitudes and channel definitions. Therefore, we use the formulas (2.58) for the S-matrix and (2.59) for the implicit function in the same way as we did in our model multichannel calculations. The only remaining task was to translate my implementation into the UKRmol+ codes.

To do that, I made changes in the files `siegert.f90` and `siegert_mod.f90` in the part UKRmol-out focused on the external region. In these files, the approach to find the poles of the S-matrix was already implemented; nevertheless, it had been done only for the completely degenerate case of elastic scattering with $e_i = e$. I improved the code to solve a general inelastic problem and checked the implementation with the results of the two-channel potential solved by my stand-alone code as described in Section 3.1. In the same way, I rewrote the implementation of the S-matrix evaluation for inelastic scattering. The UKRmol+ codes calculate the T-matrix but only on the real axis. The T-matrix is trivially related to the S-matrix: $\mathbf{T} = \mathbf{S} - \mathbb{I}$.

Then I implemented the evaluation of the residue of poles of the S-matrix and implemented output of T-matrices with and without a pole removed. Again, the results were tested on the problem solved in Section 3.1. The Siegert code is launched by calling `outer-run siegert` and outputs the poles of the S-matrix and secondly the T-matrices on a chosen energy grid. Then the standard UKRmol-out program `ixsecs` uses the T-matrices to evaluate the electron scattering cross section. I used the UKRmol+ code in the same spirit as in the previous chapter but for the real systems. The necessary input data (R-matrix amplitudes and channel data) were provided by my supervisor.

4.2 CO_2 in Hartree-Fock approximation

We test the method implemented to the UKRmol+ codes on the R-matrix results for the $CO_2{}^+$ ion calculated by Hartree-Fock approximation (CO_2 HF in what

follows) of the following channel properties:

- Number of target channels: $N_{targ} = 1$,
- Maximal angular momentum: $l_{max} = 7$.

We worked with results of the Hartree Fock (or Static Exchange) model described in Mašín et al. [2018] for the four lowest-lying states of the ion, including its ground state. The electron energies are measured with respect to the threshold of each other. The calculated HF energies of each state are:

- X ($^2\Pi_g$) state (the ground state): $e_X = -187.16$ *a.u.*,
- A ($^2\Pi_u$) state: $e_A = -186.99$ *a.u.*,
- B ($^2\Sigma_u^+$) state: $e_B = -186.97$ *a.u.*,
- C ($^2\Sigma_g^+$) state: $e_C = -186.91$ *a.u.*.

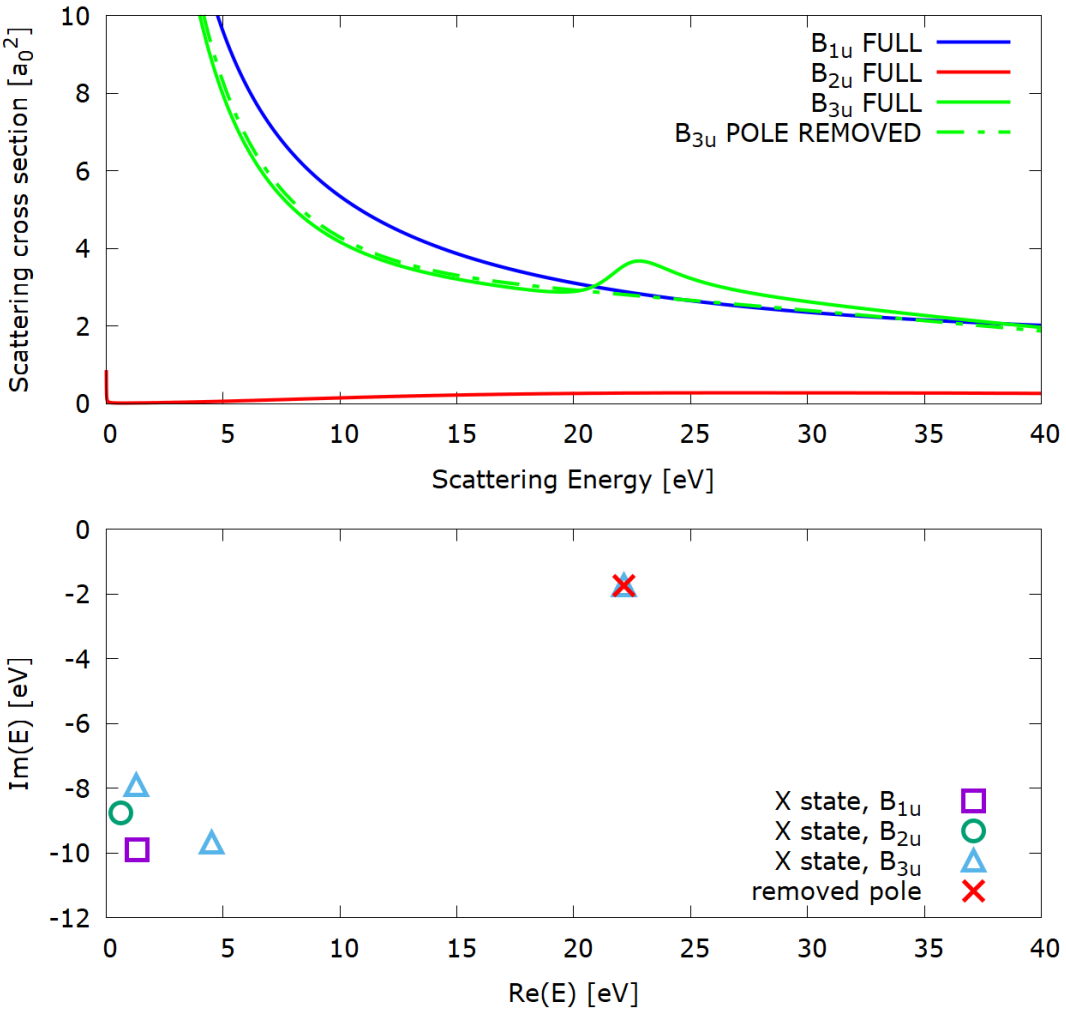

Figure 4.1: The results for the X state of CO_2^+. Upper panel: electron scattering cross section, for B_{3u} with pole removed. Bottom panel: the poles of the S-matrix, the removed pole from the B_{3u} irreducible representation is highlighted.

Due to later applications to photoionization, we have restricted ourselves to the three irreducible representations of the total wave function B_{1u}, B_{2u} a B_{3u}. Only these three irreducible representations are accessed by dipole transition from the totally symmetric neutral ground state of the molecules. We had one set of R-matrix outputs for each ionic state and each total symmetry.

We scanned the complex plane for all the states and symmetries and evaluated the cross sections for the electron scattering on the ion. We show the results for X state and C state where we found strong resonant peaks as shown in Figure 4.1 and 4.2, respectively. The scan of the complex plane is in the bottom panel and the scattering cross section with the removed peaks is in the top panel of each figure. We see that our method is indeed able to perfectly remove the resonant contribution from the results.

The selected resonant poles in states A and B do not lead to any visible peaks in the electron scattering due to the growth of the background scattering cross section for low energies. However, the removal of the poles in Figure 4.3 and 4.4 is still visible (the small sharp peaks in the cross section are there probably due to a numerical cancellation error).

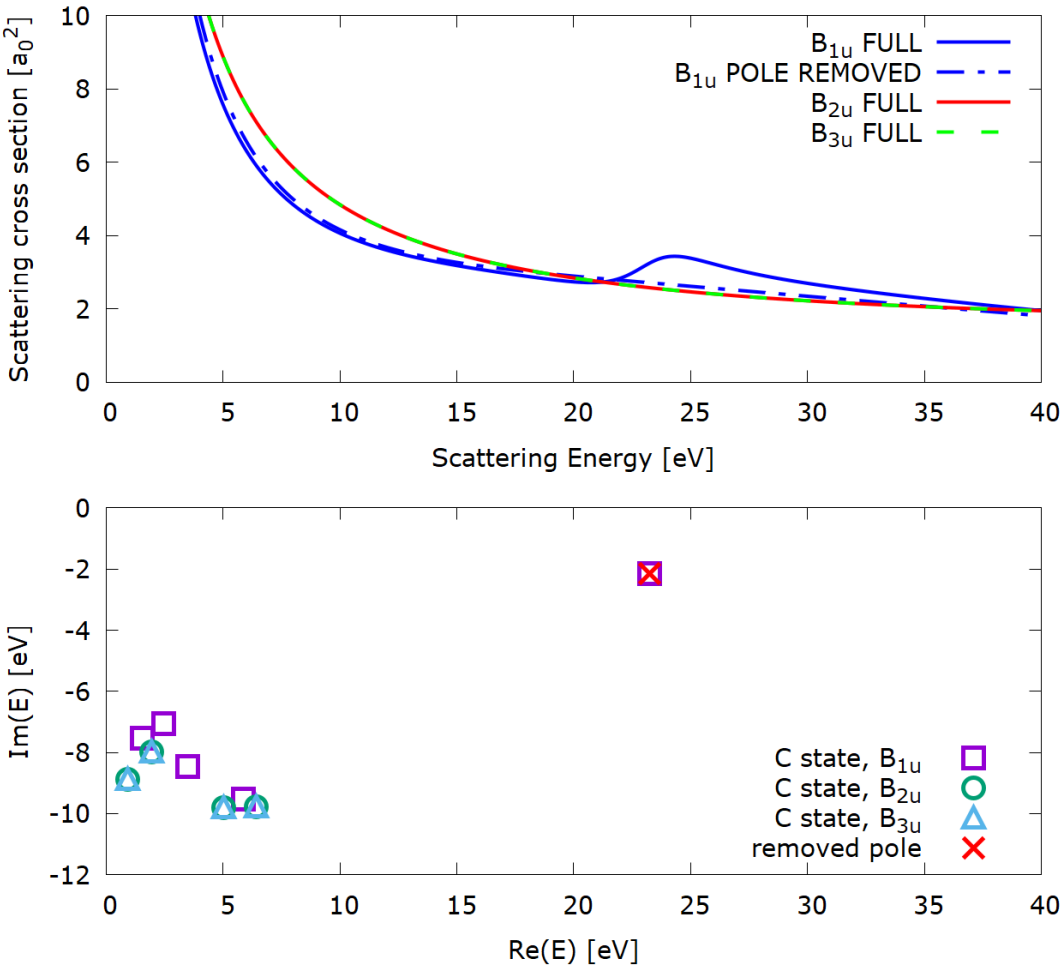

Figure 4.2: The results for the C state of CO_2^+. Top panel: electron scattering cross section, for B_{1u} with pole removed. Bottom panel: the poles of the S-matrix, the removed pole from the B_{1u} irreducible representation is highlighted.

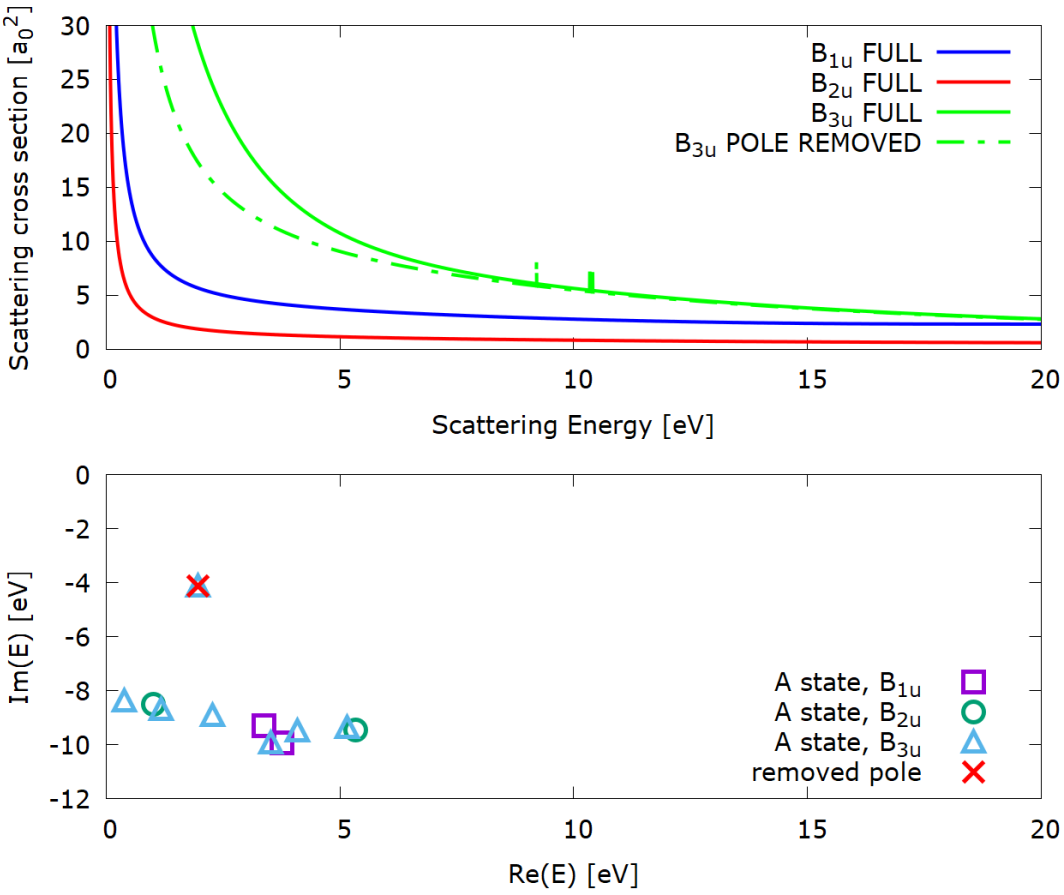

Figure 4.3: The results for the A state of CO_2^+. Upper panel: electron scattering cross section, for B_{3u} with pole removed. Bottom panel: the poles of the S-matrix, the removed pole from the B_{3u} irreducible representation is highlighted.

4.2.1 Comparison with the photoionization cross section

To see how the same resonances manifest in photoionization, we studied the photoionization cross section of CO_2 from Mašín et al. [2018]. The results are in Figure 4.5. Briefly, the molecular-frame photoionization cross section for photon polarization q is given in Harvey et al. [2014] by

$$\left(\frac{\mathrm{d}\sigma}{\mathrm{d}\Omega}\right) = 4\pi^2 \alpha a_0^2 \omega \left| \left\langle \psi^{(-)}_{\vec{k}_f} | \hat{d}_q | \psi_0 \right\rangle \right|^2 , \tag{4.1}$$

where ψ_0 is the wave function of a bound state, $\psi^{(-)}_{\vec{k}_f}$ is a final continuum state, and $\hat{d}_q$ is the dipole operator

$$\hat{d}_q = \sqrt{\frac{4\pi}{3}} r X_{1q}(\vec{r}), \tag{4.2}$$

where X_{1q} is a real spherical harmonic. The cross sections in Figure 4.5 are calculated for a randomly oriented sample of molecules from so-called partial-wave dipole matrix elements which can be calculated from solutions of the type (2.29). A detailed description of molecular photoionization is beyond the scope of this work.

In Figure 4.5, we plot the positions of the selected poles found in the previous Section to connect them with the peaks of the photoionization cross section. The highest peak is observed in C state; however, for each state, we found a peak potentially connected with one of the poles. Note that, in Figure 4.5, the horizontal axis now corresponds to photon energy.

Notice that the position of the poles in C and X is very similar; however, the strong peak in the photoionization cross section exists only for the C state. Note that while in scattering, cf. Figure 4.1 and 4.2, the resonances in the X and C states were equally visible, in photoionization, only the resonance in the C state is strong. This is clearly due to the integral which is sensitive also to the initial state (orbital); an effect not present in scattering.

We plotted also the dipole matrix element $\left\langle \psi^{(-)}_{l=1,m=0} | \hat{d}_0 | \psi_0 \right\rangle$ for the C state in B_{1u} and found a pole at $E = (23.232 - 2.142)\ eV$ – at the same position as the S-matrix pole in C state. The plots of the magnitude and phase of the dipole element in channel 1 including the pole are shown in Figure 4.6.

In the next step, we will implement the pole removal for the photoionization cross section as well and look at the behaviour of the resonances in more detail.

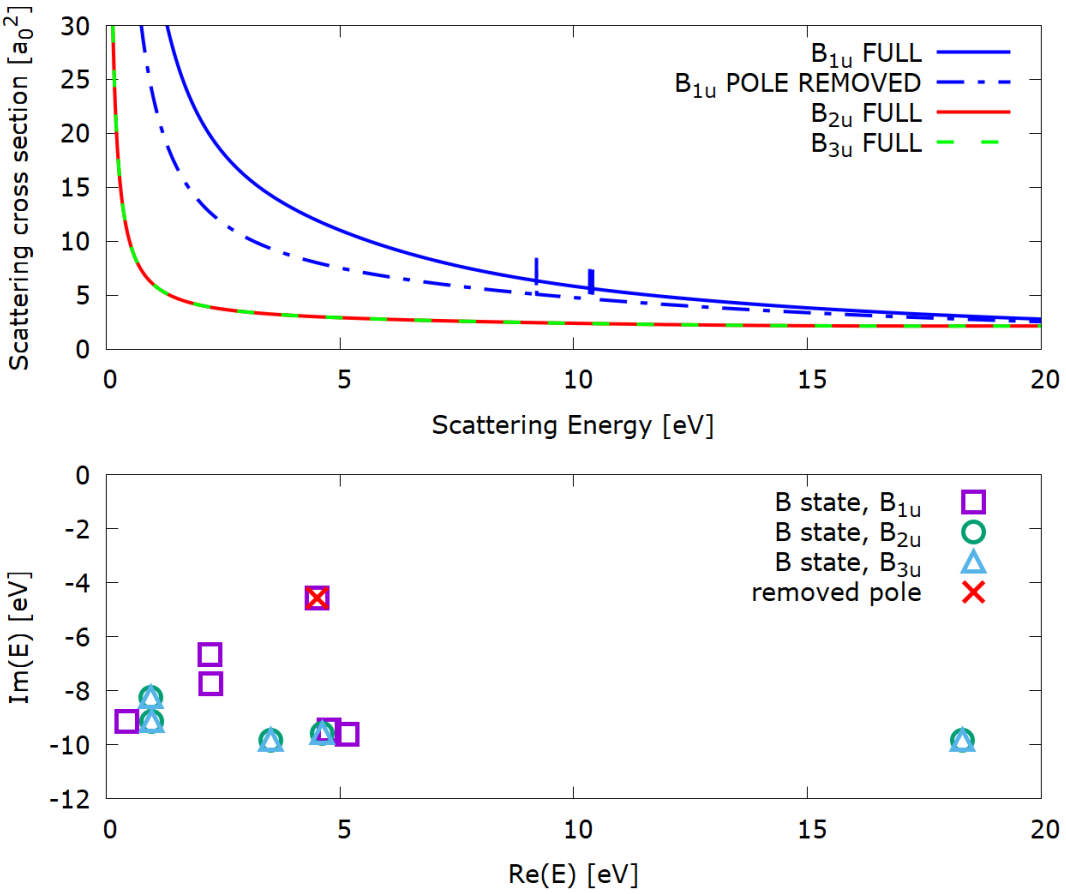

Figure 4.4: The results for the B state of CO_2^+. Upper panel: electron scattering cross section, for B_{1u} with pole removed. Bottom panel: the poles of the S-matrix, the removed pole from the B_{1u} irreducible representation is highlighted.

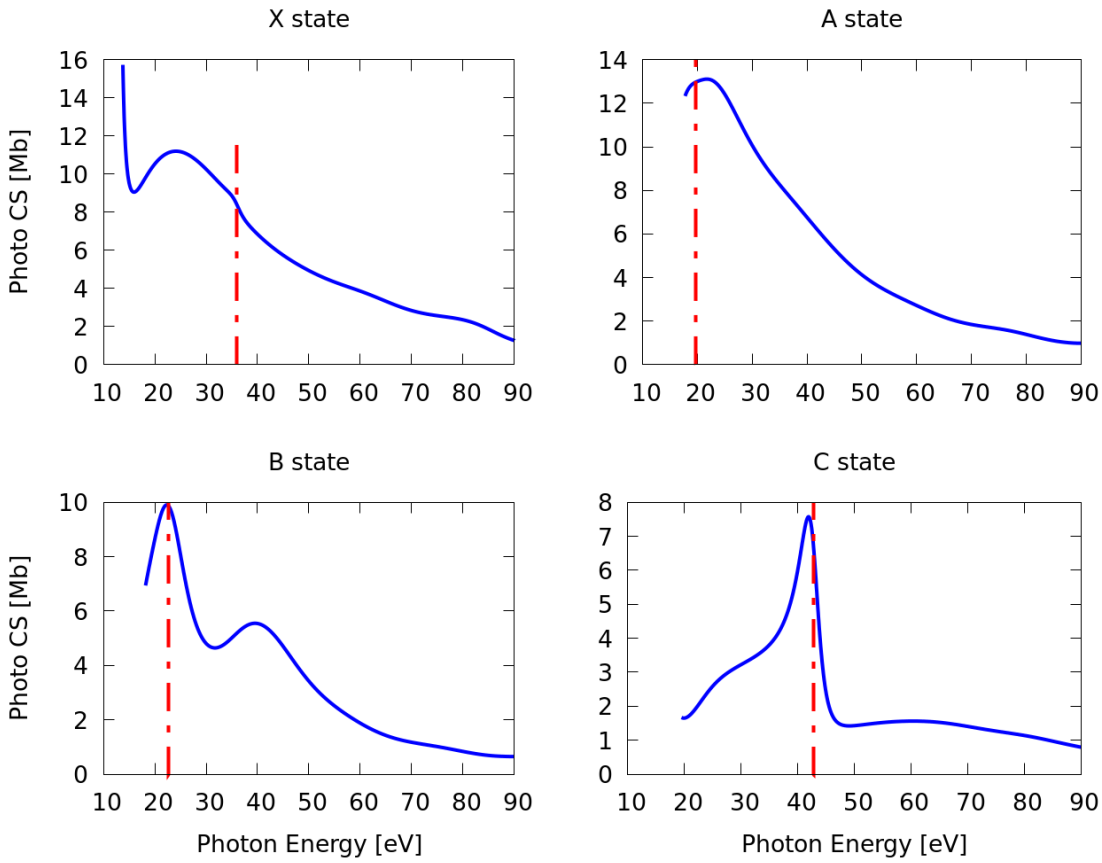

Figure 4.5: Photoionization cross section for CO_2 for four states of $CO_2{}^+$ calculated using the HF model. The positions of the selected poles from Figures 4.1, 4.2, 4.3, and 4.4 are highlighted by the vertical lines.

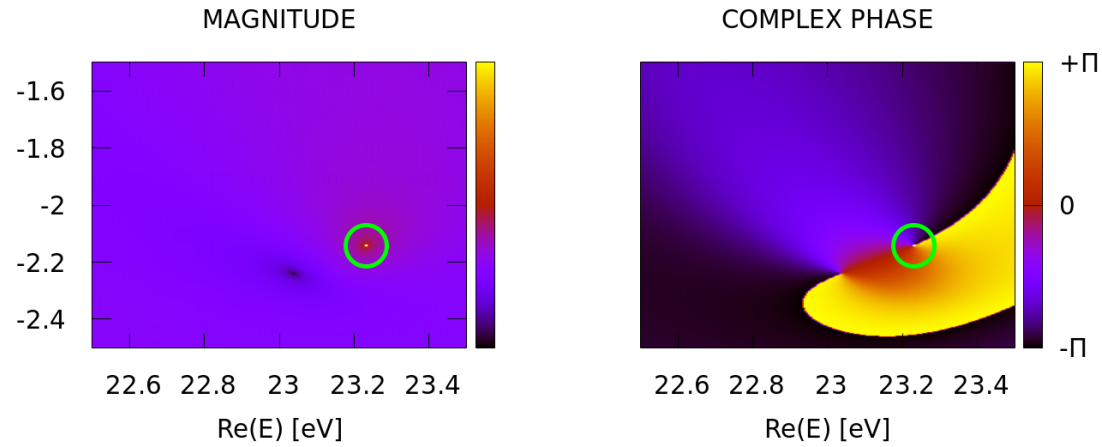

Figure 4.6: The magnitude and the complex phase of the partial-wave dipole matrix element in the complex plane; the pole at $E = (23.232 - 2.142)\ eV$ is marked by the green circles.

4.3 CO_2 in Configuration Interaction model

The more complicated case is the R-matrix solution for the CO_2 ion approximated by the configuration interaction approach (CO_2 CI in what follows) with the following channel properties:

- Number of target channels: $N_{targ} = 300$,
- Total number of channels: $N_{chan} = 2420$.

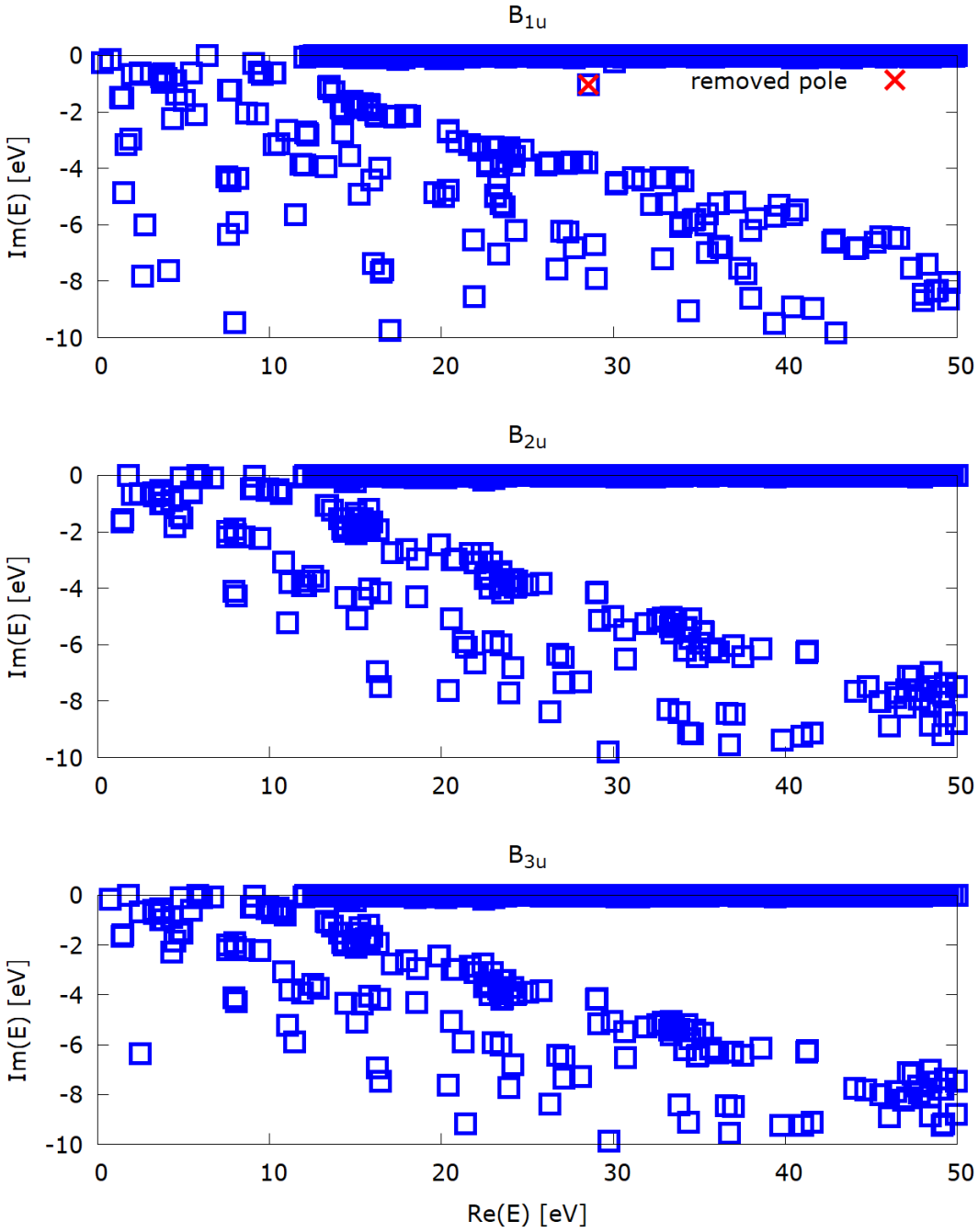

Figure 4.7: Scan of the sheet U_6 of the energy complex plane corresponding to the C state of CO_2 with $N_{targ} = 14$, $N_{chan} = 108$ for the symmetries B_{1u}, B_{2u}, and B_{3u}. In B_{1u}, one resonance is highlighted.

Again, the highest partial wave included was for $l_{max} = 7$. We do not choose the whole set of channels for the scattering solution but, for computational reasons, restrict ourselves to a lower N_{targ}. In the following results, we used

- Number of target channels: $N_{targ} = 14$,
- Total number of channels: $N_{chan} = 108$.

The states from CO_2 HF are equivalent to the first six target channels in CO_2 CI:

- X ($^2\Pi_g$) state (the ground state): target channels 1 and 2 (degenerate),
- A ($^2\Pi_u$) state: channels 3 and 4 (degenerate),
- B ($^2\Sigma_u^+$) state: channel 5,
- C ($^2\Sigma_u^+$) state: channel 6.

The results of the pole search in the complex plane are shown in Figure 4.7 for the sheet U_6 (i.e. the poles here should be affecting the C state). We marked one isolated pole in the symmetry B_{1u} that could be potentially connected with the peak in the photoionization cross section for the C state in Mašín et al. [2018] and with the resonant pole in Figure 4.2. There are a lot of poles in the complex very close to the real axis; they are called auto-ionization resonances and they generate many narrow peaks in cross section. In general, we found many poles in such complex models. A clear advantage of the Siegert analysis is that it allows to reveal much broader structures that are obscured by the dense forest of autoionization resonances.

We evaluated the cross section for electron scattering on the ion, for a particle incoming in channels 1-6 summed over all the outgoing channels; i.e. calculated by

$$\sigma_i = \sum_{j \text{ out}} \sigma_{i \to j}. \tag{4.3}$$

The results are in Figure 4.8; notice that the auto-ionization resonances indeed generated a "noise" of narrow peaks. In Mašín et al. [2018], their effect was partially removed by smoothing using Gaussian functions.

The removal of the pole in Figure 4.8 (in cross section the blue lines behind the red) did not remove any big peak. It means that the resonance is very wide and has a short decay time into each channel.

Although we did not find any isolated resonances that we can connect with significant peaks, we show that our approach is a useful method to isolate chosen poles and analyze their influence on the observable quantities. This case serves as a good illustration of the usability of the method because, without the possibility of removing the pole, it would be naturally considered a good candidate for strong resonance.

We have to mention that our model is not completely consistent with the solution in the internal region because we take only 14 channels from the total number of $N_{targ} = 300$. For restriction to $N_{targ} = 6$, we obtain non-physical results for the particle incoming in channels 5 and 6. We also see that the scattering cross sections for the degenerate target states (channels 1,2 and 3,4) are not equal

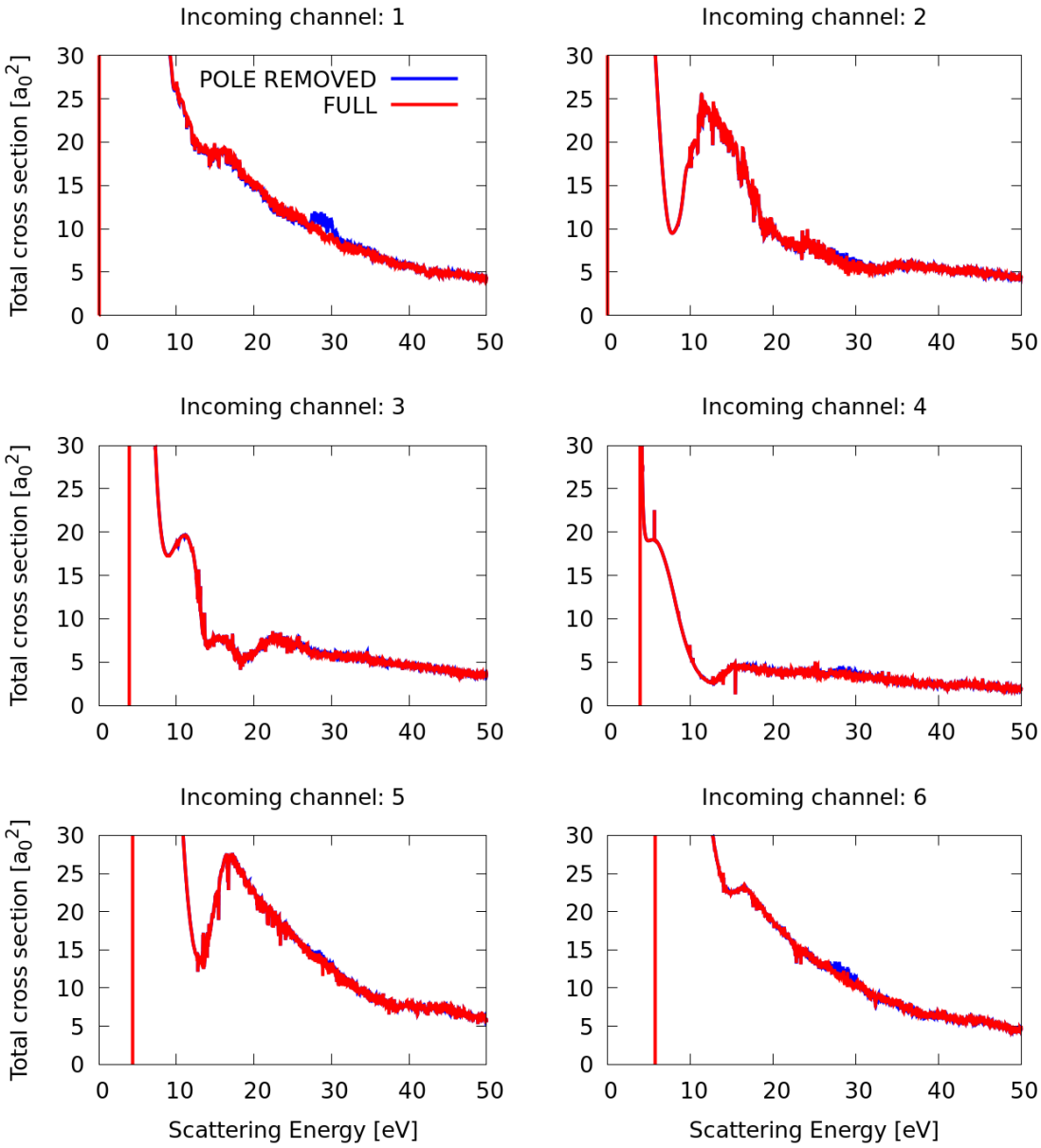

Figure 4.8: CO_2 CI: scattering cross section σ_i for particle incoming in channels 1-6. The lines FULL and POLE REMOVED overlap except for a subset of energies where the removal caused changes in the cross section.

but they should be. However, we have to restrict ourselves to a smaller N_{targ} to obtain the results in a reasonable short time. Therefore, one of the future goals is to obtain results for a model that is consistent in this sense.

4.4 Other molecules

Besides the CO_2^+ ion which served as a testing model for our approach, we worked also with results for $HCOOH^+$ ion and its dimer, N_2O^+, and ammonia and its dimer. These results are quite similar to the results for CO_2 so we include only some of them in Appendix C.

Conclusions

This work followed up my bachelor thesis Konvalinka [2021] where I studied the collision processes in quantum mechanics in one channel for a short-range potential using the Siegert states. In this work, I extended my numerical R-matrix model to the multichannel case and I repeated the implementation of the removal of the Siegert states to study their influence on the cross section in more channels than one.

I performed the first tests of my multichannel approach on the simple model from Grozdanov and McCarroll [2007] and successfully identified and removed the Feshbach resonance. Then, using the model cases and analytical results from Estrada and Domcke [1984] and Herzenberg [1984], I tested my approach on the dipole long-range potential connected with a short-range potential. I managed to confirm the existence of poles of the S-matrix on non-physical sheets of the complex plane of energies and follow their movement in the complex plane. The last test was the application of the Fortran subroutine COULCC and Coulomb-Hankel function to prove that I could solve models with a charged target particle.

After testing my method on the model potentials, I focused on the real applications. I worked with the R-matrix results for ions obtained by the UKRmol+ codes from earlier or yet unpublished results. I implemented the multichannel inelastic scattering approach and the pole removal into the program `siegert` and applied it to look for resonances in the complex energy plane of the $CO_2{}^+$ ion and plotted the electron scattering cross section with the removed resonances. The results for other molecules are to be found in Appendix C.

In the future, we want to implement the same method of the removal of poles for the dipole matrix elements and thus isolate the resonances and remove the peaks from the photoionization cross section. This allows us to study resonance effects also in quantum time delay and other observable quantities of the quantum scattering which are calculated from the S-matrix or the dipole matrix elements. The method of the removal of the poles implemented in UKRmol+ should serve in the code as an approach to analyze the quantum scattering solutions in complex systems. An example of another application can be to rigorously apply the so-called three-step model of High Harmonic Generation which uses dipole matrix elements for complex momenta as explained in detail in Smirnova and Ivanov [2014].

For electron collision applications, a particularly interesting case would be to study the core-excited resonances found by Mašín and Gorfinkiel [2012] but only in time-delays. Their explicit confirmation as poles of S-matrix is still lacking.

Bibliography

Milton Abramowitz and Irene A. Stegun. *Handbook of Mathematical Functions with Formulas, Graphs, and Mathematical Tables*. Dover, New York, ninth dover printing, tenth gpo printing edition, 1964.

H. Bachau, E. Cormier, P. Decleva, J. E. Hansen, and F. Martín. Applications of B-splines in atomic and molecular physics. *Reports on Progress in Physics*, 64(12):1815–1943, nov 2001. doi: 10.1088/0034-4885/64/12/205. URL https://doi.org/10.1088/0034-4885/64/12/205.

John Burkardt. URL: https://people.sc.fsu.edu/ jburkardt, Jul 2020. URL https://people.sc.fsu.edu/~jburkardt. Accessed: 2021-01-20.

P G Burke and M J Seaton. The vicinity of an R-matrix pole. *Journal of Physics B: Atomic and Molecular Physics*, 17(20):L683, oct 1984. doi: 10.1088/0022-3700/17/20/006. URL https://dx.doi.org/10.1088/0022-3700/17/20/006.

Philip George Burke. *R-Matrix Theory of Atomic Collisions*. Springer, Berlin, Heidelberg, 2011. ISBN 978-3-642-15930-5.

Yi-Jen Chen, Stefan Pabst, Antonia Karamatskou, and Robin Santra. Theoretical characterization of the collective resonance states underlying the xenon giant dipole resonance. *Journal of Physics: Conference Series*, 635(9):092046, aug 2015. doi: 10.1088/1742-6596/635/9/092046. URL https://dx.doi.org/10.1088/1742-6596/635/9/092046.

T. S. Chihara. *An Introduction to Orthogonal Polynomials*. Gordon and Breach Science Publishers, New York, 1978. ISBN 0-677-04150-0.

Kevin Connolly and David J. Griffiths. Critical dipoles in one, two, and three dimensions. *American Journal of Physics*, 75(6):524–531, 06 2007. ISSN 0002-9505. doi: 10.1119/1.2710485. URL https://doi.org/10.1119/1.2710485.

R. de la Madrid and M. Gadella. A pedestrian introduction to Gamow vectors. *American Journal of Physics*, 70(6):626–638, 06 2002. ISSN 0002-9505. doi: 10.1119/1.1466817. URL https://doi.org/10.1119/1.1466817.

Rafael de la Madrid, Gaston Garcia-Calderon, and Juan Gonzalo Muga. Resonance expansions in quantum mechanics. *Czechoslovak Journal of Physics*, 55(9):1141–1150, September 2005. ISSN 1572-9486. doi: 10.1007/s10582-005-0119-6. URL http://dx.doi.org/10.1007/s10582-005-0119-6.

P. Descouvemont and D. Baye. The R-matrix theory. *Reports on Progress in Physics*, 73(036301), feb 2010. doi: 10.1088/0034-4885/73/3/036301.

H. Estrada and W. Domcke. Analytic properties of the S-matrix for a simple model of fixed-nuclei electron-polar-molecule scattering. *J. Phys. B: Atom. Mol. Phys. (1968-1987)*, 17:279, 1984.

R Fandreyer, P G Burke, L A Morgan, and C J Gillan. Low-energy electron scattering by HBr. *Journal of Physics B: Atomic, Molecular and Optical Physics*, 26(20):3625, oct 1993. doi: 10.1088/0953-4075/26/20/021. URL https://dx.doi.org/10.1088/0953-4075/26/20/021.

Harald Friedrich. *Theoretical Atomic Physics*. Springer-Verlag, Berlin, Heidelberg, 1990. ISBN 3-540-52982-9.

Harald Friedrich. *Scattering theory*. Springer-Verlag Berlin Heidelberg, 2016. ISBN 978-3-662-48526-2.

TP Grozdanov and R McCarroll. Multichannel scattering calculations using absorbing potentials and mapped grids. *The Journal of chemical physics*, 126(3): 034310, 2007.

Alex G Harvey, Danilo S Brambila, Felipe Morales, and Olga Smirnova. An R-matrix approach to electron–photon–molecule collisions: photoelectron angular distributions from aligned molecules. *Journal of Physics B: Atomic, Molecular and Optical Physics*, 47(21):215005, oct 2014. doi: 10.1088/0953-4075/47/21/215005. URL https://dx.doi.org/10.1088/0953-4075/47/21/215005.

A Herzenberg. Singularities in the scattering of a very slow electron by a weakly polar molecule. *Journal of Physics B: Atomic and Molecular Physics*, 17(20): 4213, oct 1984. doi: 10.1088/0022-3700/17/20/019. URL https://dx.doi.org/10.1088/0022-3700/17/20/019.

A Herzenberg and B C Saha. The virtual electron state in a weakly polar molecule. *Journal of Physics B: Atomic and Molecular Physics*, 16(4):591, feb 1983. doi: 10.1088/0022-3700/16/4/013. URL https://dx.doi.org/10.1088/0022-3700/16/4/013.

Matěj Konvalinka. Analýza srážkových procesů v kvantové mechanice s použitím Siegertových stavů, July 2021. URL https://dspace.cuni.cz/handle/20.500.11956/128270. Accepted: 2021-08-03T09:26:34Z Publisher: Univerzita Karlova, Matematicko-fyzikální fakulta.

Steven E. Koonin. *Computational Physics*. The Benjamin/Cummings Publishing Company, Inc., Menlo Park, California, 1986. ISBN 0-8053-5430-1.

Jiří Kopáček. *Matematická analýza nejen pro fyziky (IV)*. Matfyzpress, 2010. ISBN 978-80-7378-120-0.

Stephane Mazevet, Michael A Morrison, Lesley A. Morgan, and Robert K. Nesbet. Virtual-state effects on elastic scattering and vibrational excitation of CO_2 by electron impact. *Phys. Rev. A*, 64:040701, Sep 2001. doi: 10.1103/PhysRevA.64.040701. URL https://link.aps.org/doi/10.1103/PhysRevA.64.040701.

Zdeněk Mašín and Jimena D. Gorfinkiel. Shape and core excited resonances in electron collisions with diazines. *The Journal of Chemical Physics*, 137 (20):204312–204312–14, November 2012. ISSN 00219606. doi: doi:10.1063/1.4767345. URL http://jcp.aip.org.libezproxy.open.ac.uk/resource/1/jcpsa6/v137/i20/p204312_s1.

Zdeněk Mašín, Alex G Harvey, Michael Spanner, Serguei Patchkovskii, Misha Ivanov, and Olga Smirnova. Electron correlations and pre-collision in the re-collision picture of high harmonic generation. *Journal of Physics B: Atomic, Molecular and Optical Physics*, 51(13):134006, jun 2018. doi: 10.1088/1361-6455/aac598. URL https://dx.doi.org/10.1088/1361-6455/aac598.

Zdeněk Mašín, Jakub Benda, Jimena D. Gorfinkiel, Alex G. Harvey, and Jonathan Tennyson. UKRmol+: A suite for modelling electronic processes in molecules interacting with electrons, positrons and photons using the R-matrix method. *Computer Physics Communications*, 249:107092, April 2020. ISSN 0010-4655. doi: 10.1016/j.cpc.2019.107092. URL http://dx.doi.org/10.1016/j.cpc.2019.107092.

M McCartney, P G Burke, L A Morgan, and C J Gillan. Resonance effects in low energy electron scattering by HCl. *Journal of Physics B: Atomic, Molecular and Optical Physics*, 23(15):L415, aug 1990. doi: 10.1088/0953-4075/23/15/006. URL https://dx.doi.org/10.1088/0953-4075/23/15/006.

L. A. Morgan. Virtual states and resonances in electron scattering by CO_2. *Phys. Rev. Lett.*, 80:1873–1875, Mar 1998. doi: 10.1103/PhysRevLett.80.1873. URL https://link.aps.org/doi/10.1103/PhysRevLett.80.1873.

L A Morgan and P G Burke. Low-energy electron scattering by HF. *Journal of Physics B: Atomic, Molecular and Optical Physics*, 21(11):2091, jun 1988. doi: 10.1088/0953-4075/21/11/022. URL https://dx.doi.org/10.1088/0953-4075/21/11/022.

L A Morgan, P G Burke, and C J Gillan. Low-energy electron scattering by HCl. *Journal of Physics B: Atomic, Molecular and Optical Physics*, 23(1):99, jan 1990. doi: 10.1088/0953-4075/23/1/011. URL https://dx.doi.org/10.1088/0953-4075/23/1/011.

H. M. Nussenzveig. The poles of the S-matrix of a rectangular potential well of barrier. *Nuclear Physics*, 11:499 – 521, 1959. ISSN 0029-5582. doi: https://doi.org/10.1016/0029-5582(59)90293-7. URL http://www.sciencedirect.com/science/article/pii/0029558259902937.

TP Ragesh Kumar, P Nag, M Rankovic, TFM Luxford, J Kocisek, Z Masin, and J Fedor. Distant symmetry control in electron-induced bond cleavage. *The Journal of Physical Chemistry Letters*, 13(48):11136–11142, 2022a.

TP Ragesh Kumar, P Nag, M Rankovic, TFM Luxford, J Kocisek, Z Masin, and J Fedor. Supplementary information for 'distant symmetry control in electron-induced bond cleavage'. Heyrovský Institute of Physical Chemistry, The Czech Academy of Sciences, Dolejskova 3, 18223 Prague, Czech Republic; Faculty of Mathematics and Physics, Charles University, Institute of Theoretical Physics, V Holesovickach 2, 18000 Prague, Czech Republic, 2022b.

S. A. Rakityansky and N. Elander. Analyzing the contribution of individual resonance poles of the S-matrix to two-channel scattering. *Journal of Quantum Chemistry*, 106:25, 2005.

Barry I. Schneider. Direct calculation of resonance energies and widths using an R-matrix approach. *Phys. Rev. A*, 24:1–3, Jul 1981. doi: 10.1103/PhysRevA.24.1. URL https://link.aps.org/doi/10.1103/PhysRevA.24.1.

Isao Shimamura. Complete separation of resonance and nonresonance channel spaces. *Journal of Physics B: Atomic, Molecular and Optical Physics*, 44(20): 201002, sep 2011. doi: 10.1088/0953-4075/44/20/201002. URL https://dx.doi.org/10.1088/0953-4075/44/20/201002.

A. J. F. Siegert. On the derivation of the dispersion formula for nuclear reactions. *Phys. Rev.*, 56:750–752, Oct 1939. doi: 10.1103/PhysRev.56.750. URL https://link.aps.org/doi/10.1103/PhysRev.56.750.

George V. Sitnikov and Oleg I. Tolstikhin. Siegert pseudostate formulation of scattering theory: Two-channel case. *Phys. Rev. A*, 67:032714, Mar 2003. doi: 10.1103/PhysRevA.67.032714. URL https://link.aps.org/doi/10.1103/PhysRevA.67.032714.

Olga Smirnova and Misha Ivanov. *Multielectron High Harmonic Generation: Simple Man on a Complex Plane*, chapter 7, pages 201–256. John Wiley Sons, Ltd, 2014. ISBN 9783527677689. doi: https://doi.org/10.1002/9783527677689.ch7. URL https://onlinelibrary.wiley.com/doi/abs/10.1002/9783527677689.ch7.

John R. Taylor. *Scattering theory: The quantum theory of nonrelativistic collisions*. John Wiley Sons, Inc., New York, 1972. ISBN 0-471-84900-6.

I.J. Thompson and A.R. Barnett. COULCC: A continued-fraction algorithm for coulomb functions of complex order with complex arguments. *Computer Physics Communications*, 36(4):363–372, 1985. ISSN 0010-4655. doi: https://doi.org/10.1016/0010-4655(85)90025-6. URL https://www.sciencedirect.com/science/article/pii/0010465585900256.

Oleg I. Tolstikhin, Valentin N. Ostrovsky, and Hiroki Nakamura. Siegert pseudostate formulation of scattering theory: One-channel case. *Phys. Rev. A*, 58:2077–2096, Sep 1998. doi: 10.1103/PhysRevA.58.2077. URL https://link.aps.org/doi/10.1103/PhysRevA.58.2077.

E. P. Wigner and L. Eisenbud. Higher angular momenta and long range interaction in resonance reactions. *Phys. Rev.*, 72:29–41, Jul 1947. doi: 10.1103/PhysRev.72.29. URL https://link.aps.org/doi/10.1103/PhysRev.72.29.

List of Figures

List of Tables

A. Potential well: Feshbach resonance in two channels

The cross section for the problem described in 3.1 for all four possible transitions is in Figure A.1 and A.2, respectively. The full cross section is in the top panels and the transformed cross section with the pole removed is in the bottom panels.

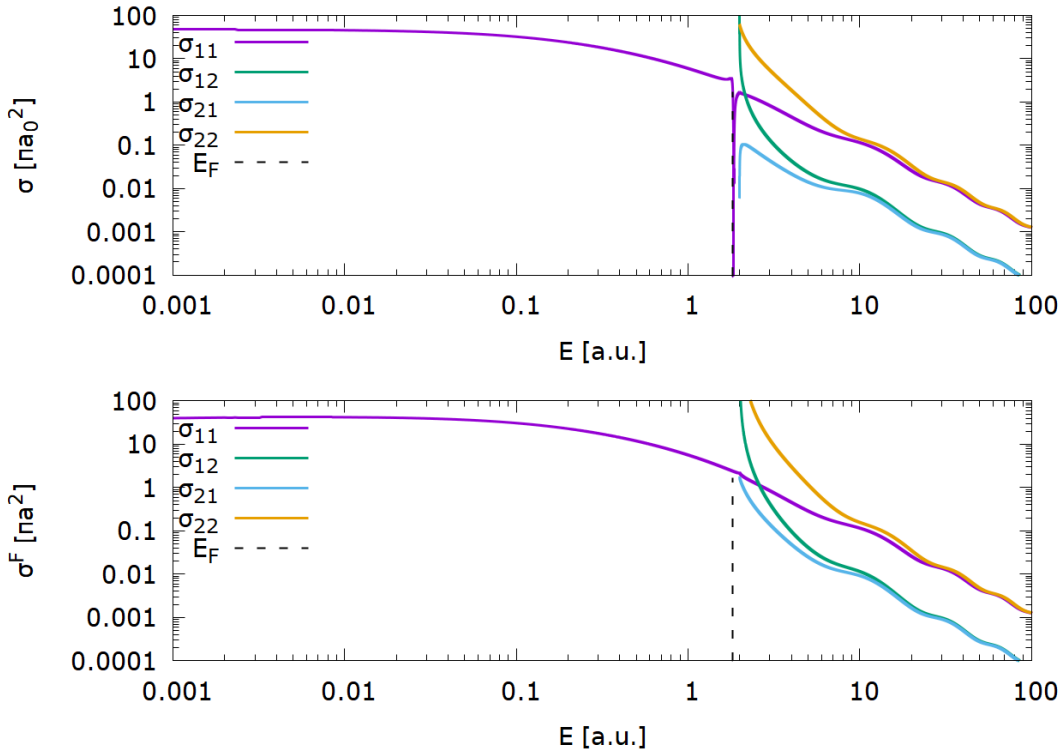

Figure A.1: The cross section of the potential well defined by (3.2) and the angular momentum $l_1 = l_2 = 0$ as a function of the energy E on the logarithmic scale. On the bottom diagram is the cross section after the removal of the Feshbach resonance.

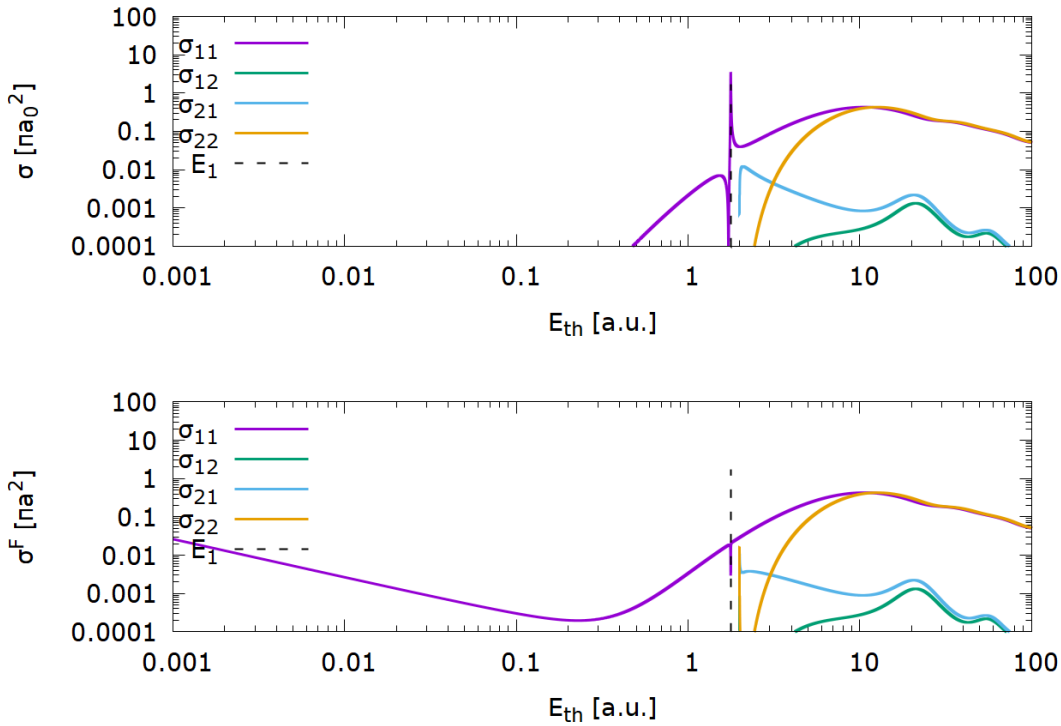

Figure A.2: The cross section of the potential well defined by (3.2) and the angular momentum $l_1 = l_2 = 3$ as a function of the energy E on the logarithmic scale. On the bottom figure is the cross section after the removal of the Feshbach resonance.

B. Riccati-Hankel functions for complex argument and order

In this section, we describe the theory behind the implementation of the Fortran subroutine `riccati_hankel_plus_riemann` that evaluates the Riccati-Hankel functions using an expansion and allowing control over the complex argument of the input. We draw the information from Abramowitz and Stegun [1964].

In our convention, the Riccati-Hankel functions of order λ are related to the spherical Hankel functions by

$$\hat{h}_\lambda^{(\pm)}(z) = \pm \mathrm{i} z h_\lambda^{(\pm)}(z). \tag{B.1}$$

The following formula expresses the spherical Hankel functions

$$h_\lambda^{(\pm)}(z) = \sqrt{\frac{\pi}{2z}} H_{\lambda+\frac{1}{2}}^{(\pm)}(z) = \sqrt{\frac{\pi}{2z}} \left(J_{\lambda+\frac{1}{2}}(z) \pm \mathrm{i} Y_{\lambda+\frac{1}{2}}(z) \right), \tag{B.2}$$

where $H_{\lambda+\frac{1}{2}}^{(\pm)}$ are the Hankel functions of the first and second kind and $J_{\lambda+\frac{1}{2}}$, $Y_{\lambda+\frac{1}{2}}$ are the Bessel functions of the first and second kind. The functions Y_ν of order ν are expressed by

$$Y_\nu(z) = \frac{J_\nu \cos(\nu\pi) - J_{-\nu}(z)}{\sin(\nu\pi)}. \tag{B.3}$$

Combining the equations (B.2) and (B.3), we see that it is sufficient to calculate the functions $J_{\pm(\lambda+\frac{1}{2})}$ to obtain both kinds of the Riccati-Hankel functions. The full expression is

$$\hat{h}_\lambda^{(\pm)}(z) = \sqrt{\frac{\pi z}{2}} \frac{J_{-(\lambda+\frac{1}{2})}(z) - e^{\mp \mathrm{i}(\lambda+\frac{1}{2})\pi} J_{(\lambda+\frac{1}{2})}(z)}{\sin[(\lambda+\frac{1}{2})\pi]}. \tag{B.4}$$

The functions $J_\nu(z)$ are evaluated from the absolutely convergent series

$$J_\nu(z) = \left(\frac{1}{2}\right)^\nu |z|^\nu \exp(\mathrm{i}\nu\theta) \sum_{k=0}^{\infty} \frac{\left(-\frac{1}{4}\right)^k \left(|z|^{2k} e^{\mathrm{i}2k\theta}\right)}{k!\Gamma(\nu+k+1)}, \tag{B.5}$$

where we separate the amplitude and argument of $z = |z| \exp(\mathrm{i}\theta)$. Calculating the functions in this form enables control over the complex argument of z. Moreover, the sum in (B.7) is invariant to the choice of the argument θ. The whole dependence on θ lies in the term $\exp(\mathrm{i}\nu\theta)$ from (B.7) and in $\sqrt{\pi z/2}$, cf. (B.4).

For the derivatives of the Riccati-Hankel functions $\mathrm{d}\hat{h}_\lambda^{(\pm)}(z)/\mathrm{d}z$, we use a similar formula, easily derived from the equation (B.4)

$$\frac{\mathrm{d}\hat{h}_\lambda^{(\pm)}(z)}{\mathrm{d}z} = \sqrt{\frac{\pi z}{2}} \frac{\frac{\mathrm{d}J_{-\lambda-\frac{1}{2}}(z)}{\mathrm{d}z} - e^{\mp \mathrm{i}(\lambda+\frac{1}{2})\pi} \frac{J_{(\lambda+\frac{1}{2})}(z)}{\mathrm{d}z}}{\sin[(\lambda+\frac{1}{2})\pi]} + \frac{1}{2z} \hat{h}_\lambda^{(\pm)}(z). \tag{B.6}$$

Analogically to (B.7), we have an expansion for the derivatives of the Bessel functions

$$\frac{\mathrm{d}J_\nu(z)}{\mathrm{d}z} = \left(\frac{1}{2}\right)^\nu |z|^{\nu-1} e^{\mathrm{i}(\nu-1)\theta} \sum_{k=0}^{\infty} \frac{\left(-\frac{1}{4}\right)^k (2k+\nu) \left(|z|^{2k} e^{\mathrm{i}2k\theta}\right)}{k!\Gamma(\nu+k+1)}. \tag{B.7}$$

Thus, calculating the Bessel functions and their derivatives order $\lambda + 1/2$ and $-\lambda - 1/2$, we obtain the Riccati-Hankel functions and their derivatives on an arbitrary Riemann surface, easily controlled by the multi-valued term $\exp(\mathrm{i}\nu\theta)$.

C. Siegert states in molecule: other results

C.1 $HCOOH^+$

The scans of the complex plane for $HCOOH^+$ for states $1a''$, $2a''$, $7a'$, $8a'$, $9a'$, and $10a'$ are below in Figures C.1 and C.2 for A' and A'' irreducible representations of the C_s point group of the molecule. We can find some isolated resonances in the plots. We applied the removal of these isolated resonances but it did not lead to any significant changes in the electron scattering cross section so we do not attach the plots of the cross section.

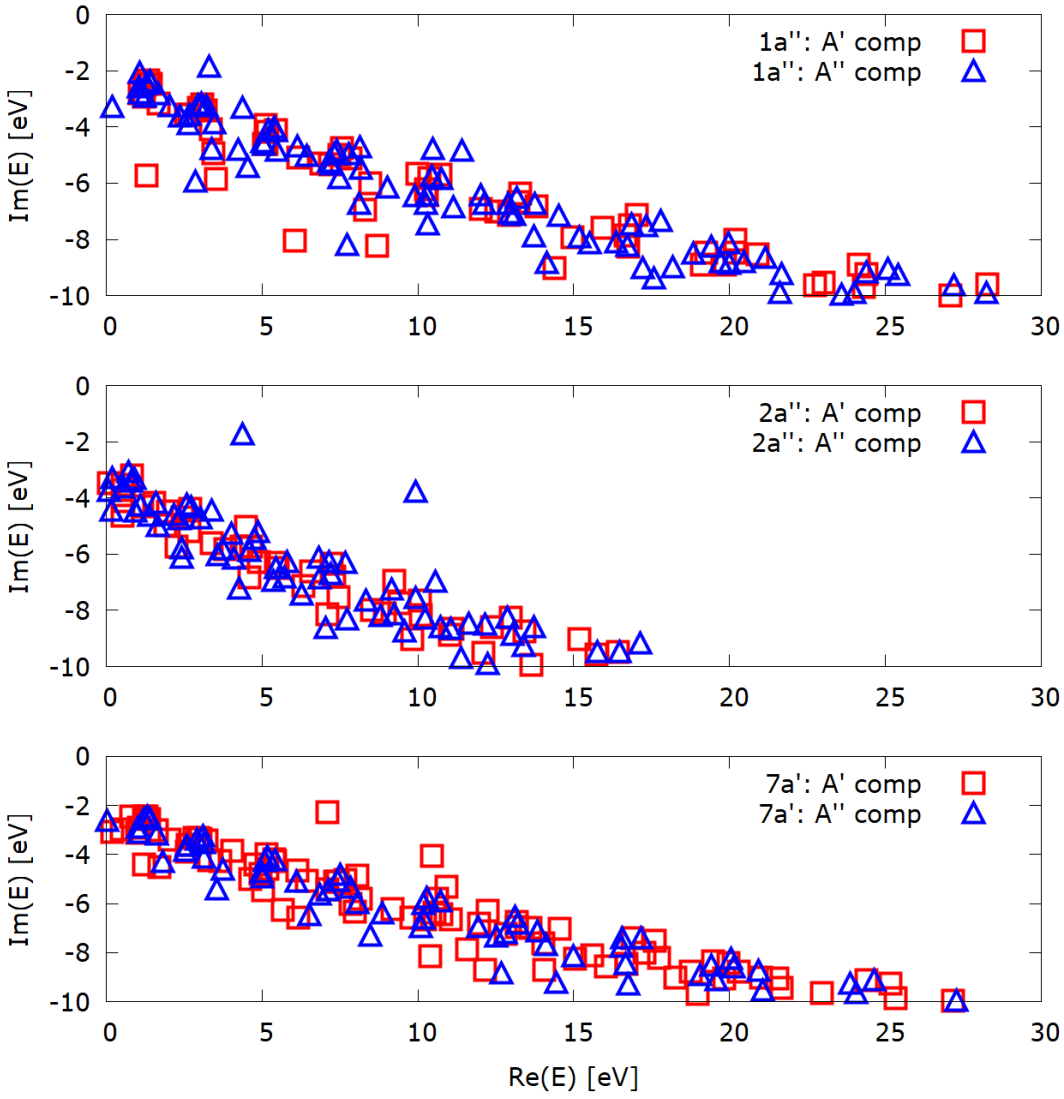

Figure C.1: Scan of the complex plane for the $HCOOH^+$ for the states $1a''$, $2a''$, $7a'$

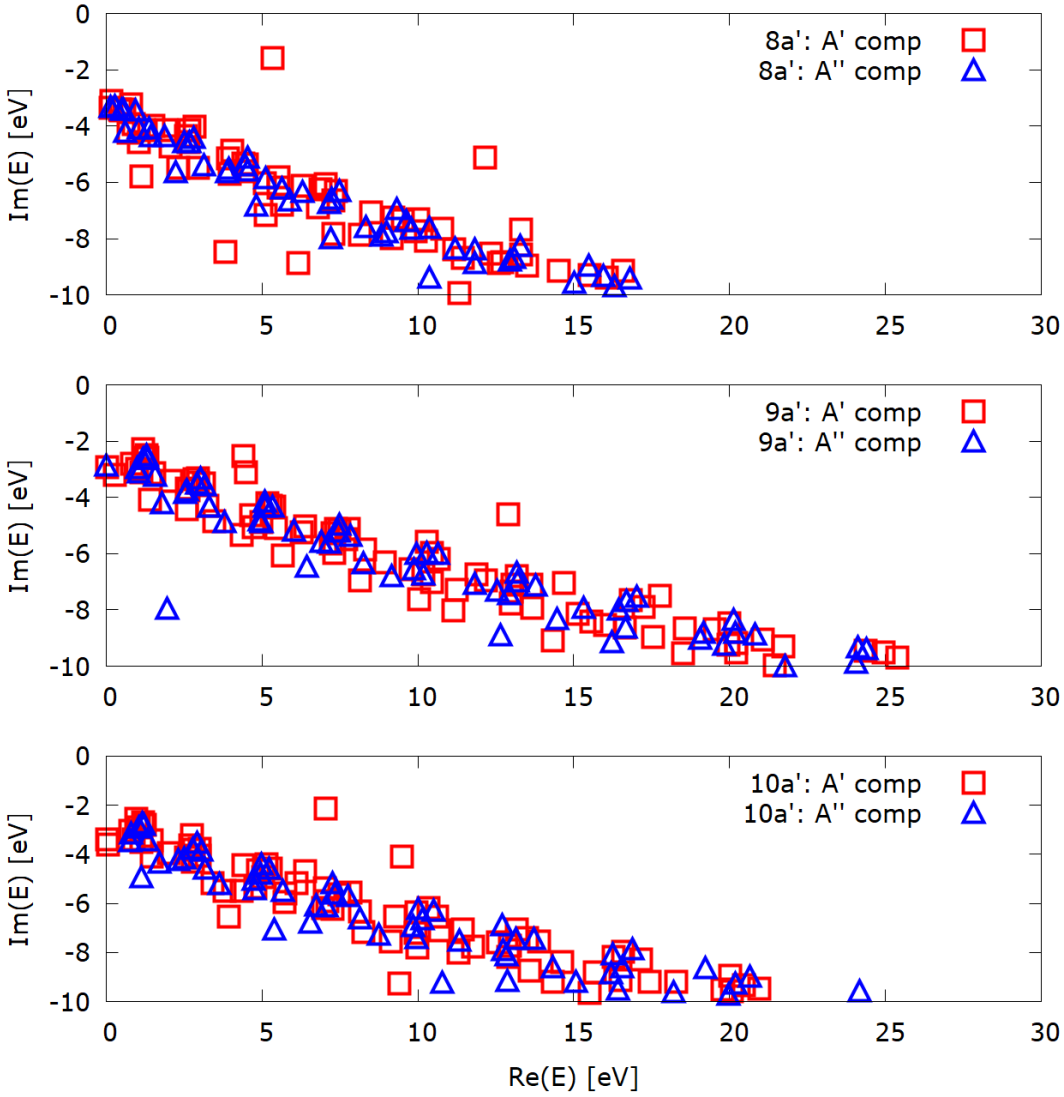

Figure C.2: Scan of the complex plane for the $HCOOH^+$ for the states $8a'$, $9a'$, $10a'$

C.2 Ion of HCOOH dimer

We scan the complex plane for the states $1a_u$, $1b_g$, $2a_u$, $2b_g$, $9a_g$, $9b_u$, $10a_g$, and $10b_u$, each either in A_u or in B_u irreducible representation of the C_{2h} molecular point group. The results are in Figures C.3 and C.4. For some resonances, we obtained interesting results using the removal of poles – the results of the removal are in Figure C.5 and removed poles are marked by crosses in Figure C.3. This is the case where the removal shows us resonant peaks that are hardly visible in the cross section.

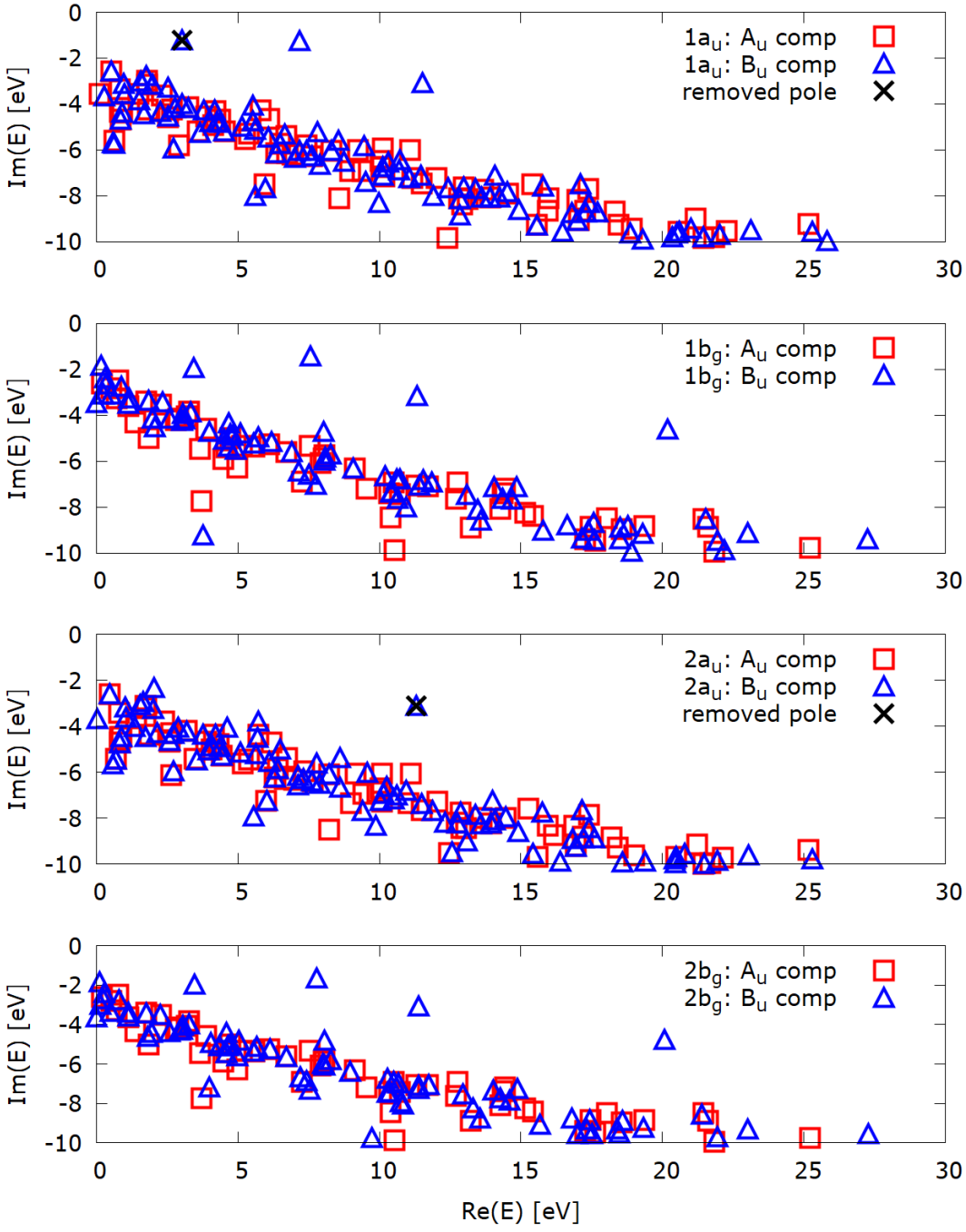

Figure C.3: Scan of the complex plane for the ion of HCOOH dimer for the states $1a_u$, $1b_g$, $2a_u$, $2b_g$.

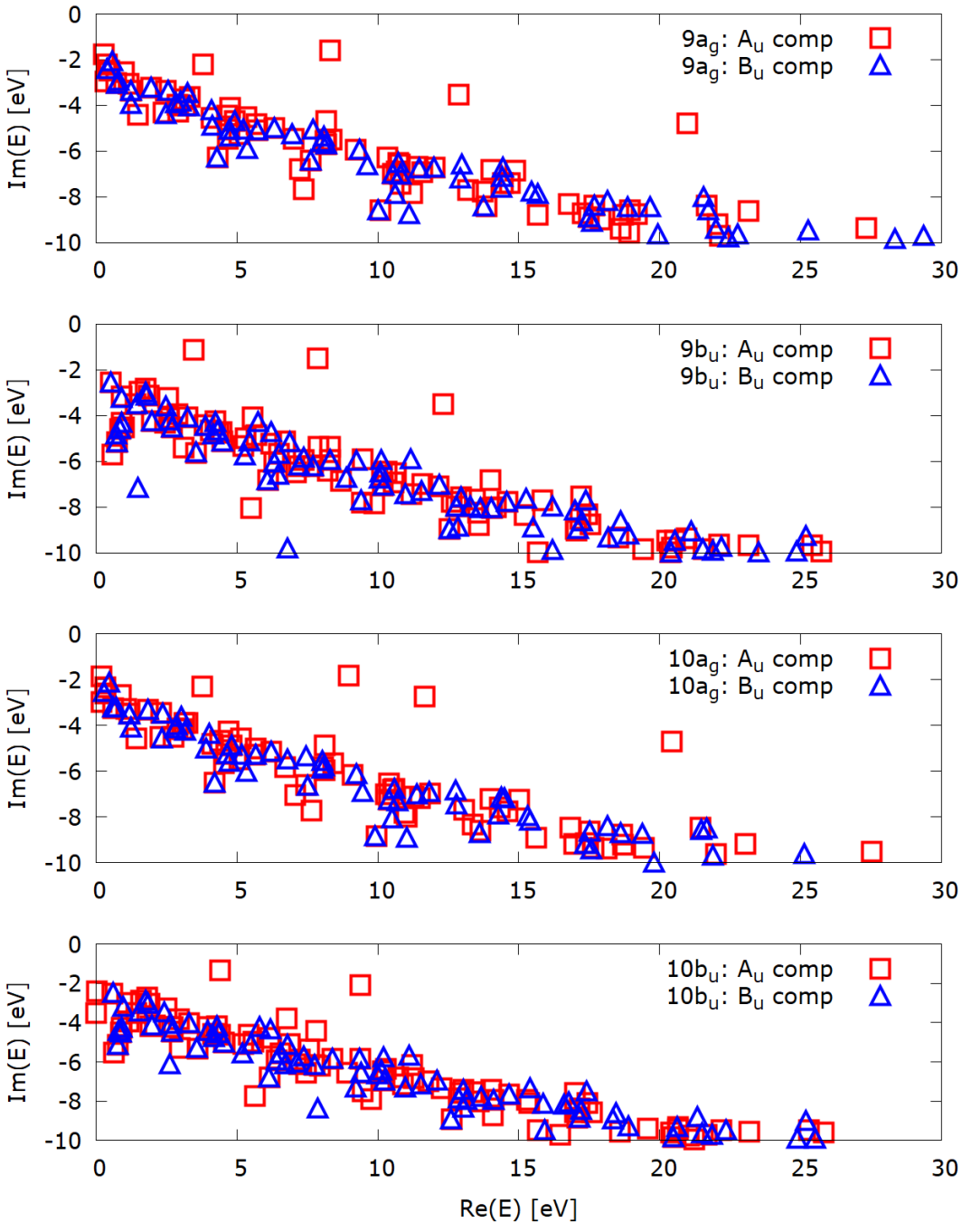

Figure C.4: Scan of the complex plane for the ion of HCOOH dimer for the states $9a_g$, $9b_u$, $10a_g$, $10b_u$.

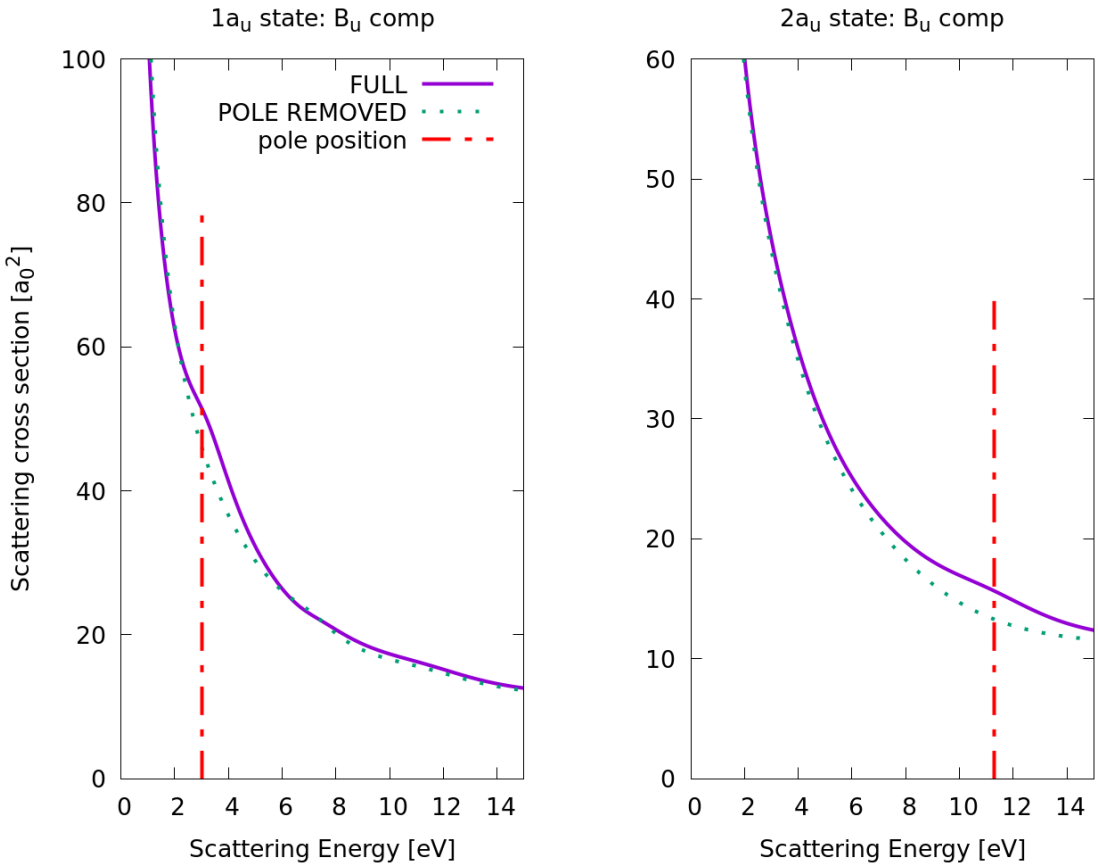

Figure C.5: The cross section for the electron scattering on the ion of HCOOH dimer for states $1a_u$ and $2a_u$ with the cross section after removing of resonances marked in Figure C.1.

C.3 N_2O^+

The same results as for HCOOH and its dimer are in this section for N_2O – scans of the complex plane in Figure C.6 and the chosen removals of the poles in the cross section in Figure C.7. The point group in this case is C_{2v}.

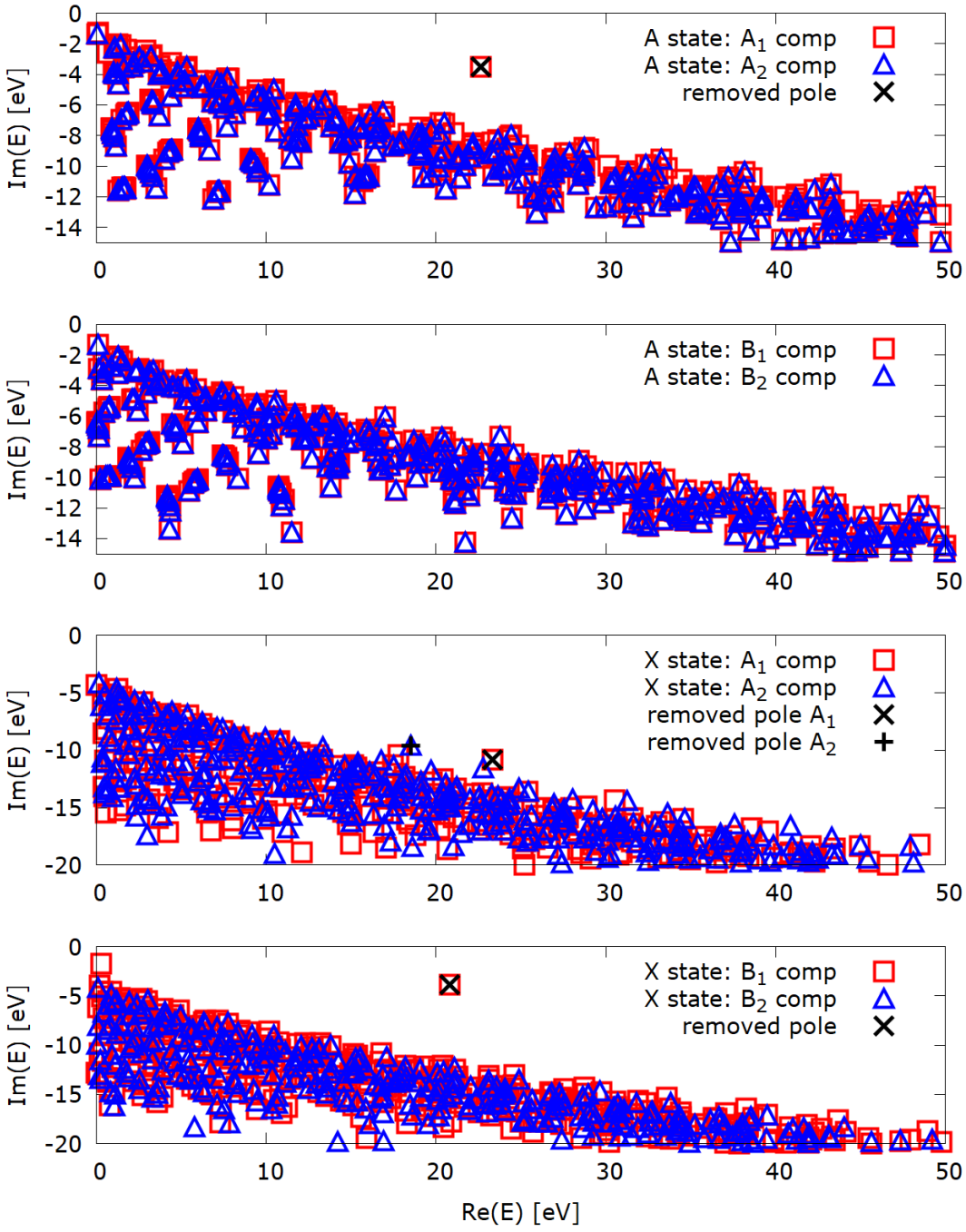

Figure C.6: Scan of the complex plane for the N_2O^+ ion for the states A and X.

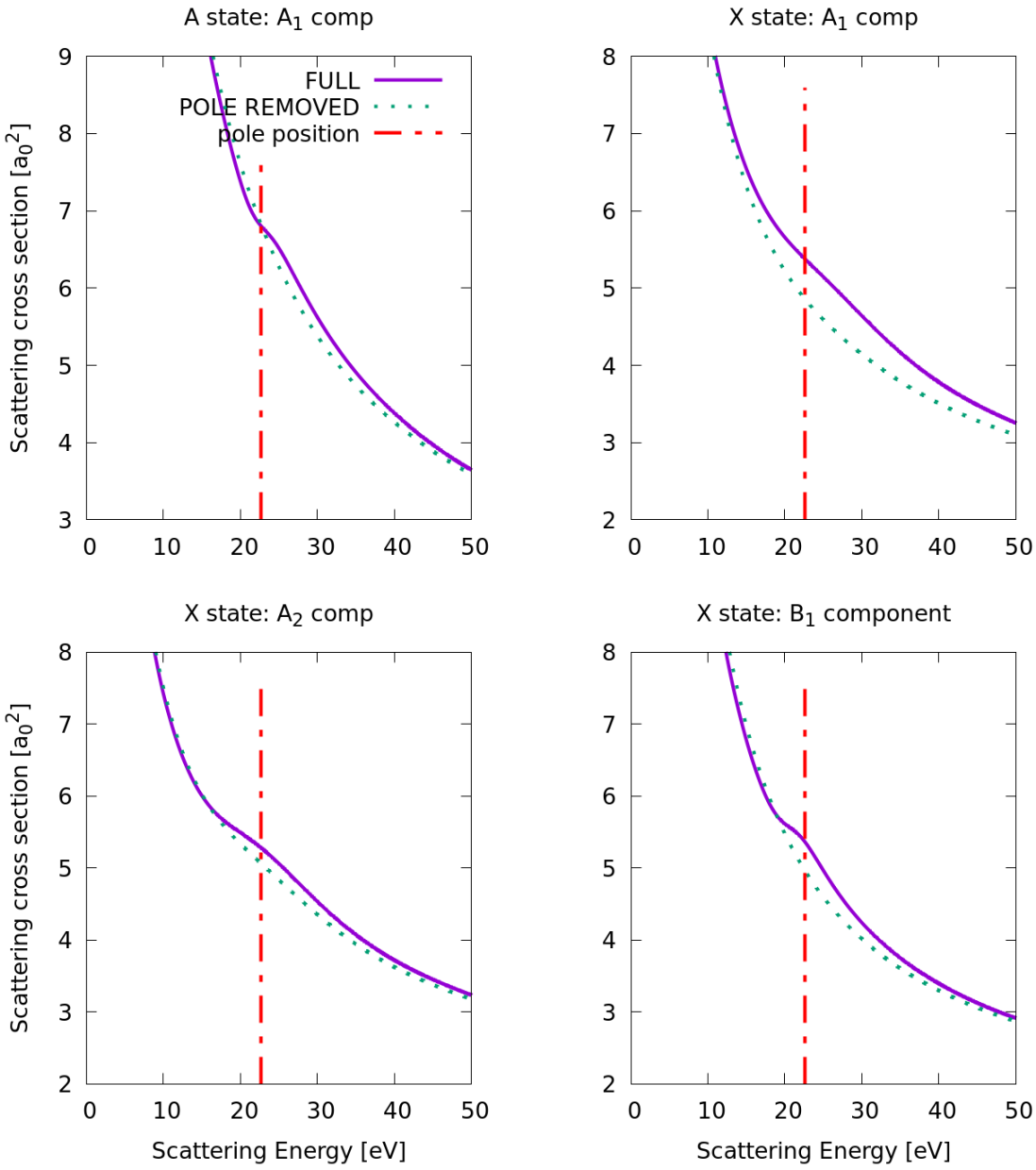

Figure C.7: The cross section for the electron scattering on the N_2O^+ ion for component A_1 in state A and components A_1, A_2, B_1 in state X; the cross section after removing of resonances that are marked in Figure C.6.